Frequency Comb Generation From Stimulated Brillouin Scattering and Semiconductor Laser Diodes

by

Mark Dong

A dissertation submitted in partial fulfillment
of the requirements for the degree of
Doctor of Philosophy
(Electrical Engineering)
in The University of Michigan
2018

Doctoral Committee:

Professor Herbert Winful, Co-Chair
Professor Steven Cundiff, Co-Chair
Professor Mackillo Kira
Professor Zetian Mi
Professor Georg Raithel

Mark Dong

markdong@umich.edu

ORCID iD: 0000-0002-8577-451X

To my fiancée, who, in the time it took for me to complete this dissertation, has done more to help the underprivileged and improve the lives of others than this dissertation probably ever will.

ACKNOWLEDGEMENTS

I would like to thank all my dissertation committee members for serving, especially my advisors Herbert Winful and Steven Cundiff for all their guidance and advice over the years. I also like to thank all the hard working technical and support staff in the ECE and Physics departments for the innumerable times they have helped me.

In addition, this work was supported in part by the Defense Advanced Research Projects Agency through the SCOUT program and in part through computational resources and services provided by Advanced Research Computing at the University of Michigan, Ann Arbor.

PREFACE

This dissertation is the culmination of a somewhat unconventional journey through my graduate studies. As the reader may notice, the contents of this thesis contain some chapters not wholly relevant to frequency comb generation, namely the two chapters on stimulated Brillouin scattering. However, these chapters represent some significant work I had done prior to working on semiconductor lasers. Serendipitous or not, the theoretical understanding and technical expertise gained from modeling Brillouin scattering was greatly relevant to the traveling wave models I would use and develop in studying our laser diodes. For this reason, these chapters serve as a prelude to the main event that is frequency comb generation directly from a semiconductor laser diode. There are even more research projects I had worked on that predate Brillouin scattering during my Ph.D., but alas, due to their divergence in content, I am not able to include them.

This dissertation consists of about two-thirds theoretical studies and one-third experimental results. It is presented in mostly chronological order, which also happens to be good for following along.

Mark Dong,
April 2018

TABLE OF CONTENTS

CHAPTER

LIST OF TABLES

Table

LIST OF FIGURES

Figure

LIST OF ABBREVIATIONS

BCB Benzocyclobutene

BHF Buffered Hydrofluoric acid

BVP boundary value problem

CW continuous wave

DBR distributed Bragg reflector

FSR free spectral range

FWM four-wave mixing

GDD group delay dispersion

GVD group velocity dispersion

HF hydrofluoric acid

IVP initial value problem

LED light-emitting diode

LHS left hand side

LNF Lurie Nanofabrication Facility

MBE molecular beam epitaxy

MOCVD metal-organic chemical vapor deposition

MQW multi-quantum well

PECVD plasma enhanced chemical vapor deposition

PID proportional integral derivative

PL photoluminescence

PVD physical vapor deposition

QC quantum cascade

QD quantum dot

QW quantum well

RF radio frequency

RHS right hand side

SBS stimulated Brillouin scattering

SCH separate confinement heterostructure

SEM scanning electron microscope

SESAM Semiconductor saturable absorber mirror

SNR signal to noise ratio

SOP standard operating procedure

SRS stimulated Raman scattering

TEC thermoelectric cooler

ABSTRACT

Optical frequency combs have shown much potential in recent years to be a revolutionary tool in metrology, signals processing, and telecommunications. This dissertation is a record of our investigation of a single-section semiconductor laser diode as a portable and robust frequency comb source with the proper bandwidth and spectral coherence for spectroscopy applications. Our previous theoretical studies on stimulated Brillouin scattering demonstrated the predictive power of traveling wave models in pulsed and cascaded configurations, including calculations of Brillouin frequency comb generation. Utilizing this knowledge, a comprehensive theoretical model of semiconductor laser diodes was developed, including all carrier dynamics, cavity effects, and nonlinear phase shifts. Then, the physics and essential mechanisms of laser diode frequency comb generation were studied, focusing upon the frequency modulated nature of the output without any saturable absorber. Finally, InGaAsP / InP quantum well laser diodes, operating at 1.55 μm and 1.3 μm were fabricated and characterized, with designs specified by our theoretical models. The fabricated lasers exhibited comb behavior as predicted, generating combs with bandwidths of about 1 THz and RF linewidths of 100-250 kHz, both at 1.55 μm and 1.3 μm. These sources show much promise for spectroscopy and other frequency comb applications, paving the way toward integration in portable systems as a truly practical frequency comb source.

CHAPTER I

Introduction

The development of optical frequency comb technology has driven major advances in optical spectroscopy techniques and precision metrology [1]. The high phase coherence between the frequency comb modes allows easy transfer of information between the optical and RF frequency domains. This highly versatile trait enables many applications such as accurate measurements of atomic transitions [2], molecular spectroscopy [3], optical atomic clocks [4] and arbitrary waveform generation [5]. Using techniques such as self-referencing [6], a frequency comb by itself is a highly precise tool for measurement. With the advent of multiheterodyne spectroscopy, sometimes called dual-comb spectroscopy [7], multiple frequency combs can be used to greatly improve data acquisition time while maintaining high resolution by eliminating the need for delay lines or diffraction gratings. This technique can be applied at a distance, such as remote atmospheric sensing of greenhouse gases [8], or combined with multi-dimensional coherent spectroscopy (MDCS) [9] to quickly and accurately distinguish species in an inhomogeneous mixture [10]. The accuracy and simplicity improvements of frequency comb spectroscopy over conventional spectroscopy have the potential to improve nearly every field of science and industry. However, much of this potential is stymied by the fact that general access to portable and reliable frequency comb sources remains elusive. Many of the aforementioned experiments utilize sensitive and bulky mode-locked lasers for frequency comb sources, including erbium doped fiber [11] and Ti: Sapphire lasers [12]. A truly portable, battery operated chip-scale frequency comb source is a highly attractive platform for greatly expanding the utility of frequency comb spectroscopy beyond the confines of the laboratory.

In this thesis, we investigate the viability of generating frequency combs directly from single-section laser diodes. These lasers have much potential to be affordable and compact frequency comb sources for spectroscopy. These laser diodes produce frequency modulated (FM) frequency combs without a saturable absorber but with sufficient bandwidth and coherence for our spectroscopy applications. Moreover, they represent a solid-state solution that requires no moving mirrors or gratings, easier to operate compared to two-section lasers, and are mass producible via standard lithography methods.

This work can be split into three major sections in its study of frequency comb generation:

1. The first major section, consisting of chapters II through IV, can be thought of as an extended prologue. These chapters contain detailed theoretical studies into solving traveling wave equations with coupled forward and backward waves. In particular, we apply this theory to the nonlinear phenomenon of stimulated Brillouin scattering (SBS) and cascaded Brillouin scattering, touching upon SBS frequency combs in fibers and on-chip chalcogenide waveguides. This first section outlines important numerical techniques that will be essential in the next two sections.

2. The second major section, consisting of chapters V through VII, is the main theory of FM comb generation in single-section semiconductor laser diodes. Detailed semiconductor physics are derived from first principles with the resulting equations solved numerically to demonstrate the dynamics and physics of these laser devices. While we focus on quantum well (QW) devices, the theory can

be extended to other types of lasers including quantum dot (QD) and quantum cascade (QC) systems.

3. The third and last major section, consisting of chapters VIII and IX, moves away from theory and into experimental work. We utilize our semiconductor laser models to aid in designing and fabrication of QW laser diodes and characterize their performance and coherence. The experimental spectra and behavior are compared to theory with additional comments on the physics and behavior of real laser diodes.

Lastly, the dissertation concludes with a look at future directions and comments on the utilization of these laser diodes as a new source of frequency comb technology.

CHAPTER II

Maxwell's Wave Equation

When I first learned about Maxwell's equations in my applied physics days in undergrad, there was a joke about James C. Maxwell - by adding one term to one equation, Maxwell somehow, dubiously, managed to get all four equations named after him, despite some of those equations being previously named after other physicists. As it turns out, this naming may be justified as this small term became the key to describing light as oscillating electromagnetic waves. The wave equation for electric and magnetic fields is now the entire basis for modeling all sorts of physical phenomenon, including light propagation through matter. As the work presented in this thesis lies in the fields of nonlinear optics and semiconductor photonics, we therefore begin with Maxwell's wave equation.

2.1 Wave equation derivation

We start with the simple form of Maxwell's equations, assuming no free charges or currents.

$$\nabla \cdot \overline{\mathbf{D}} = 0 \tag{2.1a}$$

$$\nabla \cdot \overline{\mathbf{B}} = 0 \tag{2.1b}$$

$$\nabla \times \overline{\mathbf{E}} = -\frac{\partial \overline{\mathbf{B}}}{\partial t} \tag{2.1c}$$

$$\nabla \times \overline{\mathbf{H}} = \frac{\partial \overline{\mathbf{D}}}{\partial t} \tag{2.1d}$$

At this point, we can make the simplifying assumption that $\overline{\mathbf{H}} = \overline{\mathbf{B}}/\mu_0$, meaning there is no significant magnetic response of the material due to the fact we are modeling optical fields. Also, we rewrite the electric auxiliary field by its definition: $\overline{\mathbf{D}} = \epsilon_0\overline{\mathbf{E}} + \overline{\mathbf{P}}$, where $\overline{\mathbf{P}}$ is the induced material polarization, which can be linear and highly nonlinear depending on the material. Now we can decouple the variables by applying the curl to Equation 2.1c and substituting in Equation 2.1d, obtaining

$$\nabla \times \nabla \times \overline{\mathbf{E}} = -\mu_0\epsilon_0\frac{\partial^2 \overline{\mathbf{E}}}{\partial t^2} - \mu_0\frac{\partial^2 \overline{\mathbf{P}}}{\partial t^2}\,. \tag{2.2}$$

While Equation 2.2 contains all the essential pieces for calculating light interactions with matter, it requires a bit more simplification before it can be effectively used. The first problem occurs in simplifying the LHS - if the traditional vector identity is used,

$$\nabla \times \nabla \times \overline{\mathbf{E}} = \nabla(\nabla \cdot \overline{\mathbf{E}}) - \nabla^2\overline{\mathbf{E}}\,, \tag{2.3}$$

it is not obvious if $\nabla \cdot \overline{\mathbf{E}} = 0$, especially if $\overline{\mathbf{P}}$ is highly nonlinear. We can, however, approximate that $\nabla\cdot\overline{\mathbf{P}} \approx 0$, therefore allowing $\nabla\cdot\overline{\mathbf{E}} = 0$. Physically, this ignores some nonlinear transverse effects [13] [14], which are not important to the work presented in this thesis. Another way to to allow $\nabla \cdot \overline{\mathbf{E}} = 0$ is to treat the nonlinear portions of $\overline{\mathbf{P}}$ as a perturbation to the overall electric field propagation [15]. This approach is valid in many materials in which the nonlinear effects are rather weak, but may be somewhat dubious when strong nonlinearities are present. Either way, we use the vector identity with $\nabla \cdot \overline{\mathbf{E}} = 0$ and obtain the standard form of the traveling wave equation given by

$$\nabla^2 \overline{\mathbf{E}} - \frac{1}{c^2} \frac{\partial^2 \overline{\mathbf{E}}}{\partial t^2} = \mu_0 \frac{\partial^2 \overline{\mathbf{P}}}{\partial t^2} \, . \tag{2.4}$$

The second problem is that this equation is still too complex, as it is a full vector equation in three dimensions and in time. By applying further simplifications, we can reduce the wave equation into a first order, 1-D equation that is much simpler to solve, both analytically and numerically. We now assume that the electric field is transversely polarized in predominantly a single direction (arbitrarily x or y) and propagates in direction z. The polarization is separated into its linear and nonlinear parts, $\overline{\mathbf{P}} = \overline{\mathbf{P}}_L + \overline{\mathbf{P}}_{NL}$, in which we assume the nonlinear polarization will not significantly affect the eigenmodes of the system. Under these assumptions, the wave equation reduces to a scalar problem and can be solved using separation of variables. Separating the transverse derivatives from the propagation derivatives, we obtain

$$\left(\nabla_t^2 + \frac{\partial^2}{\partial z^2} \right) E - \frac{1}{c^2} \frac{\partial^2 E}{\partial t^2} = \mu_0 \frac{\partial^2 P_L}{\partial t^2} + \mu_0 \frac{\partial^2 P_{NL}}{\partial t^2} \, . \tag{2.5}$$

Here the operator ∇_t^2 is the transverse Laplacian. The linear polarization has the general form

$$P_L(\overline{\mathbf{r}}, t) = \epsilon_0 \int_{-\infty}^{\infty} d\tau \chi(t - \tau) E(\overline{\mathbf{r}}, \tau) \tag{2.6}$$

For the sake of simplicity, we will ignore the effect of material dispersion and assume that $\chi(t) = \chi\delta(t)$ so the polarization reduces to $P_L = \epsilon_0 \chi E(\bar{\mathbf{r}}, t)$. The material dispersion will be added later as second order dispersion when we model the semiconductor waveguides. In addition, the electric field is assumed to be in the following separable form, with a forward and backward propagating wave expanded around a center frequency and wave vector

$$E(\bar{\mathbf{r}}, t) = F_{xy}(x, y) e^{-i\omega_0 t} \left[E_+(z, t) e^{ik_0 z} + E_-(z, t) e^{-ik_0 z} \right] + c.c. \,. \tag{2.7}$$

Note that the expansions around ω_0 and k_0 are arbitrary and depend upon the specific system being modeled. We plug in Equation 2.7 into Equation 2.5 to obtain

$$\begin{aligned} &\left[E_+(z, t) e^{ik_0 z} + E_-(z, t) e^{-ik_0 z} \right] \nabla_t^2 F_{xy} + F_{xy} \frac{\partial^2}{\partial z^2} \left[E_+(z, t) e^{ik_0 z} + E_-(z, t) e^{-ik_0 z} \right] \\ &+ F_{xy} \frac{n_0^2}{c^2} e^{i\omega_0 t} \frac{\partial^2}{\partial t^2} e^{-i\omega_0 t} \left[E_+(z, t) e^{ik_0 z} + E_-(z, t) e^{-ik_0 z} \right] = \mu_0 e^{i\omega_0 t} \frac{\partial^2 P_{NL}}{\partial t^2} \,, \end{aligned}$$

$$\begin{aligned} \frac{1}{F_{xy}} \nabla_t^2 F_{xy} = &\frac{e^{i\omega_0 t} \mu_0 \frac{\partial^2 P_{NL}}{\partial t^2}}{F_{xy} \left[E_+(z, t) e^{ik_0 z} + E_-(z, t) e^{-ik_0 z} \right]} + \frac{\frac{\partial^2}{\partial z^2} \left[E_+(z, t) e^{ik_0 z} + E_-(z, t) e^{-ik_0 z} \right]}{E_+(z, t) e^{ik_0 z} + E_-(z, t) e^{-ik_0 z}} \\ &+ \frac{\frac{n_0^2}{c^2} e^{i\omega_0 t} \frac{\partial^2}{\partial t^2} e^{-i\omega_0 t} \left[E_+(z, t) e^{ik_0 z} + E_-(z, t) e^{-ik_0 z} \right]}{E_+(z, t) e^{ik_0 z} + E_-(z, t) e^{-ik_0 z}} \,. \end{aligned}$$

We have used the refractive index definition $n_0^2 = 1 + \chi$. The LHS now only depends on the transverse dimensions x,y, while if we ignore the effect of the nonlinear polarization on the transverse modes $F_{x,y}$, the RHS only depends on z and t. Thus from standard separation of variables theory, each side of the equation is equal to a constant, which we write as $-k^2$. We can now separate this equation into its transverse and longitudinal parts, which produces an eigenvalue equation (Helmholtz equation) and the pulse propagation equations. We separate the forward and backward waves in the pulse propagation equations by phase matching to the appropriate exponential term and apply the slowly-varying envelope approximation to obtain

$$\nabla_t^2 F_{xy} + k^2 F_{xy} = 0 \tag{2.8}$$

$$F_{xy}\frac{\partial E_+}{\partial z} + F_{xy}\frac{n_0^2\omega_0}{k_0 c^2}\frac{\partial E_+}{\partial t} + \frac{1}{2ik_0}F_{xy}E_+\left(k^2 - k_0^2 + \frac{n_0^2\omega_0^2}{c^2}\right) = \frac{\mu_0}{2ik_0}\frac{\partial^2 P_{NL}}{\partial t^2}e^{i\omega_0 t - ik_0 z} \tag{2.9a}$$

$$-F_{xy}\frac{\partial E_-}{\partial z} + F_{xy}\frac{n_0^2\omega_0}{k_0 c^2}\frac{\partial E_-}{\partial t} + \frac{1}{2ik_0}F_{xy}E_-\left(k^2 - k_0^2 + \frac{n_0^2\omega_0^2}{c^2}\right) = \frac{\mu_0}{2ik_0}\frac{\partial^2 P_{NL}}{\partial t^2}e^{i\omega_0 t + ik_0 z} \tag{2.9b}$$

Equation 2.8 can be solved to determine the effective propagation vector k depending on the transverse geometries. While we never solve Equation 2.8 explicitly, we assume there exists a set of normalized transverse modes F_{xy} which are used in determining spatial overlap integrals. However, Equations 2.9 are somewhat incomplete - they have extra terms that modify the wave propagation as well as not quite giving the correct group velocity. This problem stems from the slowly-varying envelope approximation, and can be dealt with by defining an explicit phase in the electric field [14]. Another way to get around this is to transform into frequency domain and make the appropriate expansion for $k(\omega)$. Because the latter approach is a little simpler, we apply this to Equations 2.9, approximating that $n_0 \approx n_g$, $k_0^2 - k^2 \approx \frac{n_0^2\omega_0^2}{c^2}$ to obtain

$$F_{xy}\frac{\partial E_+}{\partial z} + F_{xy}\frac{n_g}{c}\frac{\partial E_+}{\partial t} = \frac{\mu_0}{2ik_0}\frac{\partial^2 P_{NL}}{\partial t^2}e^{i\omega_0 t - ik_0 z} \tag{2.10a}$$

$$-F_{xy}\frac{\partial E_-}{\partial z}+F_{xy}\frac{n_g}{c}\frac{\partial E_-}{\partial t}=\frac{\mu_0}{2ik_0}\frac{\partial^2 P_{NL}}{\partial t^2}e^{i\omega_0 t+ik_0 z}\,. \tag{2.10b}$$

We can define v_g as the group wave velocity where $v_g = c/n_g$, and n_g is the group index.

Finally, we have a much simpler and usable set of equations for modeling light propagation in one direction. In the subsequent chapters, we will modify Equations 2.10 by specifying specific forms for the nonlinear polarization P_{NL} appropriate to each specific system. These traveling wave equations form the basis for all theoretical studies in this work.

2.2 Numerical solution method to traveling wave equations

In most applications, analytically solving the traveling wave equations is exceedingly difficult. Even solving them in steady state, there are few forms of the nonlinear polarization that will yield analytic solutions. Thus we must use numerical methods to solve these equations.

The method we use for all our solutions is integration along both forward and backward characteristics. This method is essential for systems that have significant forward and backward waves that interact with each other as well as clearly defined boundary conditions. In these systems, we cannot use conveniences such as moving reference frames as there are no convenient frames of reference with counter-propagating waves. Moreover, we cannot use split step methods as there are no easy ways to eliminate the boundaries for performing the numerical Fourier Transform. For three-wave scattering problems such as Stimulated Brillouin Scattering (SBS) or modeling Fabry-Perot cavity laser diodes, characteristic integration is clearly the best choice.

The characteristic curves for the first order traveling wave equation are simply straight lines, which are either forward or backward diagonals in the z and t axes. For

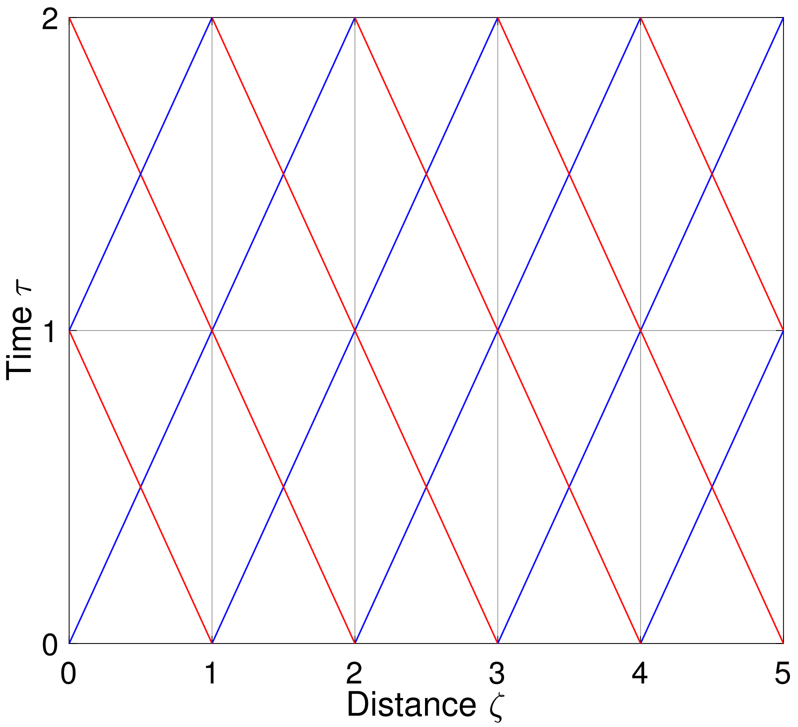

Figure 2.1: Plot of characteristic lines for the traveling wave equation. Blue lines are characteristics for the forward wave, while red lines are characteristics for the backward wave.

convenience, we rewrite the space and time variables as dimensionless, $\zeta = z/L$, $\tau = v_g t/L$, where L is the length of the system's domain. In Figure 2.1, the characteristics are plotted for the forward and backward waves in a space of length 5 units. If we define the characteristic lines as $\xi_+ = \frac{1}{2}(\zeta + \tau)$, $\xi_- = \frac{1}{2}(\tau - \zeta)$, Equations 2.10 can be rewritten as

$$F_{xy}\frac{\partial E_+}{\partial \xi_+} = \frac{\mu_0 L}{2ik_0}\frac{\partial^2 P_{NL}}{\partial t^2}e^{-ik_0 z} \tag{2.11a}$$

$$F_{xy}\frac{\partial E_-}{\partial \xi_-} = \frac{\mu_0 L}{2ik_0}\frac{\partial^2 P_{NL}}{\partial t^2}e^{ik_0 z}\,, \tag{2.11b}$$

with numerical integration following soon after. All we must do now is evaluate at the current time $\tau = \tau_0$ the RHS as the derivative along each characteristic, and then using an Euler stepping scheme or a collocation method [16] to evaluate the electric fields at the next time step $\tau = \tau_0 + \Delta\tau$. As an example, say we want to calculate the solutions of the traveling wave equations up to a time of $\tau = 2$ units, as depicted in Figure 2.1. We have discretized the ζ and τ domains with $\Delta\zeta = \Delta\tau = 1$ units. Starting at $\tau = 0$ on the ζ axis, at each ζ discretization the RHS of Equations 2.11 is evaluated, except at the boundaries ($\zeta = 0$, $\zeta = 5$). Here, only the forward wave's RHS is evaluated at $\zeta = 0$, and only the backward wave's RHS is evaluated at $\zeta = 5$. This is simply due to the fact that we stop tracking what happens to these waves once they propagate past the boundary. Once we have the derivative evaluations, we step forward in time (going up in the τ axis) and either to the right (forward wave) or to the left (backward wave) in space. Mathematically, we can write this in general form as

$$E_+(\zeta, \tau_0 + \Delta t) = \Delta\xi \left(\frac{\partial E_+}{\partial \xi_+}\right) |_{\zeta-\Delta\zeta,\tau_0} \tag{2.12a}$$

$$E_-(\zeta, \tau_0 + \Delta t) = \Delta\xi \left(\frac{\partial E_-}{\partial \xi_-}\right) |_{\zeta+\Delta\zeta,\tau_0} \,. \tag{2.12b}$$

The step size $\Delta\xi$ can be determined by its relations to Δt and Δz. We clearly see that $\Delta\xi = \frac{1}{2}(\Delta\tau + \Delta\zeta)$. However, Δt and Δz are not independent. For a wave traveling at speed v_g, the characteristic integration must satisfy the condition that the next spatial discretization is the at the distance traveled during the time step taken. In other words, $\Delta z = v_g \Delta t$ is a necessary relation for the characteristic integration. Using this relation, we find that $\Delta\tau = \Delta\zeta = \Delta z/L = v_g\Delta t/L$.

Once we calculate the fields at the next time step, we can now evaluate the boundary conditions for either waves reflecting (e.g. $rE_+(\zeta = 5) = E_-(\zeta = 5)$), or for external waves to enter the domain ($E_-(\zeta = 5) = E_{pump}$). This completes the calculation of all electric field values at time $\tau = 1$. This process can be repeated until we have reached the desired maximum simulation time.

While we have technically described the numerical process for solving traveling wave systems, implementation can be very difficult. The evaluation of the derivative can be tremendously costly, as for certain nonlinear systems we have to solve additional, coupled differential equations describing the dynamics of the material. Some examples include carrier equations in semiconductors, acoustic phonon or optical phonon equations, or Langmuir plasma waves. For our work in this dissertation, each system will be described in detail in their respective chapters.

2.3 Note on second-order derivatives

In later sections, we will be adding a second-order time derivative to the traveling wave equations. In the systems we model, this term represents a material or waveguide dispersion term and can be written

$$F_{xy}\frac{\partial E_+}{\partial z} + F_{xy}\frac{n_g}{c}\frac{\partial E_+}{\partial t} + i\frac{k''}{2}F_{xy}\frac{\partial^2 E_+}{\partial t^2} = \frac{\mu_0}{2ik_0}\frac{\partial^2 P_{NL}}{\partial t^2}e^{i\omega_0 t - ik_0 z} \tag{2.13a}$$

$$-F_{xy}\frac{\partial E_-}{\partial z} + F_{xy}\frac{n_g}{c}\frac{\partial E_-}{\partial t} + i\frac{k''}{2}F_{xy}\frac{\partial^2 E_-}{\partial t^2} = \frac{\mu_0}{2ik_0}\frac{\partial^2 P_{NL}}{\partial t^2}e^{i\omega_0 t + ik_0 z}\,, \tag{2.13b}$$

where k'' is the strength of the dispersive term. The second order derivative makes it more difficult to solve using the characteristics integration, but because in our systems the dispersion only plays a minor role, we can resolve it by using a predictor-corrector method. First, we solve the traveling waves without the dispersion term to "predict" the value of the electric fields at time $t + \Delta t$ utilizing the methodology in the previous section. This predicted value can now be used to evaluate the second-order time derivative using the finite difference formula

$$\frac{\partial^2 E_\pm}{\partial t^2} \approx \frac{E_\pm(t-\Delta t) + 2E_\pm(t) + E_\pm(t+\Delta t)}{(\Delta t)^2} \,. \tag{2.14}$$

Now the full derivative including dispersion can be calculated and used to evaluate the "correct" value of the electric fields. It is possible to use this new value of the electric field and perform the prediction-correction again - this iteration can be done as many times as desired. For our simulations, we use only a single correction step.

2.4 Note on two-point boundary value problems

The preceding sections describe what is in essence an initial value problem (IVP) with definite boundary conditions. The traveling wave equations are integrated from time $t = 0$ to a time $t = t_{\mathrm{max}}$, applying the boundary conditions at each step. While we are certainly interested in the dynamical behavior of the simulated systems, we are typically also very interested the steady state solutions and sometimes only care about the steady state solutions. The reader may wonder if it is possible to assume steady state conditions for the traveling wave equations and solve the following two-point boundary value problem (BVP):

$$F_{xy}\frac{dE_+}{dz} = -\frac{\omega_0^2\mu_0}{2ik_0}P_{NL} \tag{2.15a}$$

$$F_{xy}\frac{dE_-}{dz} = \frac{\omega_0^2\mu_0}{2ik_0}P_{NL} \,. \tag{2.15b}$$

Such an approach certainly looks attractive as the equations are now much simpler, no longer being partial differential equations but reduced to a single independent variable. However, looks can be highly deceiving. There are two major issues with attempting to solve the two-point BVP. The first is that all the dependent variables, the electric field and nonlinear polarization in this case, must actually have steady state solutions. Time harmonic wave solutions inherently carry around a complex exponential that represents phase and amplitude oscillations. If these exponentials are wittingly or unwittingly embedded in the electric field variables, then $\frac{\partial E_\pm}{\partial t}$ will never be zero, even if all material dynamics have died out. Thus the first step in solving the two-point BVP is ensuring that all dependent variables consist of only wave envelopes and that the rapidly varying exponentials are all separate beforehand. Such a process may not be desirable, however, as every electric field mode would have to have its own variable. For simulations of frequency combs in which there can be many modes, the calculations will be forced to keep track of not just each mode individually, but also the growing number of interaction terms that can easily make such simulations unruly.

The second issue, however, is that nonlinear two-point BVPs may not have unique solutions. The uniqueness of solutions to nonlinear IVPs has well defined conditions and even holds for fractional, nonlinear differential equations [17]. Numerically integrating nonlinear two-point BVPs can require an unknown number of numerical iterations before a solution is found [18]. Even worse, the resulting solutions may or may not even be unique, as they typically vary based upon the initial guess for the numerical methods in solving two-point BVPs. Calculation times are also costly: shooting methods involve iterations with Newton's method to find roots, while relaxation methods may or may not ever converge for nonlinear systems. Moreover, one may intuitively postulate that IVPs better imitate real scenarios than steady state BVPs (such as turning on a laser or studying dynamics of a pulse after it arrives).

For these reasons, we prefer the IVP over the BVPs in every instance with one exception: when the BVPs are simple enough to yield analytic solutions. Otherwise, despite the downsides of time domain calculations, solving the IVP is generally easier, quicker, and guarantees a unique solution.

CHAPTER III

Pulse Storage in Acoustic Waves via Stimulated Brillouin Scattering

Our first application of the traveling wave equations is for modeling Stimulated Brillouin Scattering (SBS). SBS is the phenomenon of light scattering off of an acoustic phonon in the medium, or light scattering from sound [19]. This is in contrast to Raman scattering, in which light scatters off optical phonons or molecular vibrations. The study of SBS in various media such as optical fibers [15] [20] and photonic chips [21, 22] has led to many diverse applications, including signals processing [23], pulse compression [24], and pulse storage and retrieval [25]. Some advantages of utilizing SBS are its low threshold and automatic phase matching [13].

We first review how the SBS equations are derived from the nonlinear polarization and then apply them to optical pulse storage and retrieval in optical fibers. At first, the optical pulses are transform limited but then we investigate the effects of frequency chirp on the efficiency of pulse storage.

3.1 Derivation of SBS equations for three waves

We begin with the first order traveling wave equations derived in Chapter I.

$$F_{xy}\frac{\partial E_+}{\partial z} + F_{xy}\frac{n_g}{c}\frac{\partial E_+}{\partial t} = \frac{\mu_0}{2ik_0}\frac{\partial^2 P_{NL}}{\partial t^2}e^{i\omega_0 t - ik_0 z} \tag{3.1a}$$

$$-F_{xy}\frac{\partial E_-}{\partial z} + F_{xy}\frac{n_g}{c}\frac{\partial E_-}{\partial t} = \frac{\mu_0}{2ik_0}\frac{\partial^2 P_{NL}}{\partial t^2}e^{i\omega_0 t + ik_0 z} \tag{3.1b}$$

For modeling SBS, the nonlinear polarization is

$$P_{NL} = \epsilon_0 \frac{\rho}{\rho_0}\gamma_e E\,, \tag{3.2}$$

where ρ_0 is the average material density, ρ is the deviation of the density from ρ_0, and

$$\gamma_e = \rho_0 \left(\frac{\partial \epsilon}{\partial \rho}\right)|_{\rho_0} \tag{3.3}$$

is the electrostrictive constant, or the change in material permittivity per density change. For convenience, we also expand the electric field into a forward pump wave and a backward wave that is shifted by an arbitrary frequency $\Delta\omega$,

$$E_+ = A_p \tag{3.4a}$$

$$E_- = A_s e^{i\Delta\omega t + i\Delta k z}\,. \tag{3.4b}$$

We insert Equations 3.2, 3.4 into Equation 3.1 and obtain

$$F_{xy}\frac{\partial A_p}{\partial z} + F_{xy}\frac{n_g}{c}\frac{\partial A_p}{\partial t} = \frac{\gamma_e \mu_0 \epsilon_0}{2ik_0\rho_0}e^{i\omega_0 t - ik_0 z}F_{xy}\frac{\partial^2}{\partial t^2}\Big[\rho(A_p e^{-i\omega_0 t + ik_0 z} + A_s e^{-i(\omega_0 - \Delta\omega)t - i(k_0 - \Delta k)z}\Big] \tag{3.5a}$$

$$-F_{xy}\frac{\partial A_s}{\partial z} + F_{xy}\frac{n_g}{c}\frac{\partial A_s}{\partial t} = \frac{\gamma_e \mu_0 \epsilon_0}{2ik_0\rho_0} e^{i(\omega_0-\Delta\omega)t+i(k_0-\Delta k)z} \times F_{xy}\frac{\partial^2}{\partial t^2}\left[\rho(A_p e^{-i\omega_0 t+ik_0 z} + A_s e^{-i(\omega_0-\Delta\omega)t-i(k_0-\Delta k)z}\right] . \tag{3.5b}$$

The material density obeys the acoustic wave equation [13]

$$\frac{\partial^2\rho}{\partial t^2} - \Gamma_A\nabla^2\frac{\partial\rho}{\partial t} - v_A^2\nabla^2\rho = -\epsilon_0\gamma_e\nabla^2(\overline{\mathbf{E}}\cdot\overline{\mathbf{E}}) . \tag{3.6}$$

Because the acoustic wave has its own dispersion relation that is derived from Equation 3.6, this greatly limits the possible phase-matching pairs on the RHS of Equations 3.5. For a bulk or nearly bulk materials, the acoustic wave has the simple dispersion relation $|\overline{\mathbf{q}}| = \Omega/v_A$, where $\overline{\mathbf{q}}$ is the acoustic wave vector and Ω is the acoustic wave frequency. If we assume the acoustic wave has the form $\rho = F_{A,xy}Q(z,t)e^{i|\overline{\mathbf{q}}|z-i\Omega t} + c.c.$, then by inspection, the RHS exponents are phase matched when $\Omega = \Delta\omega$ and $|\overline{\mathbf{q}}| = 2k_0 - \Delta k$. The phase matched acoustic frequency is also called the Brillouin frequency, labeled Ω_B. Using the acoustic dispersion relation, the Brillouin frequency is calculated to be

$$\Omega_B \approx \frac{2v_A}{v_g}\omega_0 . \tag{3.7}$$

Now returning to Equations 3.5, we keep only the phase matched terms and the equations reduce to

$$F_{xy}\frac{\partial A_p}{\partial z} + F_{xy}\frac{1}{v_g}\frac{\partial A_p}{\partial t} = \frac{\gamma_e \mu_0 \epsilon_0}{2ik_0\rho_0} e^{i\omega_0 t-ik_0 z} F_{A,xy}F_{xy}\frac{\partial^2}{\partial t^2}\left[QA_s e^{-i\omega_0 t-ik_0 z}\right] \tag{3.8a}$$

$$-F_{xy}\frac{\partial A_s}{\partial z} + F_{xy}\frac{1}{v_g}\frac{\partial A_s}{\partial t} = \frac{\gamma_e \mu_0 \epsilon_0}{2ik_0\rho_0} e^{i(\omega_0-\Delta\omega)t+i(k_0-\Delta k)z} F_{A,xy}F_{xy}\frac{\partial^2}{\partial t^2}\left[Q^* A_p e^{-i(\omega_0-\Delta\omega)t-i(k_0-\Delta k)z}\right] . \tag{3.8b}$$

We can apply the slowly-varying amplitude approximation once more to the RHS time derivative. Because the acoustic frequency Ω is typically much less than the optical frequency ω_0, we neglect both time derivatives of the envelopes. Lastly, we apply the transverse inner product $\int\int dxdyF_{xy}$ to Equations 3.8 in order to simplify the transverse functions.

$$\frac{\partial A_p}{\partial z} + \frac{n_g}{c}\frac{\partial A_p}{\partial t} = i\kappa_1 Q A_s \tag{3.9a}$$

$$-\frac{\partial A_s}{\partial z} + \frac{n_g}{c}\frac{\partial A_s}{\partial t} = i\kappa_1 Q^* A_p \tag{3.9b}$$

$$\kappa_1 = \frac{\omega_0^2 \gamma_e \left\langle F_{A,xy} F_{xy}^2 \right\rangle}{2k_0 \rho_0 c^2 \left\langle F_{xy}^2 \right\rangle} \tag{3.10}$$

The phase matching conditions can also be visualized as momentum conservation and energy conservation between the two optical waves and the acoustic wave. Figure 3.1 shows the $\overline{\mathbf{k}}$ vector phase matching for counter-propagating optical waves A_p and A_s with respective wave vectors $\overline{\mathbf{k}}_0$ and $\overline{\mathbf{k}}_s = \overline{\mathbf{k}}_0 - \Delta\overline{\mathbf{k}}$. We note that we only focus on backward SBS in this thesis as it is the more common phenomena due to phase-matching conditions. While it is possible for forward SBS to occur efficiently in confined structures [26], we predominantly work with bulk or nearly bulk acoustic behavior.

While Equations 3.9 are complete for the optical fields, we still must solve Equation 3.6 as it is coupled to the optical fields. There are considerable simplifications we can make to this equation, the biggest of them being the slowly varying amplitude approximation. We can plug in the assumed form of $\rho = F_{A,xy}Q(z,t)e^{i|\overline{\mathbf{q}}|z-i\Omega t} + c.c.$,

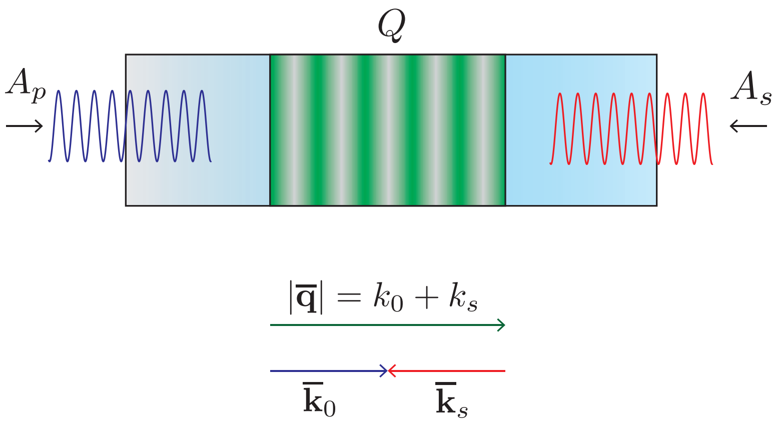

Figure 3.1: A schematic of backward SBS, with the forward wave A_p, backward wave A_s and acoustic wave Q labeled.

making the assumptions that

$$\begin{aligned}
\Omega &= \Omega_B \\
\frac{\partial^2}{\partial z^2}\frac{\partial \rho}{\partial t} &\approx i\Omega_B |\overline{\mathbf{q}}|^2 \rho \\
\frac{\partial^2 \rho}{\partial z^2} &\approx -|\overline{\mathbf{q}}|^2 \rho \\
\nabla^2(\overline{\mathbf{E}} \cdot \overline{\mathbf{E}}) &\approx -|\overline{\mathbf{q}}|^2 F_{xy}^2 (A_p A_s^* e^{i|\overline{\mathbf{q}}|z - i\Omega_B t})\,.
\end{aligned}$$

Putting it all together, Equation 3.6 becomes

$$-2i\Omega_B F_{A,xy}\frac{\partial Q}{\partial t} - i\Omega_B \Gamma_B F_{A,xy} Q = \epsilon_0 \gamma_e |\overline{\mathbf{q}}|^2 F_{xy}^2 A_p A_s^*\,, \tag{3.11}$$

where $\Gamma_B = |\overline{\mathbf{q}}|^2 \Gamma_A = 1/\tau_B$, the inverse acoustic lifetime. Rearranging some of the variables and operating once more with the transverse inner product, we finally obtain

$$\frac{\partial Q}{\partial t} + \frac{1}{2\tau_B} Q = i\frac{\epsilon_0 \gamma_e n_g \omega_0 \left\langle F_{A,xy} F_{xy}^2 \right\rangle}{v_A c \left\langle F_{A,xy}^2 \right\rangle} A_p A_s^*\,. \tag{3.12}$$

The electric fields can be normalized such that their magnitude squared is in units of power by rewriting

$$A_p \rightarrow \sqrt{\frac{2}{\epsilon_0 n_g c A_{eff}}} A_p \tag{3.13a}$$

$$A_s \rightarrow \sqrt{\frac{2}{\epsilon_0 n_g c A_{eff}}} A_s \,. \tag{3.13b}$$

This substitution affects the acoustic wave equation but does not change the optical wave equations.

$$\frac{\partial Q}{\partial t} + \frac{1}{2\tau_B} Q = i\kappa_2 A_p A_s^* \tag{3.14}$$

$$\kappa_2 = \frac{2\gamma_e \omega_0 \left\langle F_{A,xy} F_{xy}^2 \right\rangle}{v_A c^2 A_{eff} \left\langle F_{A,xy}^2 \right\rangle} \tag{3.15}$$

Lastly, to transform the Brillouin gain terms into a measurable quantity, we also normalize Q such that it too has units of power. We make the following substitution

$$Q \rightarrow 2i\tau_B \kappa_2 Q \tag{3.16}$$

Putting everything together, we obtain the following coupled three-wave SBS equations

$$\frac{\partial A_p}{\partial z} + \frac{n_g}{c}\frac{\partial A_p}{\partial t} = \frac{g_B}{2A_{eff}} Q A_s \tag{3.17a}$$

$$-\frac{\partial A_s}{\partial z} + \frac{n_g}{c}\frac{\partial A_s}{\partial t} = \frac{g_B}{2A_{eff}} Q^* A_p \tag{3.17b}$$

$$2\tau_B \frac{\partial Q}{\partial t} + Q = A_p A_s^* \,, \tag{3.18}$$

where $g_B = 4\kappa_1\kappa_2\tau_B A_{eff}$ is the Brillouin gain coefficient in units of m/W. We note that the acoustic wave is also called the Brillouin grating due to its periodic nature and how it acts as a grating to scatter light.

3.2 Optical pulse storage in acoustic waves

We apply Equations 3.17 and 3.18 to the problem of optical pulse storage, or transferring light energy into acoustic energy. Because the acoustic wave propagates much slower (or not at all relative to the speed of light), this energy transfer can be used as either temporary energy storage, optical delay lines or signals processing [25] [27] [23]. However, for these applications to be practical, the efficiency of generating the acoustic wave is paramount. This efficiency can be simulated in time domain using the three-wave SBS equations.

Pulse storage and retrieval is set up as follows. First, there is a pump ”signal” pulse that carries the information we would like to store. Next, there is a counter-propagating ”write” pulse that is down shifted in frequency by the Brillouin frequency ($\Omega_B \approx 10$ GHz in optical fibers), also called a Stokes wave (if the frequency shift is higher than the pump, it is called an anti-Stokes wave). These two pulses are sent from opposite ends of a medium, either an on-chip waveguide or an optical fiber. Once they collide, they beat together due to their frequency offset to generate the acoustic wave, transferring energy from the signal pulse to the acoustic wave. After the pulses exit, the acoustic wave stays in place and decays as the acoustic lifetime, storing the energy and information of the signal pulse. This process is shown schematically in Figure 3.2. In order to retrieve the stored information and energy, we can send in a third ”read” pulse at the same Stokes frequency as the write pulse. This third read pulse depletes the acoustic wave and transfers that energy back into a revived signal pulse. Physically, we can describe the whole process as two optical beams with a frequency offset beating together to engrave a grating into the material to store

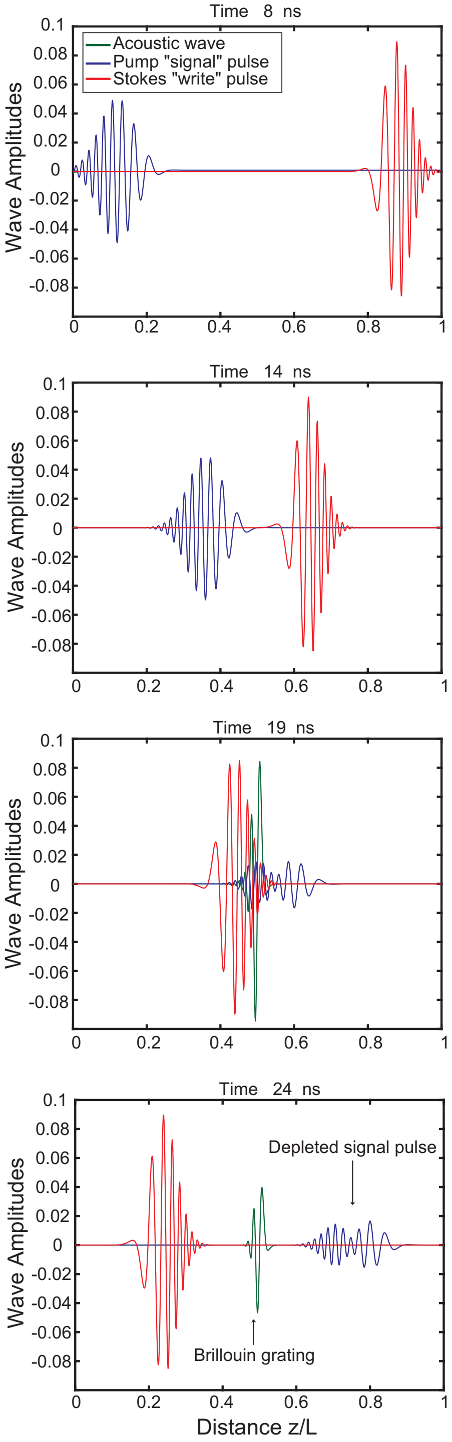

Figure 3.2: Plots of the signal and write pulses generating the acoustic wave or Brillouin grating. At first, the two pulses are separate but once they collide, they mix together to generate the Brillouin grating in the material, which exists even after the optical pulses exit.

Parameter	Description	Value
L	Length of fiber	5 m
τ_B	Brillouin lifetime	3.4 ns
g_B	Brillouin gain coefficient	3.56×10^{-11} m/W
λ	Vacuum wavelength	1.55 μ m
n_g	Refractive index	1.50
A_{eff}	Effective modal area	11 μm^2
τ_p	Pump (or signal) pulse width	2.0 ns
τ_s	Write (or Stokes) pulse width	1.5 ns

Table 3.1: Simulation parameters for SBS pulse storage and retrieval

information. Then a third beam comes in and scatters off of this grating to retrieve the information. We note that the write and read pulses are much larger than the signal and do not change much at all throughout the interaction. This allows for some simplifications in our later analysis.

We can simulate pulse storage by solving Equations 3.17 and 3.18 numerically in an optical fiber and study the interaction. The equations are solved numerically using integration along characteristics as described in Chapter II with a fourth order collocation scheme [16] for the electric fields and a simple Euler stepper for the acoustic wave equation. The pump A_p and write A_s pulses are sent in via boundary conditions of the form

$$A_p(t, z=0) = A_{p0} \exp\left[-\frac{1+iC_p}{2}\frac{t^2}{\tau_p^2}\right] \tag{3.19a}$$

$$A_s(t, z=L) = A_{s0} \exp\left[-\frac{1+iC_s}{2}\frac{t^2}{\tau_s^2}\right] . \tag{3.19b}$$

The pulses are Gaussian in form with a chirp parameter C_j, pulse width τ_j, and input pulse power $|A_{j0}|^2$ where $j = \{p, s\}$ for the pump or Stokes pulses. The use of chirped pulses was previously proposed to enhance the storage and readout efficiency and to achieve compression (hence higher signal to noise ratio) of the retrieved signal pulse [24]. The parameters used for the numerical calculations are listed in Table 3.1.

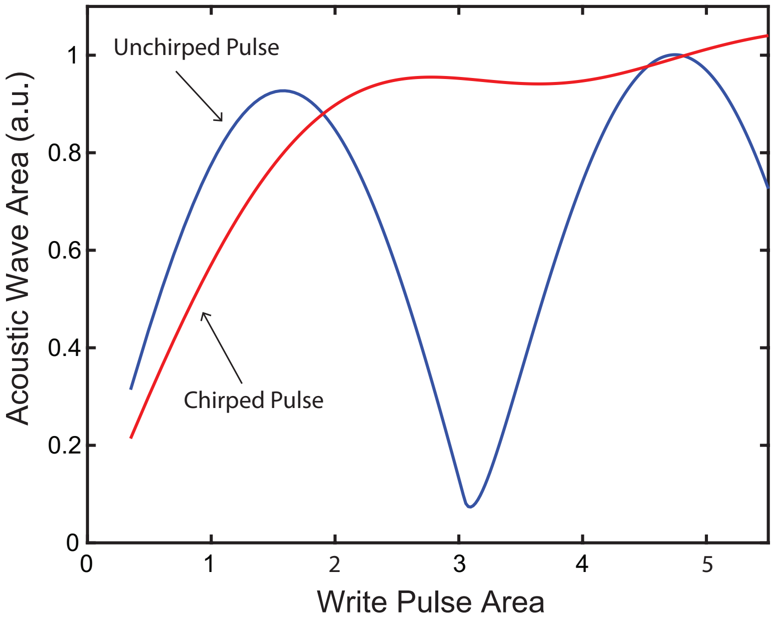

Figure 3.3: The efficiency of energy transfer into the acoustic wave (Q) as a function of write pulse area, for chirped and unchirped write pulses.

We first take a look at the efficacy of Brillouin grating generation as a function of write pulse power. However, we also define a "pulse area" for the write pulse of the form

$$\Theta_w = \sqrt{\frac{g_B c}{8A_{eff}\tau_B n_g}} \int A_s(t)dt \,, \tag{3.20}$$

whose importance will be seen shortly. We simulate the pulses for 30 ns with a pump pulse power of $|A_{p0}|^2 = 10$ mW and calculate the strength of the resulting acoustic grating while varying the area of the write pulse (Equation 3.20). The pulses have chirp parameters $(C_p, C_s) = (0, 0)$ for the unchirped case, and $(C_p, C_s) = (0, 3)$ for the chirped case. The strengths of the Brillouin gratings are plotted in Figure 3.3.

It is clear that using a chirped write pulse results in more robust Brillouin gratings as seen in the total energy of Q. In the case of using unchirped write pulses, the behavior is actually very similar to electron excitation in two-level atomic systems [14], in which a π-pulse must be used in order to efficiently excite atoms into the upper state. The analytic solution of unchirped pulse excitation is well-known for atomic systems and is derived in the three-wave SBS context [28] (also in plasma waves [29])

$$Q(z) \sim A_p(2z)\sin(\Theta_w) \tag{3.21}$$

Physically, this sinusoidal behavior can be understood by the Stokes and anti-Stokes scatterings in SBS. When the pulses first collide, their beating forms a Brillouin grating until the pump pulse is depleted. However, if the write pulse has not passed the spatial extent of the Brillouin grating once the pump is depleted (or it still has some "pulse area" left over), then the write pulse continues to interact with the Brillouin grating, this time via anti-Stokes scattering. The anti-Stokes scattering revives the pump pulse and depletes the grating, decreasing the efficiency of pulse storage. So when the write pulse has a π pulse area, this corresponds to the scenario in which the write pulse passes the Brillouin grating right as the pump is depleted. Moreover, this is a cyclical process: the pump can be fully depleted, revived, and then depleted again, which corresponds to a write pulse area of $3\pi/2$.

However, when the write pulses are chirped, the interaction becomes more complex. The chirped write pulse interacts with the pump pulse as before, but the Brillouin grating generated is only phase matched to the front portions of the write pulse frequency due to the chirp. As the tail of the write pulse moves through, the frequency is sufficiently detuned from the phase of the Brillouin grating that this suppresses the anti-Stokes process, thus preventing the depletion the acoustic wave and no energy is returned back into the signal.

Because the generation of the Brillouin grating using unchirped pulses is sinusoidal, we would much prefer using chirped write pulses to maintain high energy transfer. Despite the ease in changing pulse chirps in our calculations, making chirped pulses experimentally is not trivial. While the relatively long pulse lengths (∼1 ns) and low pulse powers (∼100-200 W) are easy to generate with conventional electronic components, the large frequency sweep per second needed for our chirps are more difficult. However, the chirp levels used (∼500 MHz/ns to 1 GHz/ns) can still be generated with more complex optical mode-locking schemes. There has been experimental demonstration of such chirps in passively mode-locked fiber lasers [30] and also diode-pumped fiber lasers [31] on the order of ∼ 10 GHz/ns to 1 THz/ns and should be well-suited for use as the write pulse.

3.3 Chirped pulse area theorem in the three wave interaction

We have seen that there exists an area theorem (Equation 3.21) when the write pulse is unchirped. In this section, we take a closer look at how this is derived and explore the connection to the two-level atomic system. In addition, we can derive a similar area theorem pertaining to using chirped pulses, although, as we shall see, this is considerably more difficult.

We return to the three-wave interaction equations (Equations Equations 3.17 and 3.18) and recast it into dimensionless units by making the substitutions $\zeta = z/L$, $\tau = \frac{v_g t}{L}$, $A_{p,s} \rightarrow \left(\frac{4A_{eff}\tau_B c}{g_B n L^2}\right)^{1/2} \tilde{A}_{p,s}$, $Q \rightarrow \frac{2A_{eff}}{g_B L}\tilde{Q}$. We also recast the spatial variable in the moving reference frame of the pump pulse A_2 with the variable $\xi = \zeta + \tau$ so traveling wave equations become

$$2\frac{\partial \tilde{A}_p}{\partial \xi} + \frac{\partial \tilde{A}_p}{\partial \tau} = -\tilde{Q}\tilde{A}_s \tag{3.22a}$$

$$\frac{\partial \tilde{A}_s}{\partial \tau} = \tilde{Q}^* \tilde{A}_p \tag{3.22b}$$

$$\frac{\partial \tilde{Q}}{\partial \tau} + \frac{\partial \tilde{Q}}{\partial \xi} = \tilde{A}_p \tilde{A}_s^* \,. \tag{3.22c}$$

To complete the transformation into a set of equations that resemble the two-level atomic system, we assume no depletion of the pump pulse, $\frac{\partial \tilde{A}_s}{\partial \tau} = 0$, that decay of $\tilde{Q}$ can be neglected (τ_B is large relative to the pulse collision time), and also $\tilde{A}_s$ is large and short in duration compared to $\tilde{A}_p$ such that the quasi-static approximation can be used [29]. Under the quasi-static approximation, the idea is that the time derivatives represent roughly how much the pulse shape changes on its own, while the ξ derivatives represent how quickly the pulse depletes under the SBS interaction. For very strong and short write pulses, $\frac{\partial}{\partial \xi} >> \frac{\partial}{\partial \tau}$ and the time derivatives in Equations 3.22 are also dropped. Under the quasi-static approximation and after another rescaling $\tilde{A}_s = \sqrt{2} A'_s$, $\tilde{Q} = \sqrt{2} q$, we obtain the following

$$\frac{\partial \tilde{A}_p}{\partial \xi} = -q A'_s \tag{3.23a}$$

$$\frac{\partial q}{\partial \xi} = \tilde{A}_p A'^{*}_s \,. \tag{3.23b}$$

Lastly, we simply write $A'_2 = |S| e^{i\theta}$, where $|S|$ is the shape of the undepleted write pulse and θ is the time-varying phase. Now make the substitutions $\theta = B - \pi/2$ and $|S| = A/2$ into the equations 3.23 to get

$$\frac{\partial \tilde{A}_p}{\partial \xi} = i \frac{A}{2} e^{iB} q \tag{3.24a}$$

$$\frac{\partial q}{\partial \xi} = i \frac{A}{2} e^{-iB} \tilde{A}_p \tag{3.24b}$$

Now it is clear that the pump pulse $\tilde{A}_p$ and the acoustic wave q are analogous to the two atomic levels, while the write pulse A'_s is analogous to the optical excitation pulse. These can be identified as $q \rightarrow c_1$, $\tilde{A}_p \rightarrow c_2$, where c_1 is the amplitude of the ground state and c_2 is the amplitude of the upper state. In this form, analytic solutions can be readily found for unchirped pulses where B does not vary in time or is zero. For initial conditions of $q(0) = 0$ and $\tilde{A}_p = A_{in}$, the solutions to Equations

3.24 are found by simply integrating to get

$$q(\zeta, \tau) = -i \sin\left(\int \frac{A}{2} d\xi\right) A_{in}(2\zeta) \tag{3.25}$$

The area of the write pulse $\int d\xi A/2$, can be rewritten out in terms of the original pulse A_s and making the transformation that $d\xi = \frac{c}{n_g L} dt$ to obtain

$$\Theta = \int \frac{A}{2} d\xi = \sqrt{\frac{g_B c}{8 A_{eff} \tau_B n_g}} \int |A_s(t)| dt \,, \tag{3.26}$$

which is the previously mentioned pulse area (Equation 3.20) with the major difference being the absolute value. For unchirped pulses, $|A_s| = A_s$ and the pulse areas are the same.

One peculiar aspect of Equation 3.25 is the factor of 2 in the argument of A_{in}. We note that this factor stems from the nature of the initial conditions applied, which are pulse profiles rather than simple constants as in the case of the two-level atom. Applying the initial condition of one wave to the solution of another, unrelated wave is a little more complex. A_{in} must satisfy initial conditions of propagation for the wave A_p, so it must have the form $A_{in}(\zeta - \tau)$. However, this cannot be the final propagation form of q, as the argument does not satisfy the acoustic wave propagation requirements. One way out of this conundrum is embedded as part of the aforementioned quasi-static approximation in which these pulse profiles are evaluated at a singular point when all three waves interact [29]. Under our current formulation, this point is the center of the write pulse, or $\xi = 0$. Using this expression, we can rewrite $A_{in}(\zeta - \tau) = A_{in}(2\zeta)$, which now satisfies the propagation requirements for q.

Going back to Equations 3.24, if we assume that the phase B is time dependent, then analytic solutions become much more difficult to obtain. Fortunately, there are some solutions that exist for specific forms of the write pulse profile [32] that we can utilize to our advantage. While our numerical simulations consist of Gaussian pulses and linear chirps, analytic solutions can be only be found for a similar, albeit slightly different, pulse shape of a sech pulse with a tanh chirp [33]. These functions are suitably close enough to warrant the usefulness of finding analytic solutions using the latter functional forms.

We can decouple Equations 3.24 with the phase B no longer constant and we get the following second order differential equation

$$q'' = i\left[-i\frac{A'}{A}q' + i\left(\frac{A}{2}\right)^2 q - B'q'\right] \tag{3.27}$$

$$q'' + q'\left(iB' - \frac{A'}{A}\right) + \left(\frac{A}{2}\right)^2 q = 0\,, \tag{3.28}$$

where here the primes indicate a $\frac{\partial}{\partial\xi}$ operation. If we let

$$A = \frac{\alpha}{\pi\xi_0}\,\mathrm{sech}\left(\frac{\xi-\xi_d}{\xi_0}\right) \tag{3.29}$$

$$B' = \frac{1}{\pi\xi_0}\left(\beta_0 - \beta\tanh\left(\frac{\xi-\xi_d}{\xi_0}\right)\right)\,, \tag{3.30}$$

the write pulse assumes the form of a sech pulse with pulse area α and chirp parameter β. We can vary the strength of the chirp of this pulse by varying β. Additionally, the parameter ξ_d is the pulse delay relative to the center of the reference frame and can be set to 0, while ξ_0 is a measure of the width of the write pulse. Now by also substituting in the hypergeometric constants

$$a = \frac{1}{2\pi}\left[(\alpha^2 - \beta^2)^{\frac{1}{2}} + i\beta\right] \tag{3.31}$$

$$b = \frac{1}{2\pi}\left[-(\alpha^2 - \beta^2)^{\frac{1}{2}} + i\beta\right] \tag{3.32}$$

$$c = \frac{1}{2}\left[1 + \frac{i}{\pi}(\beta_0 + \beta)\right] \tag{3.33}$$

$$z_h = \frac{1}{2}\left(1 + \tanh\left(\frac{\xi - \xi_d}{\xi_0}\right)\right) , \tag{3.34}$$

we can transform the equation 3.28 into the hypergeometric equation

$$z_h(1 - z_h)\frac{d^2q}{dz_h^2} + (c - (a + b + 1)z_h)\frac{dq}{dz_h} - abq = 0 . \tag{3.35}$$

This equation can be solved by looking into a handbook of mathematical functions [34]. The general solution in the range $0 < z_h < 1$ (corresponding to $-\infty < \xi < \infty$) is given by hypergeometric functions ${}_2F_1(a, b, c, z_h) = F(a, b, c, z_h)$

$$q = a_1F(a, b, c, z_h) + a_2z_h^{1-c}F(a + 1 - c, b + 1 - c, 2 - c, z_h) \tag{3.36}$$

The two constants a_1 and a_2 in Equation 3.36 are found by applying initial conditions for our two waves. First, we apply the initial condition that at $\tau \to -\infty$, $\xi \to -\infty$, $z_h \to 0$, the acoustic wave q is zero, thus we get $F(a, b, c, 0) = 1$ so $a_1 = 0$. The second initial condition is that the initial profile of the forward propagating pump wave must be taken into account. Solving for the second constant a_2 is significantly more difficult and involved. We present the steps below.

$$\begin{aligned}
\frac{\partial q}{\partial \xi} &= \frac{\partial q}{\partial z_h}\frac{\partial z_h}{\partial \xi} \\
\frac{dz_h}{d\xi} &= \frac{2}{\xi_0} z_h(1-z_h) \\
\frac{d}{dz_h}&(z_h^{c-1}F(a,b,c,z_h)) = (c-1)z_h^{c-2}F(a,b,c-1,z_h)
\end{aligned}$$

$$\frac{\partial q}{\partial \xi} = (1-c)z_h^{-c}F(a+1-c,b+1-c,1-c,z_h)\frac{2}{\xi_0}z_h(1-z_h)a_2 \tag{3.37}$$

We can use Equations 3.24 to relate this derivative to the initial input wave A_p. The variables A and B can be rewritten in terms of z_h after some effort:

$$\begin{aligned}
A &= \frac{\alpha}{\pi\xi_0} 2z_h^{1/2}(1-z_h)^{1/2} \\
B &= \frac{1}{\pi\xi_0}\int dz_h \frac{\xi_0}{2}\frac{1}{z_h(z_h-1)}(\beta_0 - \beta(2z_h-1)) \\
&= \frac{1}{2\pi}\left(\ln\left(z_h^{\beta+\beta_0}(1-z_h)^{\beta-\beta_0}\right)\right) + \phi_0
\end{aligned}$$

$$\begin{aligned}
\frac{\partial q}{\partial \xi} &= i\frac{A}{2}e^{-iB}\tilde{A}_p(\xi) \\
&= \frac{i\alpha}{2\pi\xi_0}(2z_h^{1/2}(1-z_h)^{1/2})z_h^{\frac{-i}{2\pi}(\beta_0+\beta)}(1-z_h)^{\frac{i}{2\pi}(\beta_0-\beta)}\tilde{A}_p(z_h)e^{-i\phi_0}
\end{aligned} \tag{3.38}$$

Here ϕ_0 is an arbitrary integration constant which represents an overall, constant phase of the backwards propagating Stokes wave which can be set to zero. Setting the two derivatives (Equation 3.37 and 3.38) equal to each other, we can solve for a_2

at $z_h = 0$.

$$\begin{aligned}(1-c)z_h^{-c}F(a+1-c,b+1-c,1-c,z_h)\frac{2}{\xi_0}z_h(1-z_h)a_2 \\ = \frac{i\alpha}{2\pi\xi_0}(2z_h^{1/2}(1-z_h)^{1/2})z_h^{\frac{-i}{2\pi}(\beta_0+\beta)}(1-z_h)^{\frac{i}{2\pi}(\beta_0-\beta)}\tilde{A}_p(z_h)\end{aligned}$$

$$\begin{aligned}(1-c)a_2z_h^{-c}F(a+1-c,b+1-c,1-c,z_h) &= \frac{i\alpha}{2\pi}z_h^{-\frac{1}{2}-\frac{i}{2\pi}(\beta_0+\beta)}(1-z_h)^{-\frac{1}{2}+\frac{i}{2\pi}(\beta_0-\beta)}\tilde{A}_p(z_h) \\ (1-c)a_2z_h^{-c}F(a+1-c,b+1-c,1-c,z_h) &= \frac{i\alpha}{2\pi}z_h^{-c}(1-z_h)^{-\frac{1}{2}+\frac{i}{2\pi}(\beta_0-\beta)}\tilde{A}_p(z_h) \\ (1-c)a_2 &= \frac{i\alpha}{2\pi}\tilde{A}_p(z_h=0)\end{aligned}$$

$$a_2 = \frac{i\alpha}{2\pi(1-c)}A_{in}(\zeta-\tau) \tag{3.39}$$

At last, we have solved for all unknowns in the solution to q (Equation 3.36). So the formal solutions for the three-wave SBS interaction with a chirped write pulse are found to be

$$\begin{aligned}\tilde{A}_p(\zeta-\tau) &= (1-z_h)^{1-c+a+b}F(a-c+1,b-c+1,1-c,z_h)A_{in}(\zeta-\tau) && \text{(3.40a)} \\ q(\zeta) &= \frac{i\alpha e^{-i\phi_0}}{2\pi(1-c)}z_h^{1-c}F(a-c+1,b-c+1,2-c,z_h)A_{in}(2\zeta)\,. && \text{(3.40b)}\end{aligned}$$

However, we are interested in the final result of the pulse storage interaction, as that ultimately determines the efficiency of pulse storage and retrieval. We take the limit as $z_h \to 1$ or equivalently, $\tau \to \infty$ when the pulses separate. There is a special relation between the hypergeometric function and the gamma function when $z_h = 1$, given by

$$F(a,b,c,1) = \frac{\Gamma(c)\Gamma(c-a-b)}{\Gamma(c-a)\Gamma(c-b)} \tag{3.41}$$

So taking the limit in Equation 3.40b, we get

$$q(\zeta) = \frac{i\alpha e^{-i\phi_0}}{2\pi(1-c)}(1)^{1-c}\frac{\Gamma(2-c)\Gamma(c-a-b)}{\Gamma(1-a)\Gamma(1-b)}A_{in}(2\zeta) \tag{3.42}$$

Equation 3.42 is still not very useful, as we may not always have readily available Γ function calculators. But there are some Γ function identities that can be applied to this expression to simplify it to elementary functions [34]

$$\begin{aligned}
\Gamma(z_h+1) &= z_h\Gamma(z_h)\\
\Gamma(z_h)\Gamma(-z_h) &= \frac{-\pi}{z_h\sin(\pi z_h)}\\
\Gamma(\frac{1}{2}+iy)\Gamma(\frac{1}{2}-iy) &= |\Gamma(\frac{1}{2}+iy)|^2 = \frac{\pi}{\cosh(\pi y)}\\
\Gamma(1-z_h)\Gamma(z_h) &= \frac{\pi}{\sin(\pi z_h)}\\
\Gamma(1-z_h) &= \frac{\pi}{\sin(\pi z_h)}\frac{1}{\Gamma(z_h)}\ .
\end{aligned}$$

So using plugging these into Equation 3.42 and also utilizing the fact that $-a = b^*$, $-b = a^*$, the magnitude of the acoustic wave or Brillouin grating is calculated to be

$$|q(\zeta)|^2 = \frac{\alpha^2}{4\pi^2|1-c|^2}|1-c|^2\frac{\Gamma(1-c)\Gamma(1-c^*)\Gamma(c-a-b)\Gamma(c^*-a^*-b^*)}{\Gamma(1-a)\Gamma(1-a^*)\Gamma(1-b)\Gamma(1-b^*)}|A_{in}(2\zeta)|^2$$

$$\begin{aligned}
|q(\zeta)|^2 = \frac{\alpha^2}{4\pi^2}&|\Gamma(\frac{1}{2}-\frac{i}{2\pi}(\beta_0+\beta))|^2|\Gamma(\frac{1}{2}+\frac{i}{2\pi}(\beta_0-\beta))|^2\\
&\times\frac{1}{\pi^4}\sin^2(\pi a)\sin^2(\pi b)\Gamma(a)\Gamma(a^*)\Gamma(b)\Gamma(b^*)|A_{in}(2\zeta)|^2
\end{aligned}$$

$$\begin{aligned}
|q(\zeta)|^2 = \frac{\alpha^2}{4\pi^2}&\frac{\pi}{\cosh(\frac{1}{2}(\beta_0+\beta))}\frac{\pi}{\cosh(\frac{1}{2}(\beta_0-\beta))}\\
&\times\frac{1}{\pi^4}\sin^2(\pi a)\sin^2(\pi b)\Gamma(a)\Gamma(-a)\Gamma(b)\Gamma(-b)|A_{in}(2\zeta)|^2
\end{aligned}$$

$$
\begin{aligned}
|q(\zeta)|^2 = \frac{\alpha^2}{4} \operatorname{sech}(\frac{1}{2}(\beta_0+\beta)) \operatorname{sech}(\frac{1}{2}(\beta_0-\beta)) \\
\times \frac{1}{\pi^4}\sin^2(\pi a)\sin^2(\pi b)\frac{-\pi}{a\sin(\pi a)}\frac{-\pi}{b\sin(\pi b)}|A_{in}(2\zeta)|^2
\end{aligned}
$$

$$
|q(\zeta)|^2 = \frac{\alpha^2}{4ab} \operatorname{sech}(\frac{1}{2}(\beta_0+\beta)) \operatorname{sech}(\frac{1}{2}(\beta_0-\beta)) \frac{1}{\pi^2}\sin(\pi a)\sin(\pi b)|A_{in}(2\zeta)|^2 \,,
$$

$$
\begin{aligned}
|q(\zeta)|^2 = \frac{\alpha^2}{4\pi^2 ab} \operatorname{sech}\left(\frac{1}{2}(\beta_0+\beta)\right) \operatorname{sech}\left(\frac{1}{2}(\beta_0-\beta)\right) \\
\times \sin\left(\frac{1}{2}\Phi + i\frac{\beta}{2}\right)\sin\left(-\frac{1}{2}\Phi + i\frac{\beta}{2}\right)|A_{in}(2\zeta)|^2 \,,
\end{aligned}
\tag{3.43}
$$

where $\Phi = (\alpha^2-\beta^2)^{1/2}$. We note that $-ab = \frac{\alpha^2}{4\pi^2}$ which allows q to remain dimensionless. For our write pulses, the chirp strengths are not large relative to the pulse area, meaning $\alpha > \beta$. Under this assumption, we can simply Equation 3.43 into its final form

$$
\begin{aligned}
|q(\zeta)| = \sqrt{\operatorname{sech}\left(\frac{1}{2}(\beta_0+\beta)\right) \operatorname{sech}\left(\frac{1}{2}(\beta_0-\beta)\right)} \\
\times \sqrt{\sin^2\left(\frac{\Phi}{2}\right)\cosh^2\left(\frac{\beta}{2}\right) + \sinh^2\left(\frac{\beta}{2}\right)\cos^2\left(\frac{\Phi}{2}\right)}|A_{in}(2\zeta)|
\end{aligned}
\tag{3.44}
$$

Equation 3.44 is our main result for this section. This equation determines the final Brillouin grating strength for a Gaussian-like write pulse with a linear-like chirp.

Plots of Equation 3.44 are shown in Figure 3.4 for varying values of write pulse chirp β. At $\beta = 0$, this corresponds to the case of the unchirped write pulse. If we plug in $\beta_0 = \beta = 0$ into Equation 3.44, the solution for $|q|$ reduces to

$$
|q(\zeta)| = \sin\left(\frac{\alpha}{2}\right)|A_{in}(2\zeta)| \tag{3.45}
$$

which matches our previous solution (Equation 3.25) for unchirped write pulses.

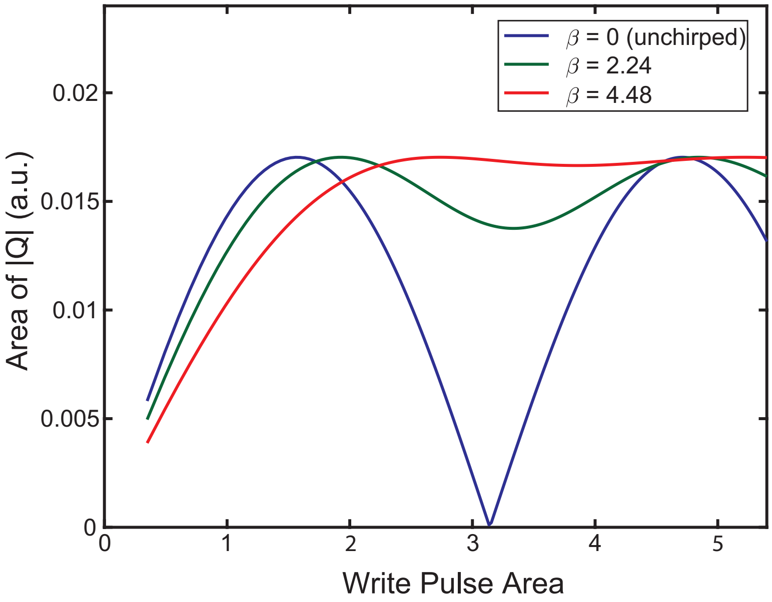

Figure 3.4: Plots of the analytic solution (Equation 3.44). The plots represent the Brillouin grating strength, a measure of energy transfer into the acoustic wave, at varying values of β the write pulse chirp.

Lastly, we verify that this analytic solution is indeed accurate for the case of Gaussian pulses with linear chirp by numerically solving Equations 3.17 and 3.18 with varying write pulse chirps. The chirp codes are defined as (C_1, C_2) where C_1 is the chirp of the pump pulse (no chirp in this case) and C_2 as the chirp of the write pulse. The results are shown in Figure 3.5, with very good agreement with the analytic results. The chirp strength $C_2 = 1, 2$ roughly corresponds with the values of $\beta = 2.24, 4.48$. Even though the analytic results are the product of sech and tanh pulse shape and chirp respectively, they still produced plots that are highly predictive of Gaussian pulse behavior.

3.4 Conclusion

In summary, we have found that chirping the pulses can produce very different behaviors of how the acoustic wave is generated in the SBS interaction. Overall, the use of chirped pulses should result in more efficient and robust generation of SBS.

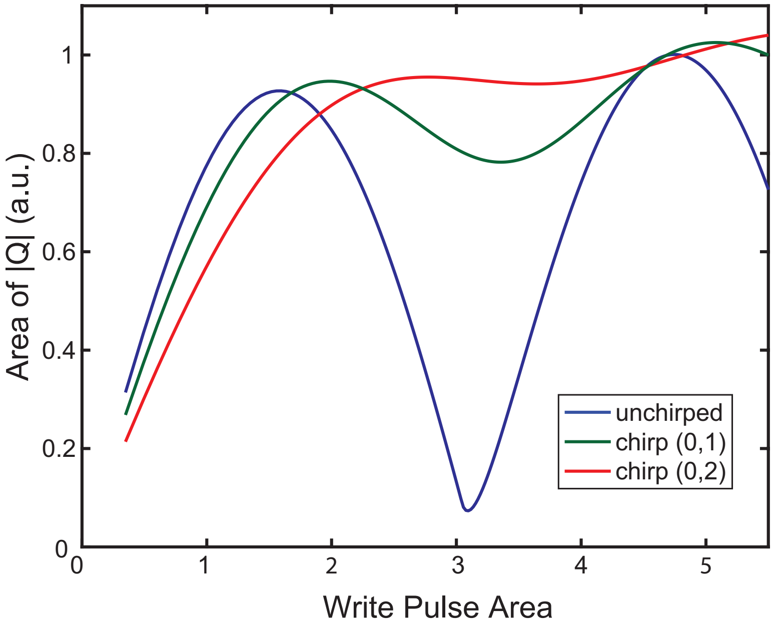

Figure 3.5: The efficiency of energy transfer into the acoustic wave numerically calculated for several write pulse chirps.

Analytic results from the use of the quasi-static approximation have confirmed the nature of using chirped pulses, which match well with our numerical calculations. The behavior of chirped pulses has been experimentally investigated in quantum dots in which chirped pulses were used for much more robust excitation [35], whose efficiencies followed the same behavior as predicted by our analytic results. Despite the fact that our derivation is applied in the context of SBS, Equations 3.24 are quite general and can apply to any three-wave interaction platform. In theory, the chirped pulse result in Equation 3.44 should be applicable to Raman scattering and plasma wave excitation as well.

CHAPTER IV

Frequency Combs from Cascaded Stimulated Brillouin Scattering

One interesting aspect of SBS is that it can be cascaded to generate many electric field modes, forming the basis of a frequency comb, or frequency modulation for signals processing. These have been demonstrated on-chip and in fibers utilizing both backward and forward scattering [36, 37, 38, 39, 26]. While the coherence and bandwidth of such combs need to be further investigated for practical use, the phenomenon of cascaded Brillouin scattering at the tens of GHz frequencies has potential to affect microwave photonics, wavelength-division multiplexing, and other sensing applications.

This chapter focuses on our modeling work on cascaded SBS. We develop a new, more unified and complete approach to modeling SBS [40] with ideas and principles that, as we see later, extend to modeling more complex frequency combs in semiconductor laser diodes.

4.1 Modeling cascaded Brillouin scattering

As the reader may have noticed from the previous chapter, the modeling efforts of nonlinear optical effects, including SBS, typically extract any rapidly varying phases from the electric field envelope. In such a scheme, all envelopes in the calculation are free from any complex exponentials and will typically have a steady state solution (not oscillating to infinity). This type of formulation is common for second and third harmonic generation, sum-difference frequency generation, and four-wave mixing (FWM) [13] [41]. The convenience and practical necessity of separating these envelopes allow us to define separate refractive indices for waves at vastly different frequencies, as well as not having to potentially use subwavelength time steps for numerical calculations.

However, such a formulation becomes unruly for a large number of frequencies present in a system, especially when they all interact at the same time. For cascaded Brillouin scattering, in which multiple modes are generated in both the forward and backward directions, separating each envelope quickly becomes untenable as the number of modes exceeds even three or four frequencies. In previous work on Brillouin combs, the authors would have to solve multiple coupled differential equations for just a few cascaded Brillouin modes [36], with Ogusu solving 14 equations in the work [42]. Moreover, there have been experiments with about 800 modes generated from cascaded Brillouin scattering [38], which could require more than 3200 coupled differential equations to model.

To see how the number of equations can grow so quickly, let us assume we have only three modes, a center mode with forward wave A_0, and backward wave B_0, and two adjacent side modes $A_\pm, B_\pm$. Immediately, we would need six traveling wave equations just to describe the three electric field frequencies. However, we still need to account for the acoustic wave equations. We would need an equation for the scattering from A_0 to B_{-1} as we did before, but now we also need an equation for A_1 to B_0, particularly if this frequency spacing is slightly different. However, we are still not done, as there could be Stokes scattering from the backward direction to the forward direction via B_1 to A_0 or B_0 to A_{-1}, which would require two additional backward

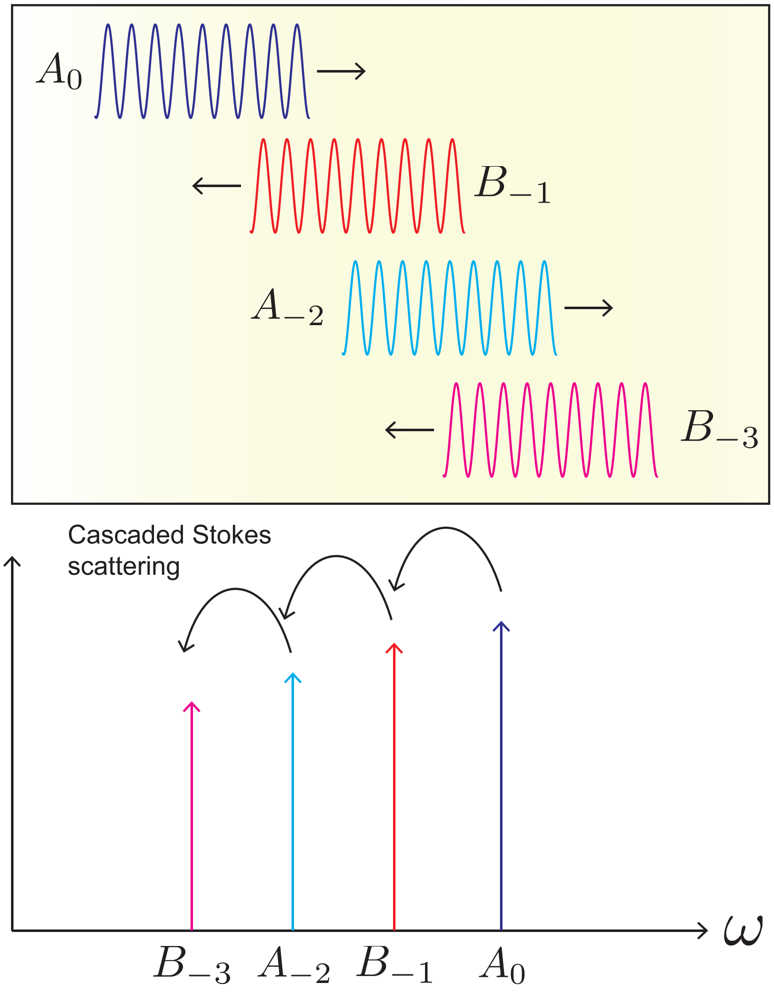

Figure 4.1: A diagram showing the nature of cascaded Brillouin scattering. An input forward wave A_0 can scatter into the Stokes wave B_{-1}, which can then scatter again to form A_{-2} etc. The frequency shifts down with each wave due to Stokes scattering, shifting by the Brillouin frequency Ω_B with each mode.

acoustic wave equations. So we have a total of 10 coupled differential equations for only three cascaded Brillouin modes. The number of equations would simply balloon as more modes are added, as there would be a growing amount of combinations of scatterings possible. Numerical solutions to these coupled equations would eventually run into problems due to the tremendous amount of coupling between all the differential equations.

We instead opt for a different approach to modeling cascaded SBS. The central idea is that, because the Brillouin frequency shift is quite small relative to optical frequencies and that optical parameters like refractive index are roughly constant and dispersion is negligible, we should be able to easily calculate the traveling wave and acoustic dynamics without overly tiny time steps. We would only need time steps that can resolve the GHz acoustic response rates and electric field modulations. In this formulation, the electric field variables can retain oscillating exponential terms, denoting frequency shifts on the order of the Brillouin frequency, without having to separate each frequency exponent. This allows a single electric field variable to describe many frequencies and modes, as long as they can be approximated with the same propagation characteristics and group velocity.

In other words, if we wish to numerically resolve the following solution

$$E(z,t) = E(z)e^{i\Omega_B t}\,, \tag{4.1}$$

where Ω_B is the Brillouin frequency, we would only need time steps smaller than $\sim 1/\Omega_B$ (and not $1/\omega_0$ the optical frequency) which puts us at the picosecond time step regime. Since time steps of this size are taken anyway in modeling SBS [28], we have much to gain by adopting the multimode approach.

4.2 Mathematical formulation of multimode SBS equations

Mathematically, formulating the electric field variables for multimode operation is straightforward - we simply retain the time harmonic exponentials that are in the range of the Brillouin frequency while extracting the central exponential with the optical frequency. Going back to Equations 3.1 in which we have already extracted the exponential $e^{-i\omega_0 t}$, we leave the electric field variables as is. In this case, the subsequent steps become

$$F_{xy}\frac{\partial E_+}{\partial z} + F_{xy}\frac{n_g}{c}\frac{\partial E_+}{\partial t} = \frac{\gamma_e \mu_0 \epsilon_0}{2ik_0\rho_0} e^{i\omega_0 t - ik_0 z} F_{xy}\frac{\partial^2}{\partial t^2}\left[\rho(E_+ e^{-i\omega_0 t + ik_0 z} + E_- e^{-i\omega_0 t - ik_0 z}\right] \tag{4.2a}$$

$$\begin{aligned} -F_{xy}\frac{\partial E_-}{\partial z} + F_{xy}\frac{n_g}{c}\frac{\partial E_-}{\partial t} &= \frac{\gamma_e \mu_0 \epsilon_0}{2ik_0\rho_0} e^{i\omega_0 t + ik_0 z} \\ &\quad \times F_{xy}\frac{\partial^2}{\partial t^2}\left[\rho(E_+ e^{-i\omega_0 t + ik_0 z} + E_- e^{-i\omega_0 t - ik_0 z}\right] . \end{aligned} \tag{4.2b}$$

Now, instead of expanding ρ like we did in Chapter III, we do not assume any explicit operating frequency. However, we extract the propagation vector $\overline{\mathbf{q}}$ with magnitude $2k_0$ for spatial phase matching

$$\rho = F_{A,xy} Q(z,t) e^{i|\overline{\mathbf{q}}|z} + c.c. . \tag{4.3}$$

The resulting material equation is a bit more complex, as we can no longer eliminate the time derivatives as those oscillating exponentials are contained in the variable $Q(t)$,

$$F_{A,xy}\frac{\partial^2 Q}{\partial t^2} - F_{A,xy}\Gamma_A|\overline{\mathbf{q}}|^2\frac{\partial Q}{\partial t} - F_{A,xy}v_A^2|\overline{\mathbf{q}}|^2 Q = -\epsilon_0\gamma_e\nabla^2(\overline{\mathbf{E}}\cdot\overline{\mathbf{E}}) . \tag{4.4}$$

From here, we follow similar procedures as those outlined in Chapter III, collecting phase-matched terms and rewriting the field variables in terms units of power, with the forward wave $A(z,t)$ and backward wave $B(z,t)$. The result consists of only three equations in the form

$$\begin{aligned} \frac{\partial A}{\partial z} + \frac{n_g}{c}\frac{\partial A}{\partial t} &= \frac{g_B}{2A_{eff}} QB && \text{(4.5a)} \\ -\frac{\partial B}{\partial z} + \frac{n_g}{c}\frac{\partial B}{\partial t} &= -\frac{g_B}{2A_{eff}} Q^* B && \text{(4.5b)} \\ \left[\frac{\partial^2}{\partial t^2} + \frac{1}{\tau_B}\frac{\partial}{\partial t} + \Omega_B^2\right] Q &= \left(\frac{4i\Omega_B}{\tau_B}\right) AB^* \,. && \text{(4.5c)} \end{aligned}$$

To complete the derivation, we add in the physical effects of linear loss, Kerr effect [15], and noise [43, 44]. The final set of equations describing a more generalized SBS process is written

$$\begin{aligned} \frac{\partial A}{\partial z} + \frac{n_g}{c}\frac{\partial A}{\partial t} =& \frac{g_B}{2A_{eff}} QB - \frac{\alpha}{2} A + i\gamma\left(|A|^2 + |B|^2\right) A && \text{(4.6a)} \\ -\frac{\partial B}{\partial z} + \frac{n_g}{c}\frac{\partial B}{\partial t} =& -\frac{g_B}{2A_{eff}} Q^* B - \frac{\alpha}{2} B + i\gamma\left(|A|^2 + |B|^2\right) B && \text{(4.6b)} \\ \left[\frac{\partial^2}{\partial t^2} + \frac{1}{\tau_B}\frac{\partial}{\partial t} + \Omega_B^2\right] Q =& \left(\frac{4i\Omega_B}{\tau_B}\right) AB^* + \tilde{f} \,, && \text{(4.6c)} \end{aligned}$$

where γ is the third-order nonlinear coefficient, $\tilde{f}$ is the Langevin noise term, and α is the linear loss per length.

There are a few interesting features about the formulation in Equations 4.6. We note that the acoustic wave equation takes on the form of a simple harmonic oscillator with resonance frequencies at $\pm\Omega_B$. While the driving term on the RHS of the oscillator can theoretically be of any frequency, the acoustic wave will only be appreciably large when it is driven on resonance. Also, because of the way ρ is formulated, the $+\Omega_B$ resonance corresponds to backward propagating acoustic waves, while the $-\Omega_B$ resonance corresponds to the forward propagating acoustic wave. Both resonances will be present and significant in more complex interactions with multiple forward and backward electric field modes. Other features of these equations include the dynamic incorporation of the Brillouin gain lineshape, which in frequency domain consists of peaks at the resonances $\pm\Omega_B$ with linewidth Γ_B, yielding a gain bandwidth of about 30 MHz. Moreover, physical effects such as all anti-Stokes scattering possibilities and every possible four-wave mixing pair between the electric field modes are automatically included as well. The strengths of the modes depends upon the gain of the various modes at phase-matched frequencies that is automatically built into Equations 4.6.

There is a similar multimode approach for the 1-D Lugiato-Lefever equation (LLE) [45] in which additional modes are modeled as phase modulations to the electric field envelope. Modeling microresonator combs with the LLE can span up to an octave with hundreds of modes. However, the LLE is rather simple compared to the SBS equations, as there is no acoustic wave in the LLE and the fields are unidirectional, which makes solving them much easier compared to the case of SBS with counter-propagating waves.

4.3 Numerical solutions to multimode SBS equations

Now that we have arrived at a unified set of only three equations (Equations 4.6) that compactly describes all possible cascaded backward SBS between optical modes, including Stokes and anti-Stokes scatterings, we put our theory to the test with some numerical experiments modeled after some actual experiments already published. The parameters of these simulations are given in Table 4.1. We focus our numerical calculations on two different systems: SBS in silica fibers, and SBS in chalcogenide glass. Equations 4.6 are solved using the same characteristics integration described in Chapter II and collocation method [16] for the electric fields. However, the second-order acoustic wave equation is now solved using a 5th order predictor corrector based upon Adams-Bashforth-Moulton coefficients [18], which yields fairly accurate and stable solutions to the harmonic oscillator equation.

Our first numerical study is a simple backward SBS setup, in which we send

Parameter	Description	Silica	Chalcogenide Glass
L	Length of device	10 m	38.6 cm
τ_B	Brillouin lifetime	3.4 ns	12 ns
Ω_B	Brillouin frequency shift	$2\pi \times 9.44$ GHz	$2\pi \times 7.8$ GHz
g_B	Brillouin gain coefficient	1.78×10^{-11} m/W	6.1×10^{-9} m/W
n_g	Refractive index	1.50	2.81
A_{eff}	Effective modal area	11 μm^2	56 μm^2
γ	Third order nonlinear coefficient	$11.5 \times 10^{-3}(\text{Wm})^{-1}$	$1.737(\text{Wm})^{-1}$
α	Linear loss coefficient	0.0064 m^{-1}	0.1935 m^{-1}

Table 4.1: Simulation parameters for cascaded SBS in fibers and chalcogenide glass.

a CW pump with 5 W power into a 10 m silica optical fiber. This is done via a boundary condition such that $|A(z = 0, t)|^2 = 5\text{W}$. The transmitted wave, the forward-propagating light that emerges from the back facet $|A(z = L, t)|^2$, and the reflected wave, the backward-propagating light that emerges from the front facet $|B(z = 0, t)|^2$, are plotted in Figure 4.2. The temporal outputs show the relative stability of the transmitted and reflected waves, but the spectrum shows that the backward wave has a clear frequency offset due to the presence of an exponential phase shift. In other words, the backward wave $B(z, t)$ has downshifted relative to the forward pump wave $A(z, t)$ by a frequency offset, and we find that this frequency shift is precisely equal to the Brillouin frequency Ω_B.

Although this is a simple calculation, it demonstrates some features of our formulation. Instead of having to specify beforehand that the backward wave is downshifted by the Brillouin frequency, this shift is automatically calculated from the acoustic wave equation (Equation 4.6c) and applied as a phase modulation. But perhaps the most powerful part is that we no longer need to know *apriori* which electric field modes will be significant for each SBS interaction, as under the old formulation, we had to assign them separate variables in order to know whether they will grow or not. In the new approach, significant modes can be seen simply by taking a Fourier transform and looking at the strength of each line.

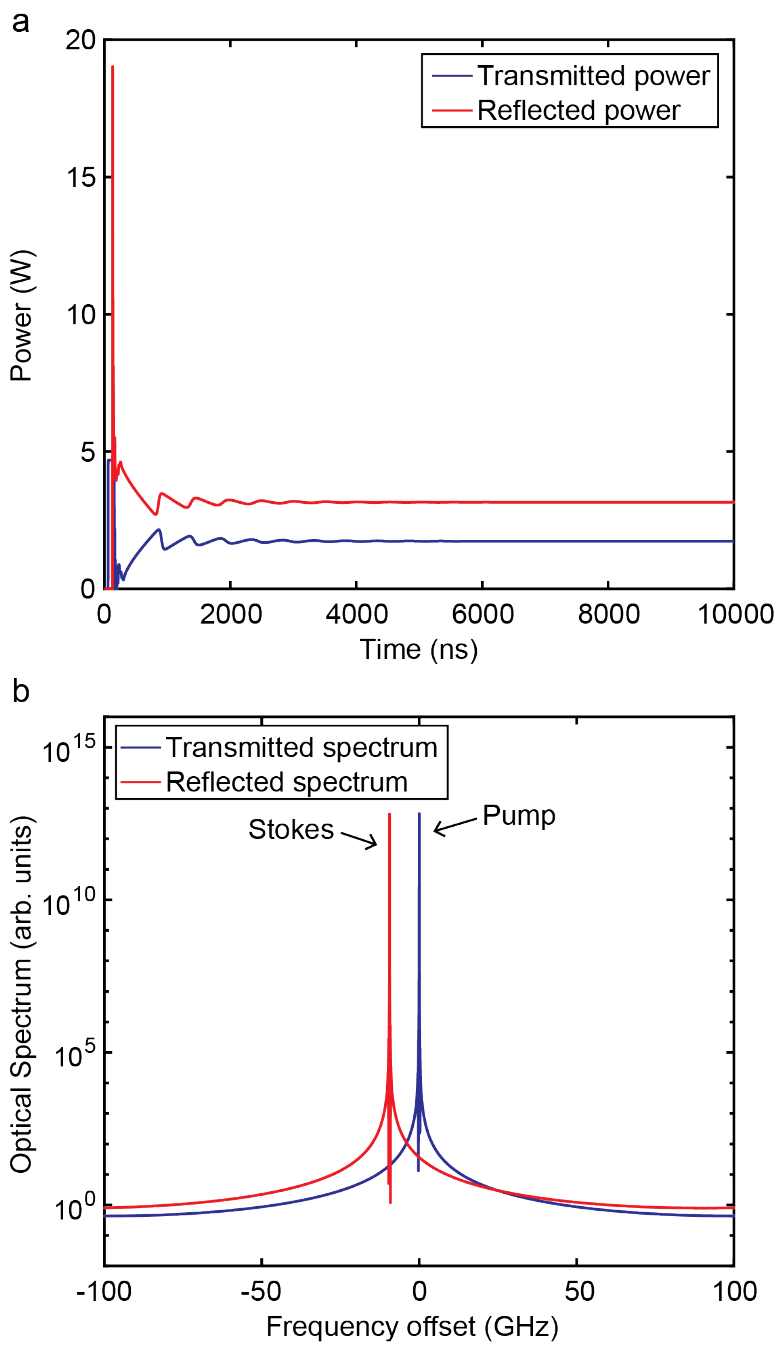

Figure 4.2: a) Temporal output and b) spectra for a 5-W cw pump in a 10-m silica fiber without facet reflections.

Our next study is similar to the first, but now the input pump is 150 W instead of 5 W. This number is chosen as it just exceeds the threshold of the emergence of a second order Stokes line, found to be about 130 W [46]. The threshold power for

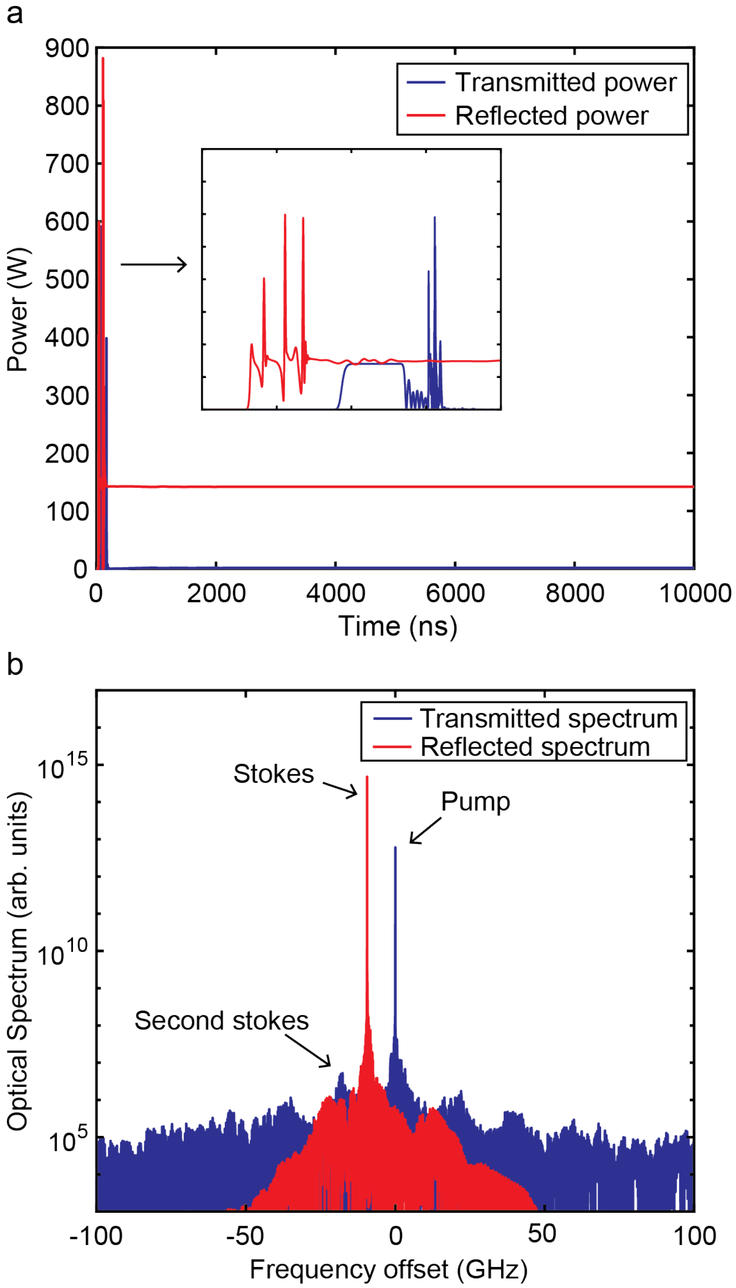

Figure 4.3: a) Temporal output and b) spectra for a 150 W cw pump in a 10-m silica fiber without facet reflections. Note the emergence of a second Stokes line, albeit very weak.

SBS is approximated as

$$P_{th} = 21\frac{A_{eff}}{g_B L_{eff}} \tag{4.7}$$

$$L_{eff} = \frac{1-e^{-\alpha L}}{\alpha}\,. \tag{4.8}$$

For the first Stokes scattering, the effective length is roughly equal to the total length of the fiber, especially due to very low losses. The threshold power greatly decreases as the length of the fiber increases, causing issues in amplifiers and long distance communications that require some engineering to suppress all SBS [47]. However, while the first order Stokes scattering is relatively easy to obtain, the second Stokes scattering has considerably higher threshold. The length traversed by the first backward Stokes wave is typically much shorter, on the order of 1% of the original length for a fully depleted pump. By sending in 150 W, we are able to see a second Stokes line emerge in Figure 4.3. Once more, we did not need to specify any additional variable for this second order Stokes wave but rather it shows up naturally as a phase modulation of A at $2\Omega_B$.

There is a way to greatly reduce the threshold of cascaded SBS for the generation of additional modes. Having facet reflections or internal reflections of any sort restores L_{eff} to its original value along the fiber. For the next study, we change the front facet to be reflecting by modifying the boundary condition to

$$A(z=0,t) = -rB(z=0,t)\,, \tag{4.9}$$

where $|r|^2 = 0.20$, a 20% reflection coefficient. In this case, the backward Stokes waves will be fed back into the forward wave $A(z,t)$ in which they can scatter once more or mix together via FWM to produce entirely new frequencies. We reduce the pump power to 5 W once more and monitor the outputs of the fiber, shown in Figure 4.4. Many more modes emerge, both in the forward and backward directions, with the forward spectrum having many more modes due to longer FWM interaction lengths from the front reflecting facet. The temporal output shows mostly a sinusoidal output from the beating of the pump and first order Stokes, while the spectrum shows several other modes at much lower magnitudes. We see about 10-11 distinct frequencies,

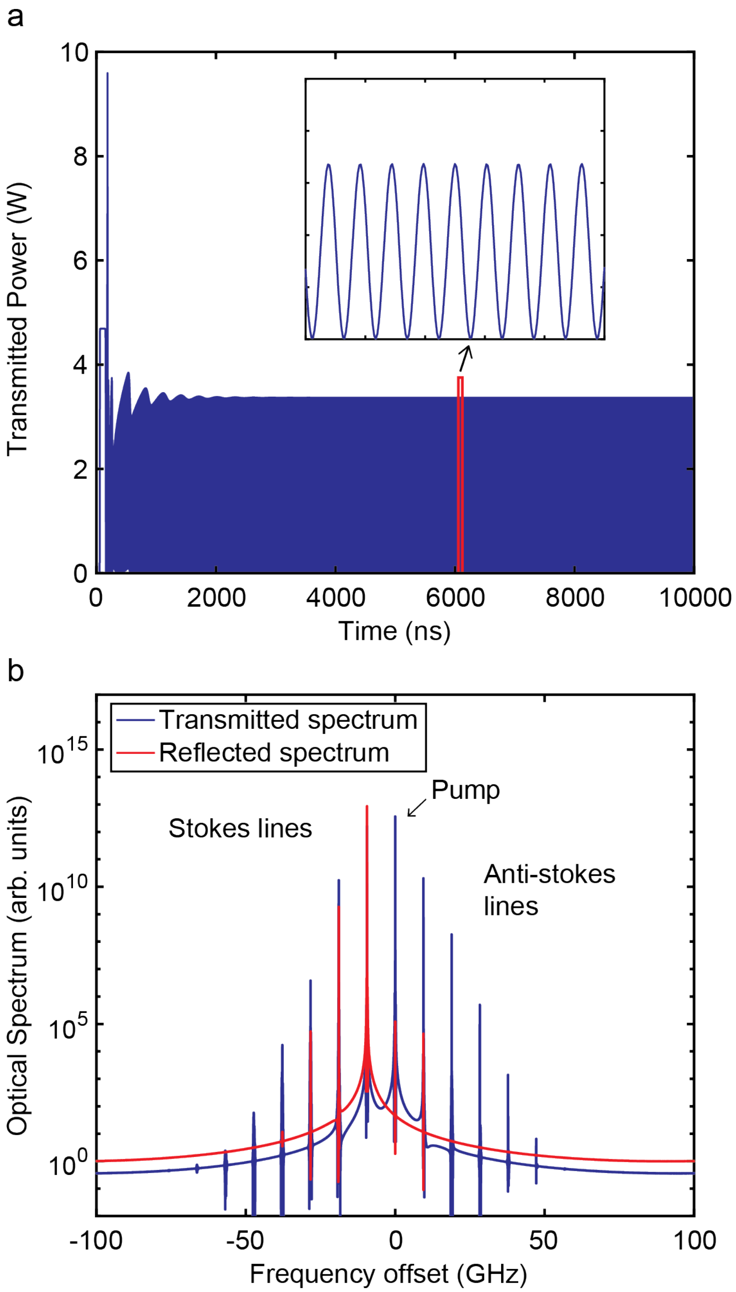

Figure 4.4: a) Temporal output and b) transmitted and reflected spectra from a fiber with a 20% Fresnel reflecting input facet and a 5-W cw pump. Many Stokes and anti-Stokes lines are now visible due to four-wave mixing.

which would already be extremely difficult to model properly with the old approach of separating every mode into its own variable. The basis of a frequency comb can be now be seen, with the dominant effects being cascaded SBS into FWM to generate the multiple modes [48].

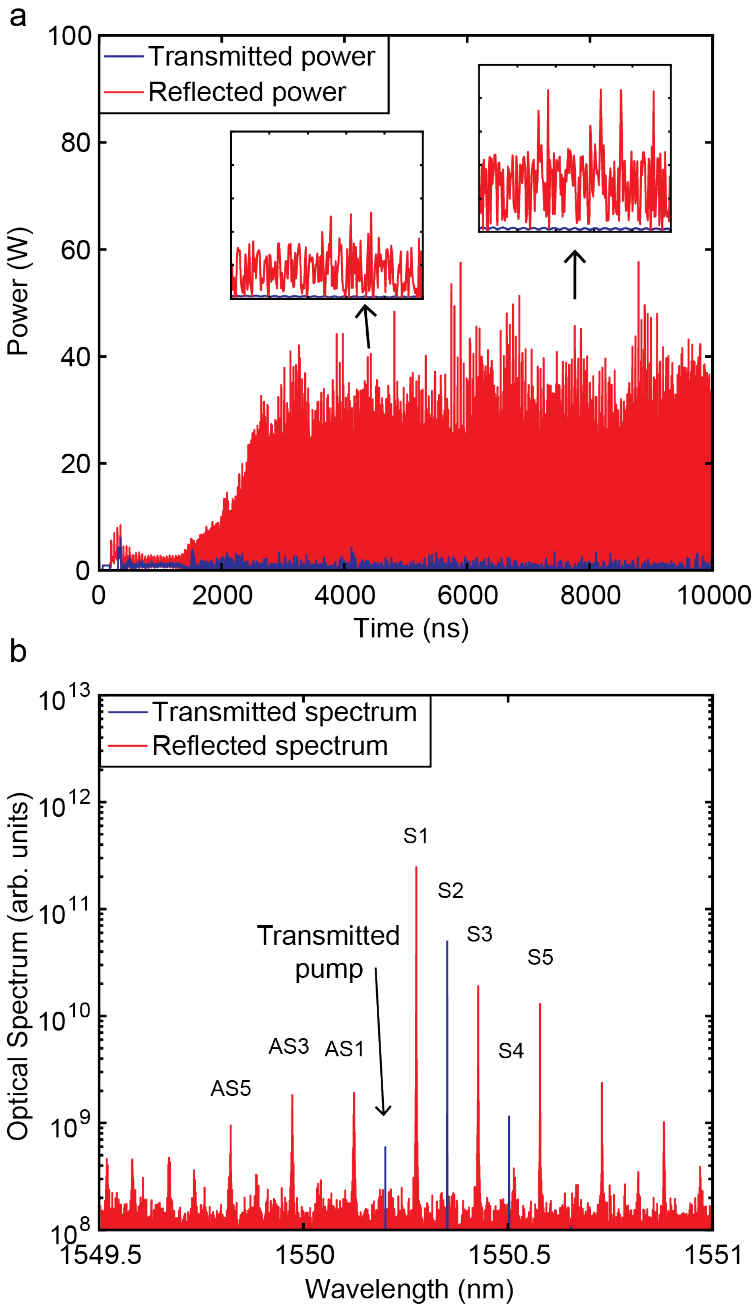

Figure 4.5: a) Output spectrum of a silica fiber ring cavity with feedback of 99% of the backward Stokes. The odd-order Stokes and anti-Stokes lines are spaced by twice the Brillouin frequency. b) Temporal output showing erratic pulsations.

Now we seek to reproduce some data from cascaded SBS frequency comb experiments. The first experiment we look at is by Tang, *et al.* [49]. The experiment uses 2.5 km of silica fiber pumped with 160 mW of power at 1546.5 nm in a ring cavity configuration. The backward Stokes waves are recirculated via fiber couplers, with 99% of the backward wave being fed back through the back facet. In terms of mathematical boundary conditions, this ring cavity is equivalent to

$$B(z = L, t) = 0.99 B(z = 0, t) \,. \tag{4.10}$$

Because simulating 2.5 km of fiber is rather time consuming, we shorten the fiber length to 10 m but greatly increase the pump power. We calculate the power output and spectra for an input pump of 1 W, shown in Figure 4.5. The spectra are in good agreement with the experimental results, with several odd numbered modes in the backward wave, meaning the frequency offset is $m\Omega_B$, where m is odd. The transmitted spectrum also exhibits some modes, although all at even ordered frequencies. The labels in Figure 4.5a correspond to Stokes (S) scattering or anti-Stokes (AS) modes with the frequency offset. The odd numbered modes emerge from the first two cascaded Stokes interactions, then mixing the strongest lines (S1 and S3) to create other odd numbered frequencies.

The temporal output also matches the experimental results with many seemingly random fluctuations. This chaotic behavior likely reflects the changing phases and amplitudes of the various modes interfering together, which suggests that there is no stable phase relation between them. If this is the case, the spectrum may look like a frequency comb but unless the phase is stabilized, the comb cannot be used.

The last experiment we investigate is by Büttner, *et al.* [36]. The experimental setup is in a chalcogenide glass fiber which has much higher nonlinear coefficients, including Brillouin gain, albeit at a cost of higher linear loss. The fiber is cut into a length of 38 cm which is resonant with the Brillouin frequency shift and acts as a Fabry-Perot cavity with facet reflections. A 500 ns square pulse of 0.7 W power is sent through the fiber and the outputs are monitored. Our new boundary conditions

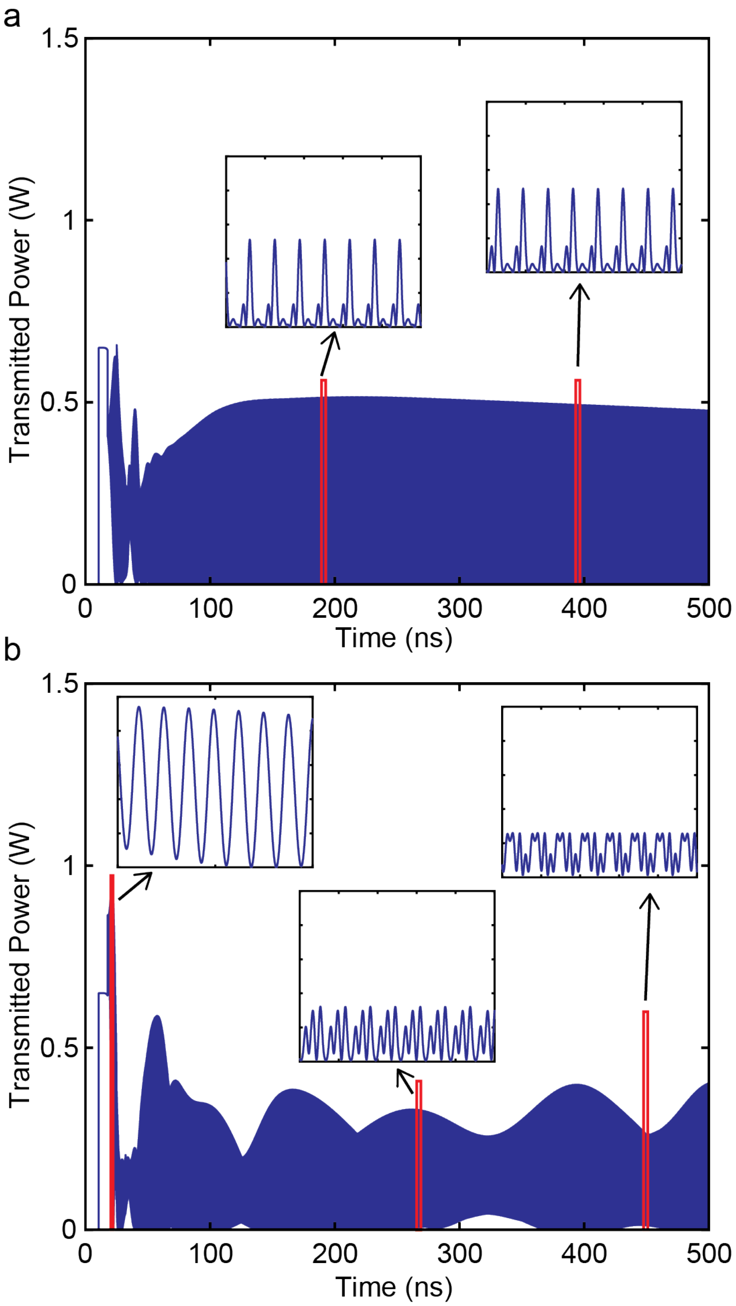

Figure 4.6: Temporal output of 38-cm-long chalcogenide fiber Fabry-Perot cavity for a 500-ns pulse input and two different values of phase shift. a) $\phi_0 = 0.62\pi$; b) $\phi_0 = 1.8\pi$

are

$$B(z = L, t) = -rA(z = L, t)e^{i\Delta\phi_0} \tag{4.11a}$$

$$A(z = 0, t) = -rB(z = L, t) + \sqrt{0.7}\,, \tag{4.11b}$$

where $|r|^2 = 0.226$ and $\Delta\phi_0$ is a constant phase factor. The origin of this phase factor stems from the fact that we have reflections from the front and the back facets and need to apply the proper carrier phase shift that has been neglected thus far. This phase shift is equal to

$$\Delta\phi_0 = 2k_0 L \,. \tag{4.12}$$

Because the value of k_0 is rather large, very slight adjustments to the carrier frequency ω_0 will easily be able to sweep this phase from 0 to 2π to yield different results, particularly in the phase relations between the modes.

We calculate the transmitted and reflected power through the fiber for 500 ns with the adjusted boundary conditions while sweeping the parameter $\Delta\phi_0$, as did the actual experiment. We plot the temporal outputs for two values of the phase, $\Delta\phi_0 = 0.62\pi$, and $\Delta\phi_0 = 1.8\pi$ that are in good agreement with the experimental data (Figure 4.6). In the case of $\Delta\phi_0 = 0.62\pi$, the modes appear to be well correlated and form a relatively stable series of pulses. However, in the case of $\Delta\phi_0 = 1.8\pi$, we find a more oscillatory solution that forms pulses and then breaks up and reforms in a periodic manner.

If we focus on the initial oscillations, a zoomed-in inset around 20 ns shows a rapidly oscillating sinusoid at the Brillouin frequency shift from the the beating between the pump and the newly generated first Stokes wave [50]. The temporal output becomes more complex as more SBS modes are generated, either coherently combining to form pulses or having slight differences between the frequency spacing, resulting in the long period oscillations in Figure 4.6b.

A typical spectrum is shown in Figure 4.7, which also is in good agreement with the experimental spectrum. We see quite a few strong Stokes modes adjacent to the pump but also the emergence of a few anti-Stokes modes from FWM, same as reported

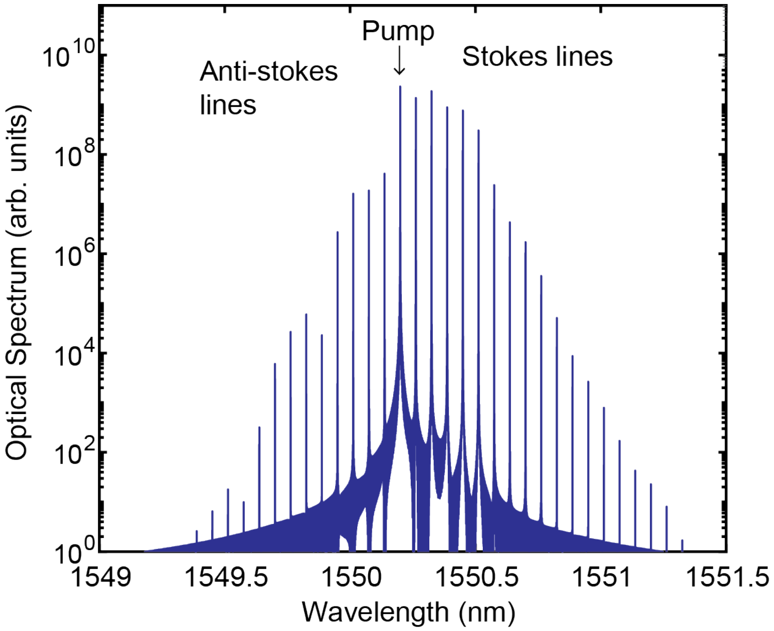

Figure 4.7: Typical spectrum of temporal outputs in Figure 4.6. There are several strong Stokes lines of the frequency comb with a few anti-Stokes lines adjacent to the pump.

in the experiment. By tweaking the carrier phase offset $\Delta\phi_0$, the chalcogenide fiber cavity is able to convert a CW pump into a series of pulses with a modest bandwidth via cascaded SBS and FWM.

4.4 Conclusion

To conclude this chapter, we have shown the power of formulating the traveling wave equations for multiple modes around a single carrier frequency. Instead of the conventional SBS approach in which each wave is a separate envelope, all waves are described by a single variable through phase and amplitude modulations. This essentially allows for modeling adjacent side modes, from SBS or an optical cavity, with greatly reduced number of interaction terms and variables, simplifying the equations to solve as well as producing a more predictive model without knowing *apriori* the modes that will be significant. These side bands oscillate at the free-spectral range rather than the carrier frequency and allows us to easily calculate the emergence of additional modes without taking tiny time steps. This method is well-suited for modeling frequency comb generation as we shall see.

CHAPTER V

Modeling Quantum Well Gain in Semiconductor Laser Diodes

Moving past Brillouin scattering, we turn to other methods of frequency comb generation. In the effort to make frequency combs practical outside the confines of the laboratory, we prefer comb sources that are small and portable, easy to operate, and inexpensive. The semiconductor laser diode certainly fits all these criteria and its prevalence in many kinds of laboratory equipment and consumer devices strengthens the argument for using diodes as a frequency comb source.

However, semiconductor lasers are not without problems when it comes to frequency comb generation. The typical approach to generating frequency combs is to use a mode-locked laser. A passively mode-locked laser diode usually has two sections: a forward-biased gain section and a reverse-biased saturable absorber section that leads to the formation of a periodic train of short pulses. The periodic train in time domain translates to a comb in the frequency domain. Unfortunately because of fast carrier dynamics in the semiconductor, there are nonlinear phase shifts inside the cavity [51], which essentially limits the pulse width. These phase shifts originate from carrier-induced refractive index shift, in which movement of carriers changes the real part of the gain, which in turn changes the imaginary part or refractive index via Kramers-Kronig relations.

There are some ways to get around this issue. There have been successful attempts at mode-locking using semiconductor saturable absorber mirrors (SESAMs) in external cavity configurations [52] to minimize the phase effects. We can also generate frequency combs without generating a series of short pulses by generating a frequency modulated (FM) output. In this case, the laser remains CW or quasi-CW while its phase is periodically swept in time, resulting in a comb in frequency domain. Experimentally, this type of laser has been demonstrated in laser diodes based on bulk material [53], quantum wells [54, 55], quantum dots and quantum dashes [56, 57, 58], and quantum cascade lasers (QC lasers) [59]. There are also a number of substantial theoretical studies on FM comb generation in quantum dot [60, 61] and quantum cascade systems [62, 63] that use a variety of traveling wave and third-order perturbation techniques, but not a lot of work on quantum well laser diodes.

For our work, we opted for the FM comb approach in quantum well based systems. A ridge waveguide is etched into the semiconductor itself for light confinement. For this device, there is no need for external cavity configurations, so we do not need any additional optical components, moving parts, or precise alignments for frequency comb generation. Instead, the laser diode itself outputs the frequency comb. The quantum well systems are also advantageous for their low cost, high gain, mature manufacturing technology, and wide availability of materials. In this chapter, we present our detailed model for a quantum well laser diode [64] and later study how the FM comb emerges.

5.1 Derivation of Bloch Equations

Before we get to modeling lasers, we take a look at the fundamentals of light-matter interaction, which ultimately result in the Bloch equations. There are actually two distinct sets of equations, the optical Bloch equations and the semiconductor Bloch equations (SBE). The optical Bloch equations are more typically used for atomic systems in which there is relatively little coupling between the atoms and electrons, while the SBEs incorporate in detail the lattice potentials and carrier-carrier interactions. Generally speaking, SBEs are much more complex and require a second quantization formulation [65]. We will focus primarily on the optical Bloch equations, neglecting most of the carrier-carrier coupling (but incorporating some phenomenologically) for simplicity and practicality in solving the traveling wave equations, although we will make mention of the SBEs occasionally.

We begin with the Hamiltonian for light-matter interaction, or matter interacting with an electric field. Under the dipole approximation, the Hamiltonian takes the form

$$\hat{\mathbf{H}} = \hat{\mathbf{H}}_0 - \hat{\mu} \cdot \overline{\mathbf{E}}(\overline{\mathbf{r}}, t)\,, \tag{5.1}$$

where $\hat{\mathbf{H}}_0$ is the unperturbed Hamiltonian, $\hat{\mu} = -q\hat{\mathbf{r}}$ is the dipole operator, and q is the elementary charge. Now assume that for a semiconductor there is an allowed carrier state in the valence band denoted by

$$\langle \hat{\mathbf{r}} |\, 1 \rangle = c_1 \tag{5.2}$$

and in the conduction band denoted by

$$\langle \hat{\mathbf{r}} |\, 2 \rangle = c_2 e^{-i\omega_0 t}\,, \tag{5.3}$$

where ω_0 is an arbitrary frequency offset, but it is typically highly conveniently to set $\hbar\omega_0$ to the band gap energy. This is also called the interaction representation in some texts [14]. The matrix elements of the Hamiltonian are calculated to be

$$
\begin{aligned}
H_{11} &= \left\langle 1 \middle| \hat{\mathbf{H}}_0 \middle| 1 \right\rangle - \langle 1 | \hat{\mu} \cdot \overline{\mathbf{E}}(\overline{\mathbf{r}}, t) | 1 \rangle = E_v \\
H_{12} &= \left\langle 1 \middle| \hat{\mathbf{H}}_0 \middle| 2 \right\rangle - \langle 1 | \hat{\mu} \cdot \overline{\mathbf{E}}(\overline{\mathbf{r}}, t) | 2 \rangle = d_{cv}^{*} e^{-i\omega_0 t} \left(E(z,t) e^{-i\omega_0 t} + E^{*}(z,t) e^{i\omega_0 t} \right) \\
H_{21} &= \left\langle 2 \middle| \hat{\mathbf{H}}_0 \middle| 1 \right\rangle - \langle 2 | \hat{\mu} \cdot \overline{\mathbf{E}}(\overline{\mathbf{r}}, t) | 1 \rangle = d_{cv} e^{i\omega_0 t} \left(E(z,t) e^{-i\omega_0 t} + E^{*}(z,t) e^{i\omega_0 t} \right) \\
H_{22} &= \left\langle 2 \middle| \hat{\mathbf{H}}_0 \middle| 2 \right\rangle - \langle 2 | \hat{\mu} \cdot \overline{\mathbf{E}}(\overline{\mathbf{r}}, t) | 2 \rangle = E_c - \hbar\omega_0 \,.
\end{aligned}
$$

Here, E_v is the valence band carrier energy, E_c is the conduction band carrier energy, and $d_{cv} = q \langle 2 | \hat{\mathbf{r}} | 1 \rangle$ is the dipole matrix element. We now take the rotating wave approximation (RWA) and only keep the electric field terms in which the exponents cancel. The Hamiltonian can be written in matrix form

$$
\hat{\mathbf{H}} = \begin{bmatrix} E_v & d_{cv}^{*} E^{*}(z,t) \\ d_{cv} E(z,t) & E_c - \hbar\omega_0 \end{bmatrix} . \tag{5.4}
$$

We note that we have ignored many other potentials, including the Coulomb interaction and carrier-carrier scattering.

Once we have the Hamiltonian in Equation 5.4, we can apply the density matrix formulation to calculate the time evolution of carrier populations in the valence and conduction bands, as well as the microscopic polarization. The density matrix approach allows us to add relaxation and scattering terms back into the calculation in ways that the Schrödinger amplitude approach does not. The equation of motion for the density matrix elements is

$$
i\hbar \frac{\partial \rho}{\partial t} = \left[\hat{\mathbf{H}}, \rho \right] \tag{5.5}
$$

$$
\begin{aligned}
i\hbar\frac{\partial}{\partial t}\begin{bmatrix}\rho_{11} & \rho_{12}\\ \rho_{21} & \rho_{22}\end{bmatrix} = &\begin{bmatrix}E_v & d_{cv}^*E^*(z,t)\\ d_{cv}E(z,t) & E_c-\hbar\omega_0\end{bmatrix}\begin{bmatrix}\rho_{11} & \rho_{12}\\ \rho_{21} & \rho_{22}\end{bmatrix}\\
&-\begin{bmatrix}\rho_{11} & \rho_{12}\\ \rho_{21} & \rho_{22}\end{bmatrix}\begin{bmatrix}E_v & d_{cv}^*E^*(z,t)\\ d_{cv}E(z,t) & E_c-\hbar\omega_0\end{bmatrix}.
\end{aligned}
\tag{5.6}
$$

We write down the two population equations and the equation for the microscopic polarization

$$
\frac{\partial\rho_{11}}{\partial t} = \frac{1}{i\hbar}\left[d_{cv}^*E^*(z,t)\rho_{21} - d_{cv}E(z,t)\rho_{12}\right] \tag{5.7a}
$$

$$
\frac{\partial\rho_{22}}{\partial t} = \frac{1}{i\hbar}\left[d_{cv}E(z,t)\rho_{12} - d_{cv}^*E^*(z,t)\rho_{21}\right] \tag{5.7b}
$$

$$
i\hbar\frac{\partial\rho_{21}}{\partial t} = (\Delta E_{cv} - \hbar\omega_0)\rho_{21} - d_{cv}E(z,t)(\rho_{22}-\rho_{11})\,. \tag{5.8}
$$

We identify ρ_{22} as the electron occupation probability and rewrite it as ρ^e. Similarly, we write $1-\rho_{11} = \rho^h$, the hole occupation probability. The microscopic polarization is also rewritten as $p(\overline{\mathbf{k}},t)$, where $\overline{\mathbf{k}}$ is the carrier momentum vector which is related to the carrier energy ΔE_{cv} via the semiconductor band structure. We also add in the relaxation terms, so that Equations 5.7, 5.8 now take on the form of the Bloch equations [65], approximately describing light interacting with a semiconductor

$$
\frac{\partial\rho^e(\overline{\mathbf{k}},t)}{\partial t} = -\frac{2}{\hbar}Im[d_{cv}^*E^*(z,t)p(\overline{\mathbf{k}},t)] + \frac{\partial\rho^e(\overline{\mathbf{k}},t)}{\partial t}|_{relax} \tag{5.9a}
$$

$$
\frac{\partial\rho^h(\overline{\mathbf{k}},t)}{\partial t} = -\frac{2}{\hbar}Im[d_{cv}^*E^*(z,t)p(\overline{\mathbf{k}},t)] + \frac{\partial\rho^h(\overline{\mathbf{k}},t)}{\partial t}|_{relax} \tag{5.9b}
$$

$$
\begin{aligned}
i\hbar\frac{\partial p(\overline{\mathbf{k}},t)}{\partial t} =&(\Delta E_{cv}(\overline{\mathbf{k}}) - \hbar\omega_0)p(\overline{\mathbf{k}},t)\\
&- d_{cv}E(z,t)(\rho^e(\overline{\mathbf{k}},t)+\rho^h(\overline{\mathbf{k}},t)-1) - i\hbar\frac{p(\overline{\mathbf{k}},t)}{T_2}\,.
\end{aligned}
\tag{5.10}
$$

5.2 Derivation of light-matter interaction in quantum wells

The Bloch equations can be tailored to modeling quantum well gain after a certain amount of approximations. The general approach is to find the macroscopic polarization by calculating individual microscopic polarizations and carrier occupation probabilities, summing them up, and inserting the result into the RHS of the traveling wave equation (Equation 2.10).

However, we need to quantify the $\Delta E_{cv}(\overline{\mathbf{k}})$ term in Equations 5.9 and 5.10. In the full treatment given in the SBEs, the energy dependence upon $\overline{\mathbf{k}}$, also called the band structure, is automatically calculated with all interacting potentials present. While this is very accurate, we typically do not have the capacity to calculate the band structure in this much detail in a traveling wave model. Instead, we use the common parabolic band approximation in which the conduction band and the heavy hole (hh) valence band can be written as quadratic functions [66]. This approximation is valid as long as the material has a direct bandgap, excited carriers behave mostly like free carriers, and the the light interacts mostly with carriers close to the $\overline{\mathbf{k}} = 0$ or Γ-point.

For a quantum well structure, electrons and holes are confined in one direction, usually labeled as the z axis. However, we note that, in the coordinates of our traveling wave, this confined direction must either be x or y as the direction the wave travels ($\pm z$ directions) is actually one of the unconfined directions relative to the geometry of the quantum well. To minimize this confusion, we use

$$\overline{\mathbf{k}}_t = \overline{\mathbf{k}}_y + \overline{\mathbf{k}}_z \,, \tag{5.11}$$

the momentum vector in the unconfined or ”transverse” directions of the quantum well (written in traveling wave coordinates), and

$$\overline{\mathbf{k}}_\perp = \overline{\mathbf{k}}_x \,, \tag{5.12}$$

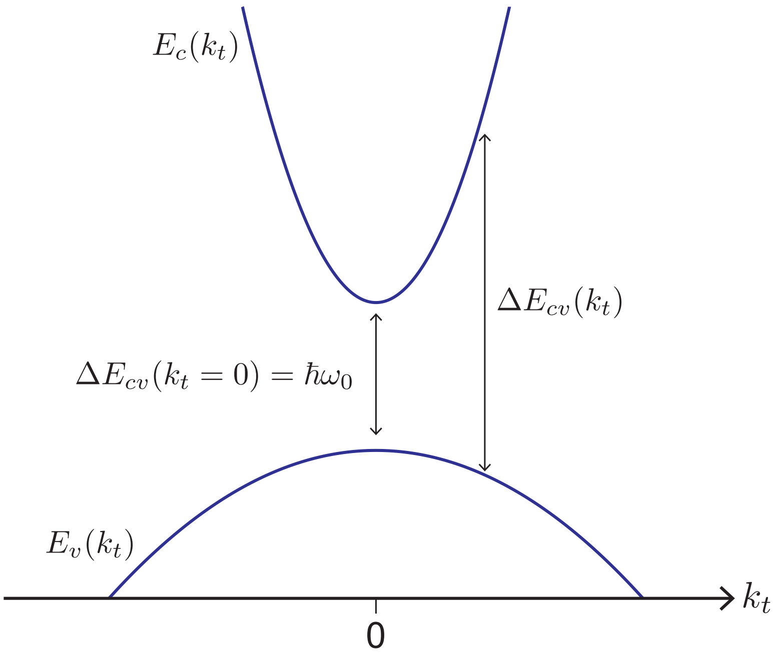

Figure 5.1: The parabolic band structure we use for our quantum well gain model. The energy difference ΔE_{cv}, which defines the radiative transition frequency or photon energy, is labeled and varies as the transverse momentum k_t varies.

in the carrier confined direction or perpendicular to the quantum well plane. We assume that only trapped or confined electrons will contribute to radiative recombinations. While the confined carrier energy is the same for all trapped carriers, the total energy of these carriers can vary significantly. Each confined carrier still has momentum and therefore energy in the $\overline{\mathbf{k}}_t$ directions, which contributes to inhomogeneous broadening of the gain spectrum.

The conduction and valence band energies in the parabolic approximation can be written in terms of the transverse momentum's magnitude $k_t = |\overline{\mathbf{k}}_t|$,

$$E_c(k_t) = E_g + E_{en} + \frac{\hbar^2 k_t^2}{2m_e^*} \tag{5.13}$$

$$E_v(k_t) = E_{hm} - \frac{\hbar^2 k_t^2}{2m_h^*}\,, \tag{5.14}$$

where E_g is the bandgap energy, E_{en} is the confinement energy of the nth confined electron state in the quantum well, E_{hm} is the confinement energy of the mth confined hole state, and $m^*_{e,h}$ is the electron and hole reduced effective mass. The transition energy, then, is simply the difference between these two energies

$$\Delta E_{cv}(k_t) = E_c - E_v$$

$$\Delta E_{cv}(k_t) = E^{en}_{hm} + \frac{\hbar^2 k_t^2}{2m_r^*}\,, \tag{5.15}$$

where $E^{en}_{hm} = E_g + E_{en} - E_{hm}$, and

$$m_r^* = \left[\frac{1}{m_e^*} + \frac{1}{m_h^*}\right]^{-1} \tag{5.16}$$

is the reduced effective mass. While a quantum well may have multiple confined states for the carriers, for simplicity our model only accounts for the first and lowest energy confined state. In this case, the $E^{en}_{hm} = E^{e1}_{h1}$. Figure 5.1 shows the parabolic band structure in the unconfined $\overline{\mathbf{k}}_t$ direction, labeling the variances in radiative recombination frequency. It is convenient now to define the variables

$$\hbar\omega_0 = E^{e1}_{h1} \tag{5.17}$$

$$E_t = \frac{\hbar^2 k_t^2}{2m_r^*}\,, \tag{5.18}$$

where the photon carrier frequency ω_0 that we extract from the traveling wave equations is now aligned to the fundamental quantum well transition. The new variable E_t is the transverse energy and represents the additional energy that is added due to carrier momentum in the unconfined directions.

Returning to the Bloch equations (Equations 5.9, 5.10), we can now make some progress in formulating our model. We insert the expression for the transition energy

(Equation 5.15) and rewrite the equations in terms of the transverse energy E_t. The microscopic polarization can be directly integrated to give

$$\int_{-\infty}^{t} dt' \left[\frac{\partial p(E_t, t')}{\partial t'} + i\frac{E_t}{\hbar} p(E_t, t') + \Gamma p(E_t, t') \right] = \frac{i}{\hbar} \int_{-\infty}^{t} dt' d_{cv} E(z, t') (\rho_{E_t}^{e} + \rho_{E_t}^{h} - 1)$$

$$\int_{-\infty}^{t} dt' \frac{\partial}{\partial t'} \left[p(E_t, t') e^{i\frac{E_t}{\hbar} t' + \Gamma t'} \right] = \frac{i}{\hbar} \int_{-\infty}^{t} dt' d_{cv} E(z, t') (\rho_{E_t}^{e} + \rho_{E_t}^{h} - 1) e^{i\frac{E_t}{\hbar} t' + \Gamma t'}$$

$$p(E_t, t) = \frac{i d_{cv}}{\hbar} \int_{-\infty}^{t} dt' E(z, t') (\rho_{E_t}^{e} + \rho_{E_t}^{h} - 1) e^{-i\frac{E_t}{\hbar}(t-t') - \Gamma(t-t')} \,. \tag{5.19}$$

We have rewritten the coherence relaxation time $T_2 = 1/\Gamma$, which is typically on the order of 10 - 100 fs (Zimmermann [67] measured a relaxation time of 300 fs for electrons and 50 fs for holes in strained quantum wells). We now make an important simplification by realizing that the population occupation probabilities will vary slowly in interband lasers, typically much slower than the coherence relaxation time. In this case, we can use the adiabatic approximation, in which the microscopic polarization adiabatically follows the electric field and population terms. Mathematically, if the $\rho_{E_t}^{e,h}$ terms in Equation 5.19 vary slowly relative to the exponential decay, then we can take them out of the integral. This results in a simple expression for the microscopic polarization

$$p(E_t, t) = \frac{i d_{cv}}{\hbar \Gamma} (\rho_{E_t}^{e} + \rho_{E_t}^{h} - 1) F(E_t, z, t) \,, \tag{5.20}$$

where we call $F(E_t, z, t)$ the filtered field [60] and is defined as

$$F(E_t, z, t) = \Gamma \int_{-\infty}^{t} dt' E(z, t') e^{-i\frac{E_t}{\hbar}(t-t') - \Gamma(t-t')} \,. \tag{5.21}$$

This filtered field variable is a time domain representation of a Lorentzian gain profile with half linewidth Γ centered around frequency $E_t/\hbar$. It captures the real and complex parts of the gain, dynamically accounting for carrier induced refractive index shifts.

To complete the derivation of the stimulated emission term, we insert the microscopic polarization (Equation 5.20) into the population equations (Equations 5.9) to obtain

$$\begin{aligned}\frac{\partial \rho^e_{E_t}}{\partial t} &= -\frac{2|d_{cv}|^2}{\hbar^2\Gamma} Im[iE^*(z,t)F(E_t,z,t)(\rho^e_{E_t}+\rho^h_{E_t}-1)] + \frac{\partial \rho^e_{E_t}}{\partial t}|_{relax} \\ \frac{\partial \rho^h_{E_t}}{\partial t} &= -\frac{2|d_{cv}|^2}{\hbar^2\Gamma} Im[iE^*(z,t)F(E_t,z,t)(\rho^e_{E_t}+\rho^h_{E_t}-1)] + \frac{\partial \rho^h_{E_t}}{\partial t}|_{relax}\end{aligned}$$

$$\frac{\partial \rho^e_{E_t}}{\partial t} = -\frac{2|d_{cv}|^2}{\hbar^2\Gamma}(\rho^e_{E_t}+\rho^h_{E_t}-1) Re[E^*(z,t)F(E_t,z,t)] + \frac{\partial \rho^e_{E_t}}{\partial t}|_{relax} \tag{5.22a}$$

$$\frac{\partial \rho^h_{E_t}}{\partial t} = -\frac{2|d_{cv}|^2}{\hbar^2\Gamma}(\rho^e_{E_t}+\rho^h_{E_t}-1) Re[E^*(z,t)F(E_t,z,t)] + \frac{\partial \rho^h_{E_t}}{\partial t}|_{relax}\,. \tag{5.22b}$$

As per usual, we rewrite several variables in more convenient units, starting with the electric field in units of $\sqrt{\mathrm{W}}$

$$E(z,t) \rightarrow \sqrt{\frac{2}{\epsilon_0 n_g c A_{eff}}} E(z,t)\,. \tag{5.23}$$

Operating with a transverse integral over the area of the quantum well, we next define the mode overlap integral

$$\Gamma_{xy} = \int\!\!\int dA \frac{F_{qw,xy}F_{xy}}{A_{eff}}\,, \tag{5.24}$$

where $F_{qw,xy}$ is the transverse distribution of electrons, roughly uniform over the active region. Thus when this integral operates on the LHS of Equations 5.22, it yields the active region area for a single quantum well which is approximately $A_{active} = h_{qw}W$, where h_{qw} is the height or thickness of the quantum well and W is the width of the optical waveguide. The overlap integral is typically on the order of 1% -10% depending on the design of the active region. Now the electric dipole moment can be rewritten in terms of the momentum matrix element [66]

$$|d_{cv}|^2 = \frac{q^2}{m_0^2 \omega_0^2} |\hat{\mathbf{e}} \cdot \overline{\mathbf{p}}|^2 \, , \tag{5.25}$$

where q is the electron charge and m_0 is the free electron mass. The momentum matrix element can be related to an experimental parameter E_P via

$$|\hat{\mathbf{e}} \cdot \overline{\mathbf{p}}|^2 \approx \frac{m_0 E_P}{6} \, . \tag{5.26}$$

The value of E_P varies by material but has been measured and documented for the most common III-V semiconductors. We also introduce the effective reduced or joint 2-D density of states

$$N_{r,qw} = \frac{\Delta E_t m_r^*}{\hbar^2 \pi h_{qw}} \, , \tag{5.27}$$

where ΔE_t is a discretized slice of the transverse energy. Writing the terms this way will give us some physical insight, as we will see in a moment. Putting it all together, the rate equations become

$$\frac{\partial \rho^e_{E_t}}{\partial t} = - 8 g_0 \frac{\Delta E_t}{(\hbar\omega_0)^2 h_{qw} W N_{r,qw}} (\rho^e_{E_t} + \rho^h_{E_t} - 1) Re(E^* F) + \frac{\partial \rho^e_{E_t}}{\partial t}|_{relax} \tag{5.28a}$$

$$\frac{\partial \rho^h_{E_t}}{\partial t} = - 8 g_0 \frac{\Delta E_t}{(\hbar\omega_0)^2 h_{qw} W N_{r,qw}} (\rho^e_{E_t} + \rho^h_{E_t} - 1) Re(E^* F) + \frac{\partial \rho^h_{E_t}}{\partial t}|_{relax} \, , \tag{5.28b}$$

with the gain coefficient

$$g_0 = \Gamma_{xy} \frac{q^2 E_P m_r^*}{12 \pi n_g c \epsilon_0 m_0 \hbar^2 \Gamma h_{qw}} \, . \tag{5.29}$$

In this form, we can describe the stimulated emission in physical terms. It is the number of photons per second (electric field power $Re(E^*F)$ divided by the photon energy $\hbar\omega_0$) resonant with carriers at transition energy E_t with width ΔE_t, divided by the total number of states available for that carrier group at E_t with the gain coefficient as the conversion factor. This results in a rate of carrier depletion with units $1/s$, which we can write as the stimulated emission rate

$$R_{st} = 8g_0 \frac{\Delta E_t}{(\hbar\omega_0)^2 h_{qw} W N_{r,qw}} \, . \tag{5.30}$$

The derivation of the stimulated emission term at this point is complete. Light interacts with a certain group of carriers in an energy bin with energy E_t and bin width ΔE_t. These carriers are tracked separately, each with their own rate equations and Lorentzian gain lineshapes. In order to properly model the inhomogeneous broadening, the overall gain will be the result of a summation of all of these carrier-photon interactions.

5.3 Modeling carrier injection and relaxation in quantum wells

While the light-matter interaction term has been carefully derived from the Bloch equations, the carrier injection and relaxation terms are added phenomenologically. We follow the schematic of the quantum well shown in Figure 5.2. There is a bulk layer called the separate confinement heterostructure (SCH) layer that facilitates electron transport and capture into the quantum well. We model the carrier occupation probability in this region via the variable $\rho_{sch}^{e,h}$ and we add a subscript to the quantum well carriers to avoid confusion $\rho_{qw,E_t}^{e,h}$. Electrons are captured into the quantum well (with lifetime τ_c), hence lost by the SCH, and simultaneously electrons can escape from the quantum well (with lifetime τ_e) and gained by the SCH. To begin quanti-

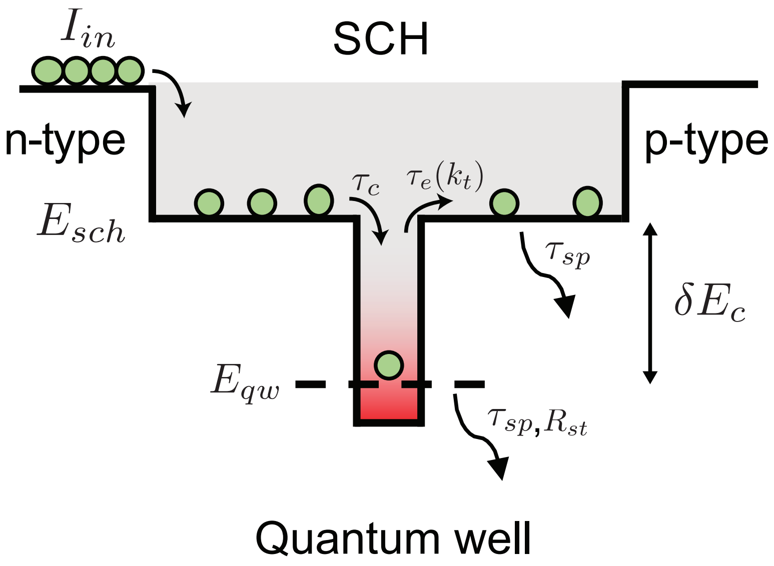

Figure 5.2: A schematic of carrier injection, capture, and escape in a quantum well laser diode. The lifetimes are measured

fying the term $\frac{\partial \rho^{e,h}_{qw,E_t}}{\partial t}|_{relax}$, we write simple rate equations for the SCH (N_{sch}) and quantum well (N_{qw}) carrier number that satisfy charge conservation

$$\frac{dN_{sch}}{dt} = -\frac{N_{sch}}{\tau_c} + \frac{N_{qw}}{\tau_e} \tag{5.31a}$$

$$\frac{dN_{qw}}{dt} = \frac{N_{sch}}{\tau_c} - \frac{N_{qw}}{\tau_e} \tag{5.31b}$$

$$\frac{d}{dt}(N_{sch} + N_{qw}) = 0\,. \tag{5.32}$$

The carrier number can be converted into carrier occupation probabilities via

$$N_{sch} = N_{c,v,sch} W h_{sch} \Delta z \rho^{e,h}_{sch} \tag{5.33a}$$

$$N_{qw} = N_{r,qw} W h_{qw} \Delta z \rho^{e,h}_{qw,E_t}\,, \tag{5.33b}$$

where

$$N_{c,v,sch} = 2\left(\frac{m^*_{e,h} k_B T}{2\hbar^2 \pi}\right)^{3/2} \tag{5.34}$$

is the effective bulk density of states for the conduction and valence bands. We now add Pauli blocking terms and obtain a set of coupled rate equations for the occupation probabilities

$$\frac{d\rho_{sch}}{dt} = -\frac{\rho^{e,h}_{sch}}{\tau^{e,h}_c}(1-\rho^{e,h}_{qw,E_t}) + \frac{N_{r,qw}h_{qw}}{N_{c,v,sch}h_{sch}}\frac{\rho^{e,h}_{qw,E_t}}{\tau^{e,h}_e}(1-\rho^{e,h}_{sch}) \tag{5.35a}$$

$$\frac{d\rho_{qw,E_t}}{dt} = \frac{N_{c,v,sch}h_{sch}}{N_{r,qw}h_{qw}}\frac{\rho^{e,h}_{sch}}{\tau^{e,h}_c}(1-\rho^{e,h}_{qw,E_t}) - \frac{\rho^{e,h}_{qw,E_t}}{\tau^{e,h}_e}(1-\rho^{e,h}_{sch})\,. \tag{5.35b}$$

We note that, for spin 1/2 carriers, the steady state solutions to Equations 5.35 should obey Fermi-Dirac statistics and relax into a Fermi-Dirac distribution. We assume the solutions for the electrons, with holes following a similar expression, are of the form:

$$\rho^e_{sch} = \frac{1}{1+\exp\left(\frac{E_{sch}-E_f}{k_B T}\right)} \tag{5.36a}$$

$$\rho^e_{qw,E_t} = \frac{1}{1+\exp\left(\frac{E_{qw}+\frac{m^*_r}{m^*_e}E_t-E_f}{k_B T}\right)}\,, \tag{5.36b}$$

where E_f is the electron Fermi level. Inserting these expressions into Equations 5.35, we can solve for the proper escape time in terms of the capture time such that the occupation probabilities settle into Fermi-Dirac statistics in steady state. We find the resulting expressions for the escape times and the relaxation to be:

$$\tau^e_e(E_t) = \tau^e_c\left(\frac{N_{r,qw}h_{qw}}{N_{c,sch}h_{sch}}\right)\exp((\delta E_c - \frac{m^*_r}{m^*_e}E_t)/k_B T) \tag{5.37a}$$

$$\tau^h_e(E_t) = \tau^h_c\left(\frac{N_{r,qw}h_{qw}}{N_{v,sch}h_{sch}}\right)\exp((\delta E_v - \frac{m^*_r}{m^*_h}E_t)/k_B T)\,. \tag{5.37b}$$

Here, $\delta E_c = E_{sch} - E_{qw}$ (and analogously, δE_v) is the energy difference between the SCH layer and the confined carrier with zero transverse energy, visually labeled in Figure 5.2. For a slightly simpler form, we relocate the bracketed fraction from the lifetimes and write it explicitly in the rate equations, allowing us to define the escape lifetimes as:

$$\tau_e^e(E_t) = \tau_c^e \exp((\delta E_c - \frac{m_r^*}{m_e^*} E_t)/k_B T) \tag{5.38a}$$

$$\tau_e^h(E_t) = \tau_c^h \exp((\delta E_v - \frac{m_r^*}{m_h^*} E_t)/k_B T) \tag{5.38b}$$

Finally, we can combine the capture and escape terms with the stimulated emission term and add in a spontaneous lifetime to get the rate equations. While we have shown the derivation for only a single quantum well carrier group, there are actually multiple quantum well rate equations discretized by the value of E_t with bin width ΔE_t. Thus the SCH equation must sum up the capture and escape contributions from every group of quantum well carriers. Taking this into account, we write the down the rate equations with carrier injection, capture, and escape.

$$\frac{\partial \rho_{sch}^{e,h}}{\partial t} = \frac{\eta J_{in}}{q N_{c,v,sch} h_{sch}} (1 - \rho_{sch}) - \frac{\rho_{sch}^{e,h}}{\tau_{sp}} + \sum_{E_t} \left[\frac{\rho_{qw,E_t}^{e,h}}{\tau_e^{e,h}} (1 - \rho_{sch}^{e,h}) - \frac{\rho_{sch}^{e,h}}{\tau_c^{e,h}} (1 - \rho_{qw,E_t}^{e,h}) \right] \tag{5.39a}$$

$$\frac{\partial \rho_{qw,E_t}^{e,h}}{\partial t} = \frac{N_{c,v,sch} h_{sch}}{N_{r,qw} h_{qw}} \left(\frac{\rho_{sch}^{e,h}}{\tau_c^{e,h}} (1 - \rho_{qw,E_t}^{e,h}) - \frac{\rho_{qw,E_t}^{e,h}}{\tau_e^{e,h}} (1 - \rho_{sch}^{e,h}) \right) - \frac{\rho_{qw,E_t}^{e,h}}{\tau_{sp}} - R_{st} \tag{5.39b}$$

We can account for multiple quantum wells by adding a simple parameter n_{qw} to denote the number of quantum wells and assume that carriers are injected uniformly across all quantum wells without coupling. In this case, the rate equations are modified to

$$\frac{\partial \rho^{e,h}_{sch}}{\partial t} = \frac{\eta J_{in}}{q N_{c,v,sch} h_{sch}}(1-\rho_{sch}) - \frac{\rho^{e,h}_{sch}}{\tau_{sp}} + n_{qw}\sum_{E_t}\left[\frac{\rho^{e,h}_{qw,E_t}}{\tau^{e,h}_e}(1-\rho^{e,h}_{sch}) - \frac{\rho^{e,h}_{sch}}{\tau^{e,h}_c}(1-\rho^{e,h}_{qw,E_t})\right] \tag{5.40a}$$

$$\frac{\partial \rho^{e,h}_{qw,E_t}}{\partial t} = \frac{N_{c,v,sch} h_{sch}}{n_{qw} N_{r,qw} h_{qw}}\left(\frac{\rho^{e,h}_{sch}}{\tau^{e,h}_c}(1-\rho^{e,h}_{qw,E_t}) - \frac{\rho^{e,h}_{qw,E_t}}{\tau^{e,h}_e}(1-\rho^{e,h}_{sch})\right) - \frac{\rho^{e,h}_{qw,E_t}}{\tau_{sp}} - R_{st} \tag{5.40b}$$

The input current density is J_{in}, scaled by the quantum efficiency η, and τ_{sp} is the spontaneous lifetime.

5.4 Evaluation of the macroscopic polarization and gain spectrum

With the rate equations in place, we can evaluate the macroscopic nonlinear polarization in the traveling wave equations. We sum up all microscopic polarization contributions (Equation 5.20) in $\overline{\mathbf{k}}_t$ and write the total polarization as

$$\begin{aligned} P_{NL} &= \frac{2}{V}\sum_{\overline{\mathbf{k}}} -d^*_{cv} p(\overline{\mathbf{k}}_t, t) e^{-i\omega_0 t} \\ &= -i e^{-i\omega_0 t}\frac{|d_{cv}|^2}{2\hbar\Gamma}\frac{2}{V}\sum_{\overline{\mathbf{k}}}(\rho^e_{qw,E_t} + \rho^h_{qw,E_t} - 1) F(E_t, z, t)\,. \end{aligned} \tag{5.41}$$

The summation can be converted into a transverse energy integral via the 2-D density of state. Inserting Equation 5.41 into the RHS of Equations 2.10 yields

$$\begin{aligned} &F_{xy}\frac{\partial E_+}{\partial z} + F_{xy}\frac{n_g}{c}\frac{\partial E_+}{\partial t} = \\ &\qquad \frac{\mu_0}{2ik_0} e^{i\omega_0 t - ik_0 z}\frac{\partial^2}{\partial t^2}\left[-i e^{-i\omega_0 t}\frac{|d_{cv}|^2}{2\hbar\Gamma}\int dE_t \frac{m^*_r}{\hbar^2 \pi h_{qw}}(\rho^e_{qw,E_t} + \rho^h_{qw,E_t} - 1) F(E_t, z, t)\right] \end{aligned} \tag{5.42a}$$

$$
\begin{aligned}
&-F_{xy}\frac{\partial E_-}{\partial z} + F_{xy}\frac{n_g}{c}\frac{\partial E_-}{\partial t} = \\
&\qquad \frac{\mu_0}{2ik_0}e^{i\omega_0 t + ik_0 z}\frac{\partial^2}{\partial t^2}\left[-ie^{-i\omega_0 t}\frac{|d_{cv}|^2}{2\hbar\Gamma}\int dE_t \frac{m_r^*}{\hbar^2 \pi h_{qw}}(\rho^e_{qw,E_t} + \rho^h_{qw,E_t} - 1)F(E_t, z, t)\right] .
\end{aligned}
\tag{5.42b}
$$

We again rewrite the dipole matrix elements into momentum matrix elements and apply the slowly varying amplitude approximation for the second order derivative of the polarization to simplify the RHS. We also expand the filtered field into forward and backward components recalling that $F(E_t, z, t)$ is proportional to $E(z, t)$

$$
F(E_t, z, t) = F_+(E_t, z, t)e^{ik_0 z} + F_-(E_t, z, t)e^{-ik_0 z} . \tag{5.43}
$$

Lastly, we apply a transverse integral to the traveling wave equations, yielding the confinement factor $n_{qw}\Gamma_{xy}$. By taking the phase-matched components, the traveling wave equations become

$$
\frac{\partial E_+}{\partial z} + \frac{n_g}{c}\frac{\partial E_+}{\partial t} = n_{qw}g_0 \int \frac{dE_t}{\hbar\omega_0}(\rho^e_{qw,E_t} + \rho^h_{qw,E_t} - 1)F_+(E_t, z, t) \tag{5.44a}
$$

$$
-\frac{\partial E_-}{\partial z} + \frac{n_g}{c}\frac{\partial E_-}{\partial t} = n_{qw}g_0 \int \frac{dE_t}{\hbar\omega_0}(\rho^e_{qw,E_t} + \rho^h_{qw,E_t} - 1)F_-(E_t, z, t) . \tag{5.44b}
$$

The gain spectrum is found by taking the Fourier transform of the RHS of Equations 5.44. We assume the carriers are in steady state so that the populations obey Fermi-Dirac statistics. In this case, the Fourier transform evaluates to

$$
\begin{aligned}
&\mathcal{F}\left[n_{qw}g_0 \int \frac{dE_t}{\hbar\omega_0}(\rho^e_{qw,E_t} + \rho^h_{qw,E_t} - 1)F_\pm(E_t, z, t)\right] \\
&\qquad = n_{qw}g_0 \int \frac{dE_t}{\hbar\omega_0}(\rho^e_{qw,E_t} + \rho^h_{qw,E_t} - 1)\frac{E_\pm(z, \omega)}{-i(\omega + E_t/\hbar) - \Gamma} ,
\end{aligned}
$$

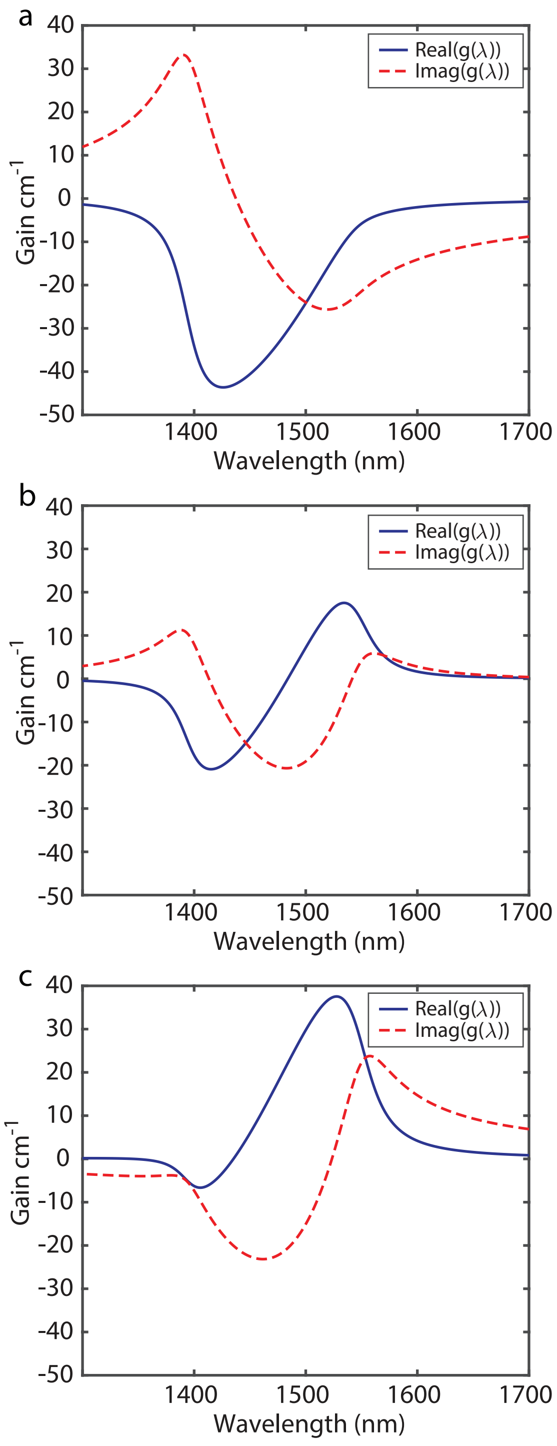

Figure 5.3: The real and imaginary parts of the gain plotted for various levels of carrier injection rates. a) low injection b) medium injection c) high injection. The gain is asymmetric, reflecting the product of the 2-D density of states and the Fermi-Dirac occupation probabilities.

and hence the gain spectrum is

$$g(\omega) = n_{qw} g_0 \int \frac{dE_t}{\hbar\omega_0} (\rho^e_{qw,E_t} + \rho^h_{qw,E_t} - 1) \frac{1}{-i(\omega + E_t/\hbar) - \Gamma} \tag{5.45}$$

In this form, we see that the gain spectrum is an integral of Lorentzians centered at different transition energies. A plot of Eq. 5.45 is shown in Figure 5.3 for varying levels of carrier population. Note that the gain is highly asymmetrical due to the quantum well 2-D density of states and the fact that lower energy carriers fill up much faster than higher energy carriers, a result of Fermi-Dirac statistics.

5.5 Complete equations for QW laser diode

We can at last put everything together - traveling waves coupled with the carrier rate equations. We add a few other effects to the electric field equations, including linear loss, second order dispersion, noise, and third order nonlinearities. The derivations of many of these effects can be found in standard textbooks [15], so we omit them here. We obtain the full set of equations to be

$$\begin{aligned}\frac{\partial E_+}{\partial z} + \frac{n_g}{c}\frac{\partial E_+}{\partial t} + i\frac{k''}{2}\frac{\partial^2 E_+}{\partial t^2} = -\frac{\alpha}{2}E_+ - (\frac{\alpha_S}{2} + i\beta_S)(|E_+|^2 + 2|E_-|^2)E_+ + S_{sp} \\ + n_{qw} g_0 \int \frac{dE_t}{\hbar\omega_0}(\rho^e_{qw,E_t} + \rho^h_{qw,E_t} - 1)F_+(E_t, z, t)\end{aligned} \tag{5.46a}$$

$$\begin{aligned}-\frac{\partial E_-}{\partial z} + \frac{n_g}{c}\frac{\partial E_-}{\partial t} + i\frac{k''}{2}\frac{\partial^2 E_-}{\partial t^2} = -\frac{\alpha}{2}E_- - (\frac{\alpha_S}{2} + i\beta_S)(|E_-|^2 + 2|E_+|^2)E_- + S_{sp} \\ + n_{qw} g_0 \int \frac{dE_t}{\hbar\omega_0}(\rho^e_{qw,E_t} + \rho^h_{qw,E_t} - 1)F_-(E_t, z, t)\,,\end{aligned} \tag{5.46b}$$

where k'' is the group velocity dispersion, α is the linear loss coefficient, α_S, β_S are the third order nonlinear coefficients for two-photon absorption and Kerr effect, respectively, and S_{sp} is the spontaneous emission noise. This spontaneous emission term S_{sp} is derived more phenomenologically and is related to the number of free carriers able to radiatively recombine. The traveling wave equations in Equations 5.46 are coupled to the rate equations given by

$$\frac{\partial \rho^{e,h}_{sch}}{\partial t} = \frac{\eta J_{in}}{q N_{c,v,sch} h_{sch}}(1-\rho_{sch}) - \frac{\rho^{e,h}_{sch}}{\tau_{sp}} + n_{qw}\sum_{E_t}\left[\frac{\rho^{e,h}_{qw,E_t}}{\tau^{e,h}_e}(1-\rho^{e,h}_{sch}) - \frac{\rho^{e,h}_{sch}}{\tau^{e,h}_c}(1-\rho^{e,h}_{qw,E_t})\right] \tag{5.47a}$$

$$\frac{\partial \rho^{e,h}_{qw,E_t}}{\partial t} = \frac{N_{c,v,sch} h_{sch}}{n_{qw} N_{r,qw} h_{qw}}\left(\frac{\rho^{e,h}_{sch}}{\tau^{e,h}_c}(1-\rho^{e,h}_{qw,E_t}) - \frac{\rho^{e,h}_{qw,E_t}}{\tau^{e,h}_e}(1-\rho^{e,h}_{sch})\right) - \frac{\rho^{e,h}_{qw,E_t}}{\tau_{sp}} - R_{st}\,. \tag{5.47b}$$

Equations 5.47 must be solved simultaneously with Equations 5.46 to calculate all carrier dynamics and laser dynamics in a quantum well laser diode. Typical values for all material parameters in these equations are given in Table 5.1.

The spontaneous emission term is found by following the approach in [61] in which the power spectrum follows the quantum well gain spectrum.

$$\begin{aligned} |S_{sp}\Delta z|^2 &= \sum_{modes} \frac{\#\text{ carriers}}{\tau_{sp}} \times \text{photon energy} \times \text{coupling factor} \\ &= \sum_{modes} n_{qw} \frac{N_{r,qw} h_{qw} W \Delta z}{2\pi \tau_{sp}} \rho^{e}_{qw,E_t} \rho^{h}_{qw,E_t} \hbar\omega\beta_{sp} \end{aligned}$$

$$S_{sp} \approx \sum_{E_t} \sqrt{\frac{n_{qw} N_{r,qw} h_{qw} W \beta_{sp} \hbar\omega \rho^{e}_{qw,E_t} \rho^{h}_{qw,E_t}}{2\pi\tau_{sp}\Delta z}} F_{sp}(E_t) \tag{5.48}$$

$$F_{sp}(E_t) = \Gamma \int_{-\infty}^{t} dt' e^{-i(\frac{E_t}{\hbar}-\omega_0)(t-t')-\Gamma(t-t')} e^{i\phi(z,t',E_t)} \tag{5.49}$$

Here, $\phi(z,t,E_t)$ is a random phase value between 0 and 2π, $\Delta z = c\Delta t/n_0$ is the spatial discretization size, and β_{sp} is the spontaneous emission coupling factor.

Parameter	Description	Value
L	Length of device	500 μm
W	Width of waveguide	4 μm
h_{sch}	Height of SCH layer	50 nm
h_{qw}	Height of quantum well	5 nm
n_g	Group refractive index	3.5
n_{qw}	Number of quantum wells	2
α	Intrinsic waveguide loss	5 cm^{-1}
Γ_{xy}	Optical confinement factor	0.01
α_S	Two-photon absorption	2750 W^{-1}m^{-1}
β_S	Kerr coefficient	430 W^{-1}m^{-1}
k''	Group velocity dispersion	1.25 ps^2/m
$\hbar\omega_0$	Central transition energy	800 meV
$\lvert\hat{\mathbf{e}} \cdot \overline{\mathbf{p}}\rvert^2$	Momentum matrix element	21 meV $\times m_0/6$ [66]
Γ	Homogenous half linewidth	10 meV/$\hbar$
$m^*_{e,h,sch}$	Effective mass of electrons, holes in the SCH layer	0.07m_0, 0.55m_0
$m^*_{e,h,qw}$	Effective mass of electrons, holes, in the InGaAsP QW	0.067m_0, 0.45m_0
$\tau_c^{e,h,qw}$	electron, hole capture time	1, 10 ps
δE_c	Conduction band quantum well barrier	50 meV
δE_v	Valence band quantum well barrier	75 meV
β_{sp}	Spontaneous emission coupling factor	1×10^{-4}
τ_{sp}	Spontaneous emission lifetime	1 ns

Table 5.1: Typical parameters for an InGaAsP quantum well with photoluminescence at 1.5 μm.

5.6 Numerical simulation of a quantum well semiconductor laser

Now we have all the pieces to numerically calculate the quantum well laser dynamics using parameters in Table 5.1. We numerically solve Equations 5.47, 5.46 using a simple first order Euler stepper along characteristics for both the carrier and electric field equations. We note that this is a step down from the SBS solution methods (fourth order collocation and fifth order predictor-corrector) which were much higher order, as the equations we solve here are extremely complex. Derivative evaluations are expensive here, so we opted for the time saving Euler's method. For future work, it is possible to implement a higher order scheme.

In order to solve all the discretized quantum well population equations, we specify a few more values. We define a maximum transverse energy $max(E_t) = 50$ meV, roughly corresponding to the quantum well electron barrier height. The idea is to include enough carrier groups until they become insignificant to the gain or until they can no longer be confined in the quantum well. For the energy spacing, we choose $\Delta E_t = 2$meV, which is small relative to the homogeneous linewidth 2Γ - this allows multiple Lorentzians to overlap in calculating the inhomogeneous gain. All calculations are done at room temperature $T = 300$K.

For our first study, we simulate an InGaAsP quantum well laser as a semiconductor optical amplifier operating at 1.5 μm to make sure the expected carrier dynamics are properly calculated. In this case, we pump the laser diode with $\eta I_{in} = 10$ mA with no reflections at the boundaries. Then, once the carriers are pumped, we send in a pulse to be amplified. Two pulses of similar total energies are sent through the amplifier, one with pulse width 5 ps and the other 0.5 ps. The amplified pulse magnitude and phase are plotted in Figure 5.4

We note that, as expected from past experiments [51], the length of the input pulse has large effects on the carrier dynamics and can induce unwanted phase effects in the amplified pulse. The short pulse has a cubic phase which stems from partial gain recovery from carrier cooling, which in our model involves carriers quickly refilling from the SCH layer. The capture time is 1 ps, so only pulses shorter than this time will appreciably see this effect. For the case of the long pulse, the process is much more adiabatic and the carrier population simply follows the shape of the pulse giving a simpler quadratic phase that is easy to compensate. The population levels in the laser cavity as these two pulses pass through is shown in Figure 5.5. As we discussed before, the short pulse population has much a steeper depletion and partial recovery,

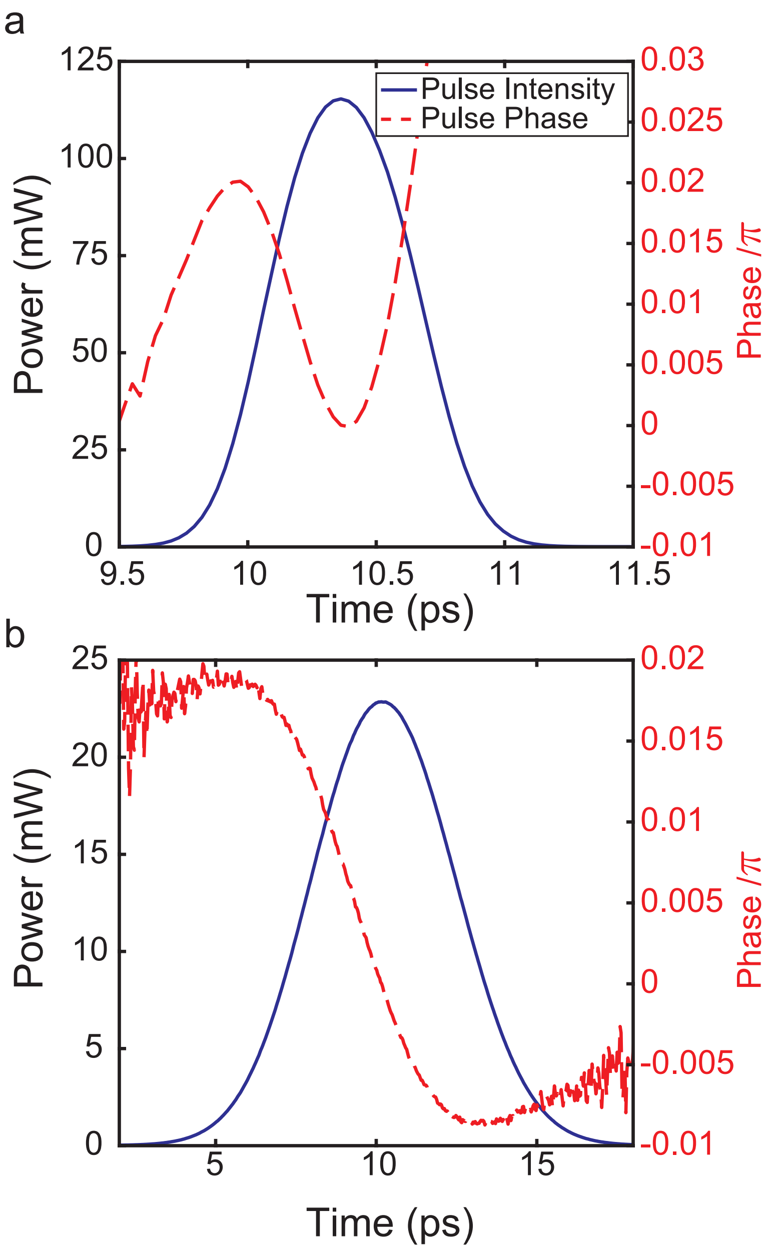

Figure 5.4: The results of sending in a transform limited or unchirped Gaussian pulse through a single pass of the laser cavity. The amplified pulse shape and phase are plotted for a) a 0.5 ps pulse b) a 5 ps pulse.

while the long pulse decreases mostly adiabatically. It is precisely these phase effects, resulting from fast carrier dynamics, that have made mode-locking in laser diodes difficult in the past. Our simulation is able to accurately reproduce these effects, so we can be confident of the robustness of any predicted mode-locking from our model.

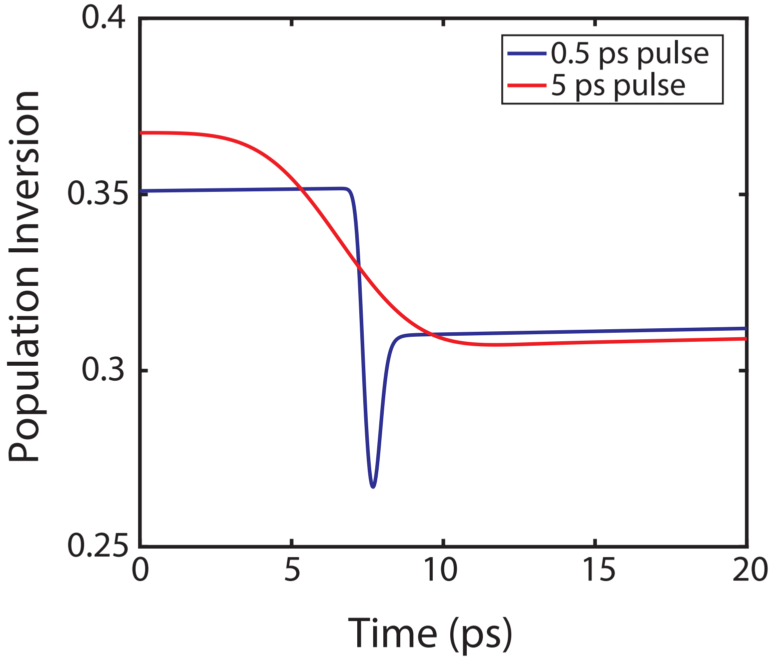

Figure 5.5: The population depletion and recovery as the pulses pass through.

Moving on from semiconductor optical amplifiers, we now run a numerical study on a ridge waveguide laser diode with an InGaAsP quantum well with a central photoluminescence (PL) wavelength of 1.5μm. The laser cavity is a simple Fabry-Perot cavity with facet reflecting mirrors, with reflection coefficient $|r|^2 = 0.32$. This time, there are no external input fields but the laser is started from noise with an DC injection current of $\eta I_{in} = 25$ mA. The temporal output and spectrum are plotted in Figure 5.6. The resulting spectrum has important physical characteristics - it is a single mode with CW temporal output after initial relaxation oscillations.

The nature of single mode operation can be understood in terms of gain competition [68]. In semiconductor lasers and certain gas lasers, the homogeneous linewidth $2\Gamma \approx 5$ THz is much larger than the cavity mode spacing ($\nu_{fsr} \approx 50$) GHz, meaning all cavity modes are competing for the same gain to lase. For such strong gain competition, only a single mode will emerge in steady state as once this mode reaches threshold, the gain is capped at threshold gain due to carrier depletion from stimulated emission. In Figure 5.7 the carrier dynamics are shown. Initially, the carriers

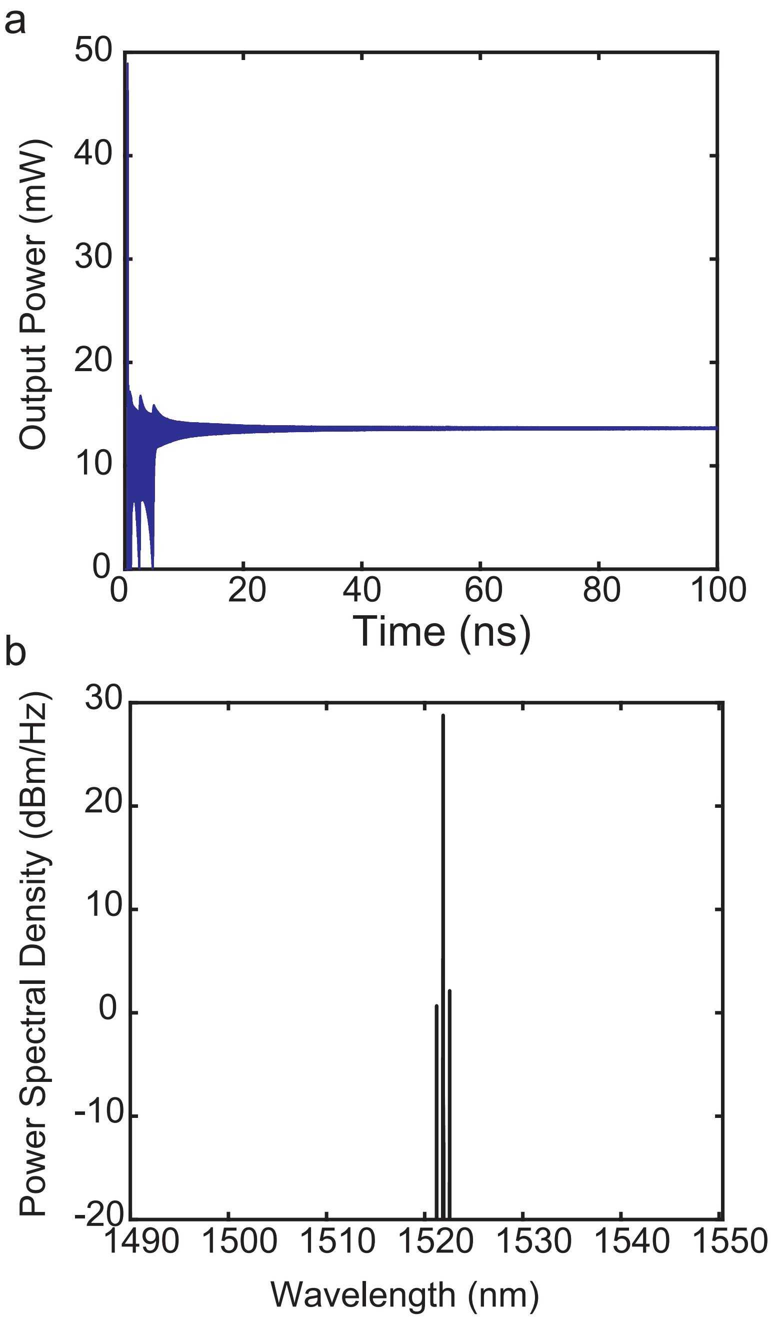

Figure 5.6: a) the temporal output of the InGaAsP quantum well laser.The output operates in a single mode after some initial relaxation oscillations b) the spectrum of the above output which shows predominantly a single mode, with some side bands many decades below the peak mode.

fill up very quickly, but within 1 ns the laser reaches threshold the populations start to deplete. We note that the electrons in the SCH and quantum well layer deplete to a lower level, but the holes actually continue to fill until they reach a steady state

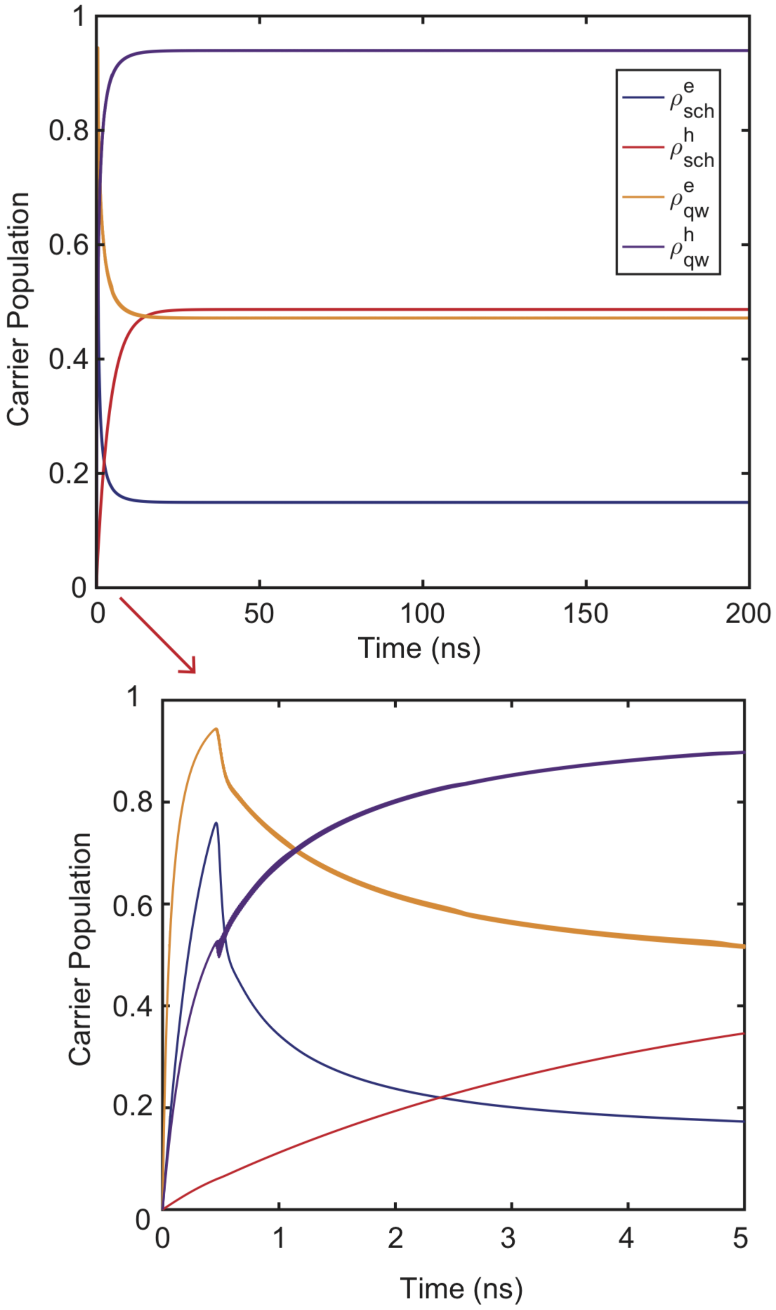

Figure 5.7: Plot of the temporal dynamics of the carriers in the SCH and QW regions. The populations settle into a steady state value after the initial pumping and then depletion from lasing.

value that is much larger than that of electrons. This interesting feature is due to the unusual splitting of the conduction and valence band offsets [69] in InGaAsP / InP heterojunctions. Of the total bandgap difference between InGaAsP and InP, ap-

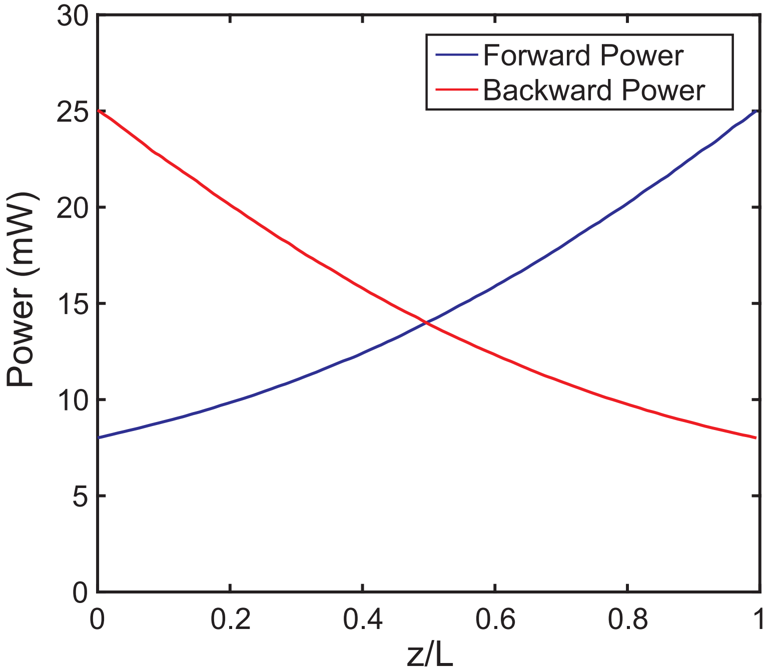

Figure 5.8: The forward and backward optical power inside the cavity in steady state. Such behavior is typical for a single mode laser.

proximately 40% is in the conduction band offset, while 60% is in the valence band. This means that holes have a much larger barrier height to overcome, meaning they are trapped much more efficiently than electrons and hence the charge build-up seen in Figure 5.7. This is in contrast to GaAs / AlGaAs heterojunctions in which the conduction band sees 2/3 of the bandgap difference while the valence band only sees 1/3 [70].

5.7 Conclusion

To conclude, we have successfully derived a model for quantum well laser diodes that incorporates inhomogeneous broadening, carrier induced refractive index shift, third order nonlinearities, second order dispersion, and fast carrier dynamics. The carrier dynamics of each inhomogeneous group is solved separately, all coupled through the interaction with carriers in the bulk SCH layer. Each of the carrier groups contributes a complex Lorentzian gain lineshape that accounts for refractive index shifts, and the total gain is calculated by integrating all of these carriers weighted by the 2D density of states. The model accurately replicates pulse amplification and calculates a quantum well laser with a single mode. However, the output is not yet a comb, and we take a look at how to generate one in the next chapter.

CHAPTER VI

Spatial Hole Burning and Frequency Comb Generation in Quantum Wells

While we have successfully derived and implemented a model for quantum well laser diodes, we find that the output of the laser is not actually a frequency comb, whether an FM comb or a mode-locked laser. Because there is no saturable absorber in our model (our laser is single-section), the single mode laser we found is expected as there is nothing driving mode-locking. However, there are additional physical effects such as spatial hole burning (SHB) which we did not yet include. As we shall see, the inclusion of standing waves inside the cavity, which generate carrier gratings or SHB, is vitally important to comb generation.

6.1 Modeling spatial hole burning in quantum well laser diodes

SHB occurs when there is a significant standing wave inside the laser cavity. When the forward and backward waves interfere, an intensity pattern is created with half the optical wavelength inside the cavity. This standing wave pattern has intensity peaks and minima, which in turn affects the rate of stimulated emission (as seen in R_{st}, Equation 5.30). This allows some parts of the cavity to see no electric field, retaining the carriers and gain in those sections. This unused gain can then be utilized by other,

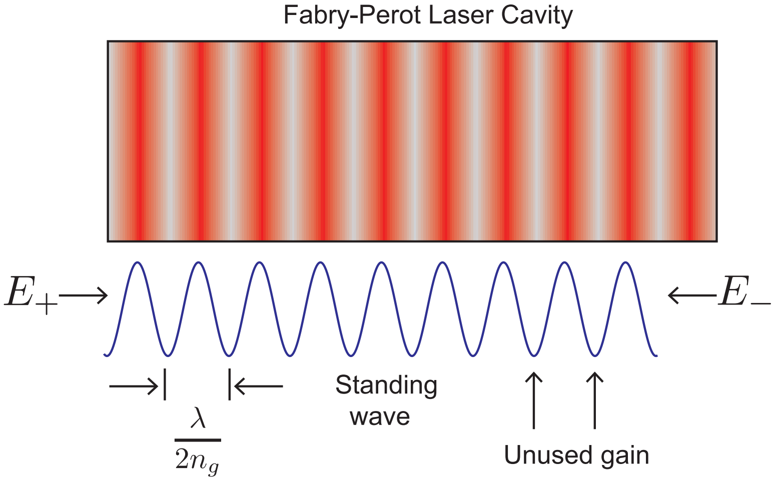

Figure 6.1: A diagram of SHB inside a Fabry-Perot cavity. The forward and backward waves create a standing wave pattern which does not deplete the gain uniformly inside the cavity.

adjacent cavity modes to reach threshold and lase simultaneously to the central mode. This multimode operation of the laser diode is vital to the generation of frequency combs. A schematic of SHB is shown in Figure 6.1.

However, we do have to be careful that carrier diffusion in our gain medium does not wash out the standing wave grating. In other words, the diffusion of carriers from the low intensity parts of the standing wave to the high intensity parts, and then recombining will still deplete carriers and gain at the intensity minima. Therefore, strong carrier diffusion and short operating wavelengths mitigate the effects of the unused gain. In this chapter, we focus on the InGaAsP quantum well operating at 1.5 μm wavelength, which has a strong enough SHB effect for multimode lasing. A more in-depth analysis of SHB in various quantum well systems is investigated in Chapter VII.

To model SHB, we look at several other quantum well models in the literature that have varying degree of complexity. They range from simple rate equations [71, 72] to more complicated models with multiple rate equations [73, 74, 75, 76, 77, 78, 79]. In particular, SHB modeling in papers such as [71, 80, 81] use an explicit grating equation, while other papers use a more phenomenological approach with adjustable parameters such as gain compression [61, 60, 82]. Because we need to carefully incorporate the diffusion effects into our system, we choose to use the more rigorous process of expanding the carrier populations in space and keeping the diffusion term to account for spatial gratings. This allows us to modify our current quantum well gain theory and also incorporating diffusion effects.

We add the effects of SHB to our current theory as follows. We start by modifying Equation 5.47b to include a diffusion term in the quantum well rate equations

$$\begin{aligned}\frac{\partial \rho^{e,h}_{qw,E_t}}{\partial t} = \frac{N_{c,v,sch} h_{sch}}{n_{qw} N_{r,qw} h_{qw}} &\left(\frac{\rho^{e,h}_{sch}}{\tau^{e,h}_c} (1 - \rho^{e,h}_{qw,E_t}) - \frac{\rho^{e,h}_{qw,E_t}}{\tau^{e,h}_e} (1 - \rho^{e,h}_{sch}) \right) \\ &- \frac{\rho^{e,h}_{qw,E_t}}{\tau_{sp}} - R_{st} - D \frac{\partial^2 \rho^{e,h}}{\partial z^2} \, ,\end{aligned} \tag{6.1}$$

where D is the ambipolar diffusion coefficient in units of cm^2/s. If we were to numerically calculate this term directly, we would need a spatial discretization of much less than a wavelength which is something we want to avoid. We can get around this by defining a separate variable for the grating terms by expanding the quantum well population to the first even harmonic in z

$$\rho^{e,h}_{qw,E_t} \to \rho^{e,h}_{qw,E_t} + \rho_{g,E_t} e^{i2k_0 z} + \rho^*_{g,E_t} e^{-i2k_0 z} \, , \tag{6.2}$$

where $k_0 = n_g \omega_0 / c$. In this expansion, we have made a few simplifying assumptions: we drop all higher order grating terms and we write only a single grating equation for both electrons and holes. The source for the grating is evaluated from the stimulated emission term in the rate equations, which contains the product:

$$\mathrm{Re}(E^* F) = \mathrm{Re}(E^*_+ F_+ + E^*_- F_-) + \frac{1}{2}(E^*_+ F_- + F^*_+ E_-) e^{i2k_0 z} + \frac{1}{2}(E_+ F^*_- + F_+ E^*_-) e^{-i2k_0 z}$$

Under this formulation, we can separate the quantum well rate equation into two equations, one for the carrier population and one for the grating, by matching the spatial phases on the LHS to the RHS of Equation 6.1

$$\frac{\partial \rho^{e,h}_{qw,E_t}}{\partial t} = ... - 8g_0 \frac{\Delta E_t}{(\hbar\omega_0)^2 h_{qw} W N_{r,qw}} \times \Big[\mathrm{Re}(E_+^* F_+ + E_-^* F_-)(\rho^e_{qw,E_t} + \rho^h_{qw,E_t} - 1) + (E_+ F_-^* + F_+ E_-^*)\rho_{g,E_t} + (E_+^* F_- + F_+^* E_-)\rho^*_{g,E_t} \Big] \tag{6.3}$$

$$\frac{\partial \rho_{g,E_t}}{\partial t} = -4k_0^2 D \rho_{g,E_t} - 8g_0 \frac{\Delta E_t}{(\hbar\omega_0)^2 h_{qw} W N_{r,qw}} \times \left[\frac{1}{2}(E_+^* F_- + F_+^* E_-)(\rho^e_{qw,E_t} + \rho^h_{qw,E_t} - 1) + 2\mathrm{Re}(E_+^* F_+ + E_-^* F_-)\rho_{g,E_t} \right] . \tag{6.4}$$

We define another rate constant as the photon-grating interaction

$$R_g = 8g_0 \frac{\Delta E_t}{(\hbar\omega_0)^2 h_{qw} W N_{r,qw}} \big((E_+ F_-^* + F_+ E_-^*)\rho_{g,E_t} + (E_+^* F_- + F_+^* E_-)\rho^*_{g,E_t} \big) . \tag{6.5}$$

Combining the new terms in the population and grating equations together, we obtain

$$\frac{\partial \rho^{e,h}_{sch}}{\partial t} = \frac{\eta J_{in}}{q N_{c,v,sch} h_{sch}}(1 - \rho^{e,h}_{sch}) - \frac{\rho^{e,h}_{sch}}{\tau_{sp}} + n_{qw} \sum_{E_t} \left[\rho^{e,h}_{qw,E_t} \frac{(1 - \rho^{e,h}_{sch})}{\tau^{e,h}_e} - \rho^{e,h}_{sch} \frac{(1 - \rho^{e,h}_{qw,E_t})}{\tau^{e,h}_c} \right] \tag{6.6a}$$

$$\frac{\partial \rho^{e,h}_{qw,E_t}}{\partial t} = \frac{h_{sch} N_{c,v,sch}}{n_{qw} h_{qw} N_{r,qw}} \left(\rho^{e,h}_{sch} \frac{(1 - \rho^{e,h}_{qw,E_t})}{\tau^{e,h}_c} - \rho^{e,h}_{qw,E_t} \frac{(1 - \rho^{e,h}_{sch})}{\tau^{e,h}_e} \right) - \frac{\rho^{e,h}_{qw,E_t}}{\tau_{sp}} - R_{st} - R_g \tag{6.6b}$$

$$\begin{aligned}\frac{\partial \rho_{g,E_t}}{\partial t} &= -\frac{\rho_{g,E_t}}{\tau_{sp}} - 4k_0^2 D\rho_{g,E_t} - 8g_0\frac{\Delta E_t}{(\hbar\omega_0)^2 h_{qw} W N_{r,qw}} \\ &\quad \times \left[\frac{1}{2}(E_+^* F_- + F_+^* E_-)(\rho_{qw}^e + \rho_{qw}^h - 1) + 2\mathrm{Re}(E_+^* F_+ + E_-^* F_-)\rho_{g,E_t}\right] .\end{aligned} \tag{6.6c}$$

For modifications to the traveling wave equations, we similarly phase match the RHS to the LHS of Equations 5.46 to obtain a coupling between the forward and backward waves through the carrier grating term

$$\begin{aligned}\frac{\partial E_+}{\partial z} + \frac{n_g}{c}\frac{\partial E_+}{\partial t} + i\frac{k''}{2}\frac{\partial^2 E_+}{\partial t^2} &= -\frac{\alpha}{2}E_+ - (\frac{\alpha_S}{2} + i\beta_S)(|E_+|^2 + 2|E_-|^2)E_+ + S_{sp} \\ &\quad + n_{qw} g_0 \int \frac{dE_t}{\hbar\omega_0}(\rho_{qw,E_t}^e + \rho_{qw,E_t}^h - 1)F_+(E_t, z, t) \\ &\quad + n_{qw} g_0 \int \frac{dE_t}{\hbar\omega_0}\rho_{g,E_t} F_-(E_t, z, t)\end{aligned} \tag{6.7a}$$

$$\begin{aligned}-\frac{\partial E_-}{\partial z} + \frac{n_g}{c}\frac{\partial E_-}{\partial t} + i\frac{k''}{2}\frac{\partial^2 E_-}{\partial t^2} &= -\frac{\alpha}{2}E_- - (\frac{\alpha_S}{2} + i\beta_S)(|E_-|^2 + 2|E_+|^2)E_- + S_{sp} \\ &\quad + n_{qw} g_0 \int \frac{dE_t}{\hbar\omega_0}(\rho_{qw,E_t}^e + \rho_{qw,E_t}^h - 1)F_-(E_t, z, t) \\ &\quad + n_{qw} g_0 \int \frac{dE_t}{\hbar\omega_0}\rho_{g,E_t}^* F_+(E_t, z, t) .\end{aligned} \tag{6.7b}$$

Equations 6.7 coupled with the rate equations 6.6 form the basis of our model with SHB included. These equations are significantly more complex than the model presented in Chapter V, as they introduce an additional grating equation for every carrier energy bin. However, the numerical methods used to solve the previous model still apply to solving these equations.

6.2 Calculating frequency modulated comb generation

We simulate the laser cavity once more with the effect of SHB. The parameters are the same as those in Table 5.1 with the addition of $D = 7.2\,\mathrm{cm}^2/\mathrm{s}$, a measured value in InGaAsP quantum wells [83].

We calculate the same Fabry-Perot laser as before, starting from noise, and monitor the output. The results are plotted in Figure 6.2. The power output and spectrum qualitatively replicate the experimental results for a single-section laser diode found in experiments [55, 54], with a significant number of strong comb lines spanning about 30 nm in bandwidth (or about 3 THz) with a mode spacing of $\nu_{fsr} = 85.7$ GHz. The laser reaches steady state at about $t = 100$ ns, before which there are irregular oscillations in the power output. After steady state, however, the waveform remains periodic and is coherent over a long timespan. We note that the output also does not consist of a train of short pulses as is typical for a mode-locked laser, but rather a periodic modulation of the intensity and phase to generate the comb spectrum. Plots of the output power and instantaneous frequency in Figure 6.2a,c show the periodic nature of the amplitude and phase, with both of them being swept in time. The instantaneous frequency is being swept across a large range of about 5 THz and has a triangular, almost saw-tooth like shape. The chirp of the laser output is linearly decreasing until it jumps back up and then repeats at the round trip cavity time. This frequency sweep is the signature feature of an FM signal.

The results in Figure 6.2 are in stark contrast to Figure 5.6. The carrier grating which induces the SHB effect is a major mechanism for the generation of multiple Fabry-Perot modes. This is consistent with previous work [61, 60] which modeled SHB in quantum dot laser diodes. Without an effect like SHB which reduces the gain competition between modes, we would only get a single mode laser, but now we are able to achieve multimode lasing without the need of active modulation or saturable absorbers.

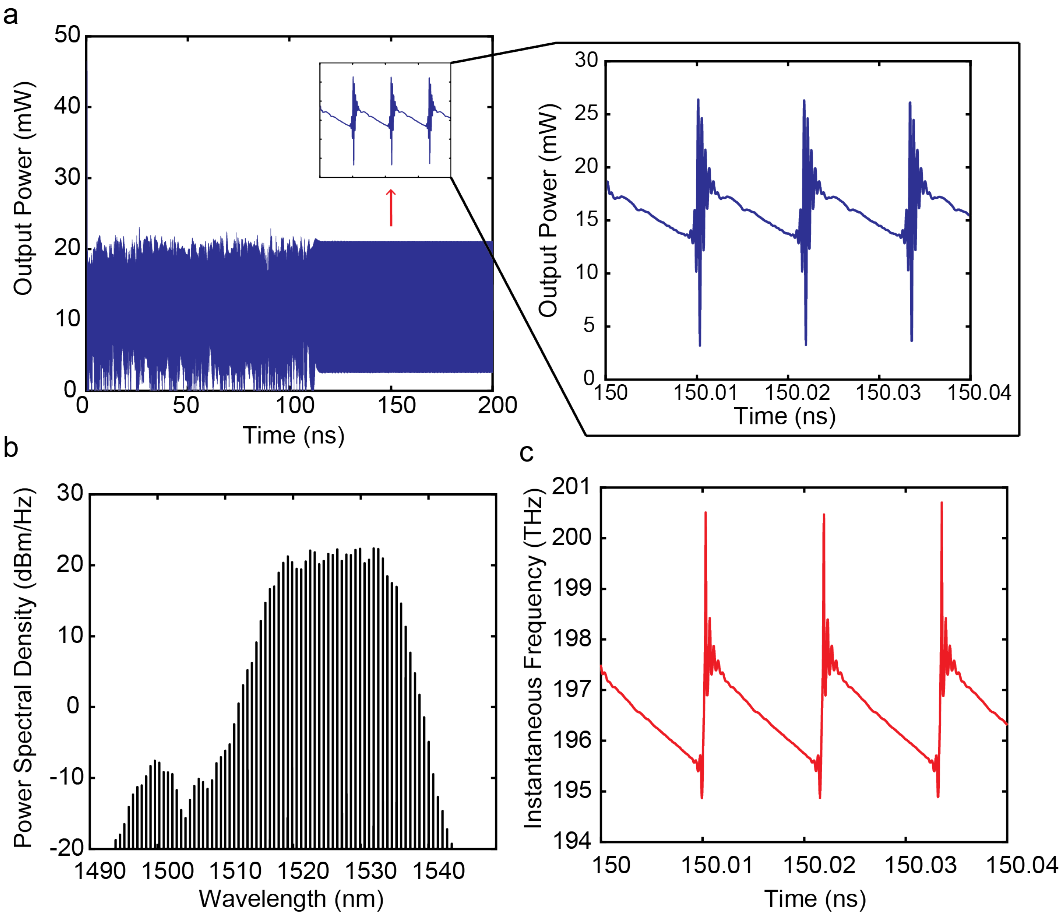

Figure 6.2: a) The temporal output of the single-section quantum well device at $\eta I_{in} = 25$ mA with a zoomed inset to show the detailed dynamics. The output is quasi-CW except for a short burst that repeats every round trip. A steady state is reached for $t > 110$ ns b) The power spectral density of the last 100 ns of the temporal output in log scale showing a broad comb c) the instantaneous frequency of the laser output, which is also sweeping periodically, showing the FM nature of the comb.

To show that the modes in the comb we calculated are indeed phase coherent with one another, we perform some phase calculations in frequency domain. If we apply a spectral filter in frequency domain in the form of a quadratic phase

$$\tilde{E}_{comp}(z,\omega) = e^{-i\mathrm{GDD}\omega^2}\tilde{E}(z,\omega) \tag{6.8}$$

where $\tilde{E}(z,\omega)$ is the Fourier transform of $E_+(z,t)$ and GDD is the group delay dispersion, we can compensate for the quadratic phase in our output and realign all

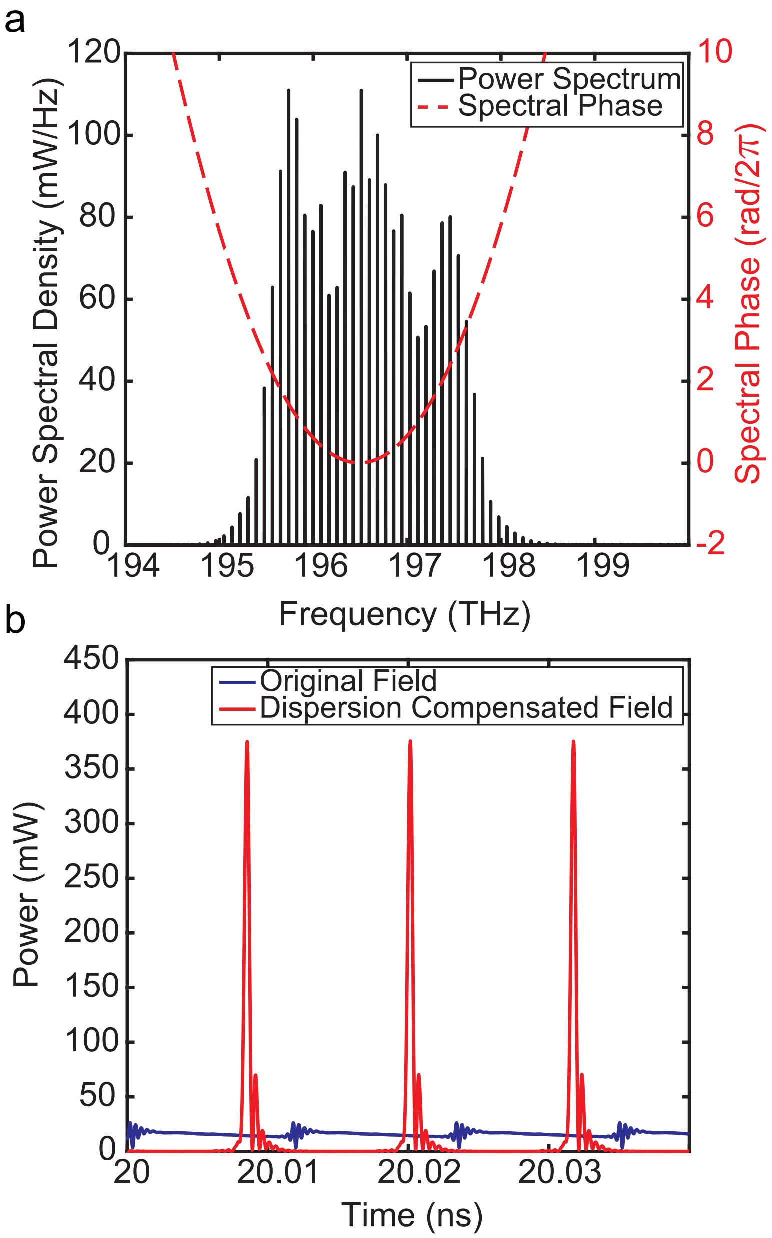

Figure 6.3: a) the power spectral density in linear scale along with the spectral phase b) The spectrum is compensated for dispersion and inverse Fourier transformed to produce a series of short pulses separated by the cavity round trip time. The group delay dispersion (GDD) is calculated to be 0.41 ps^2.

modes to precisely the same phase value. To find the approximate spectral phase, we sweep the GDD until we find the value that most coherently transforms the time domain signal into a series of pulses. This GDD is inserted as the approximate phase and plotted (along with the power spectral density) in linear scale in Figure 6.3a. We apply this phase compensation at the optimum GDD and inverse Fourier transform the signal to show that the time-domain output power has transformed into a series of short pulses as seen in Figure 6.3b with pulse width of about 390 fs. The original field is plotted for comparison.

This demonstrates that our FM, quasi-CW power output has modes that are all phase-locked but not necessarily all at the same phase value. This explains why the modes do not all constructively interfere at one point in time. However, if we compensate for this phase, either numerically as we have done here or experimentally by propagating the FM signal through an anomalous dispersion material [55, 84], we are able to obtain a series of short pulses.

During our simulations, we find that the third order nonlinearities (two-photon absorption and Kerr effect) do not play a significant role in frequency comb generation, likely due to the fact our laser output is quasi-CW instead of pulses. Two-photon absorption does appear to help stabilize our numerical stepping scheme due to increased losses in the cavity, but the Kerr effect has almost no effect at all. The physics of why exactly the laser diode would behave this way, with only a single section and no saturable absorber, is explored in Chapter VII.

6.3 Conclusion

Our results in this chapter show that FM comb generation directly from a laser diode is possible. The frequency comb has phase-locked modes with a quadratic spectral phase that can be compensated to form a series of short pulses with a bandwidth of about 1-3 THz. This FM solution allows us to avoid some of the detrimental phase effects stemming from carrier dynamics, as seen in the pulse amplification calculations. Ultimately, the great advantage of these laser diodes is that they can be easily used, cheaply produced, and embedded into various electronics, as they only require a power supply and no additional optical components. This technology will be a major step in bringing the advantages of frequency combs outside the laboratory.

CHAPTER VII

Physics of Frequency Modulated Comb Generation in Laser Diodes

With the completion of our full theoretical model that can predict and replicate the generation of FM combs from laser diodes in experiments, we now delve a bit deeper into the physics of frequency comb generation in quantum well laser diodes.

On the surface, it is not quite clear why the inclusion of SHB would generate a frequency comb, let alone an FM comb. This question has been investigated in quantum dot and QC systems [60, 85, 62, 63]. In [60], modeling QD and quantum dash lasers, the authors used an additional gain compression term to model SHB which also gave rise to multimode operation, as we saw in our model. The authors also mention that the large inhomogeneous gain broadening provided by the quantum dot gain medium is also essential, making great effort to properly model the inhomogeneous distribution of quantum dots. In other QD papers [86, 87], additional physical effects are also mentioned as important in affecting comb generation, including four-wave mixing (FWM), Kerr nonlinearities, and group velocity dispersion (GVD). In QC systems, previous works [62, 63] place significant focus on the effect of the short upper state population lifetime for intraband transitions ($\sim$ 1 ps in QC lasers), which are typically much shorter than interband transitions ($\sim$ 1 ns, as is the case in our lasers). The short gain recovery in QC lasers naturally favors the FM mode-locked state as opposed to the traditional mode-locking that generates a pulse train.

In this chapter, we study the physics in quantum well systems to answer the question of how an FM comb is generated in a single-section laser diode. We attempt to isolate the essential physical mechanisms and find the most important effects without the large amount of microscopic details already in our full model. We also apply some of our findings on quantum wells to QD and QC systems, making some important comparisons of the physical characteristics of each system.

7.1 Background

From the modeling results so far, we can hypothesize that we require at least two physical effects for comb generation: a mechanism for multimode operation and a mechanism for locking the phases together. Typically, either inhomogeneous broadening or SHB can lead to multimode lasing [68]. It is clear from the preceding chapters that SHB is essential for multimode operation, especially in our semiconductor cavities in which the homogeneous linewidth is large relative to the free spectral range (FSR) of the cavity. Because of gain competition, the laser operates mostly in single mode unless we have SHB. The effects of SHB have been investigated in past works such as [71, 75]. where SHB is clearly linked to multimode operation. Once we have multimode lasing, however, the modes still need to be locked together. For this, we find gain-mediated four-wave mixing (FWM) as the most likely candidate responsible for phase locking. In semiconductor lasers, the FWM arises from either intraband population pulsations or interband population fluctuations which nonlinearly couples the adjacent cavity modes [88] through the gain term, thus locking their phases together. This is not the same as the third order nonlinearity responsible for FWM in many other media such as fibers and crystals [13, 15]. This distinction becomes quite important as they affect laser operation in different ways - the most important of which is that the phase locking requires the different optical modes to share the same group of carriers for gain and phase modulation via FWM. In other words, a laser emitting multiple frequencies with only inhomogeneous broadening for multimode lasing will, by definition, not share common carriers between its optical modes. Such a laser would not be phase coherent, as it does not have the FWM component.

There have been many experimental and theoretical papers documenting FWM in bulk and quantum well semiconductor optical amplifiers (SOAs) and lasers [89, 90]. In particular, [90] shows significant FWM efficiency in SOAs even up to detunings of 10 nm or about 1 THz at the 1550 nm operating point. This detuning is already much larger than the normal FSR of a typical semiconductor diode laser, which has longitudinal mode spacings of 10 GHz - 100 GHz. This suggests that FWM should be significant in QW lasers. Indeed, it has been shown that FWM is responsible for the passive mode locking that leads to self-pulsations in quantum well distributed Bragg reflector (DBR) lasers [91]. On the other hand, SHB is typically discarded [88, 92, 93] as the carrier diffusion length in quantum wells ($\sim$ 2 - 3 μm) is very long relative to the half wavelength inside the cavity, smearing out the spatial carrier grating. However, the calculation of these diffusion lengths relies on the optical cavity being empty of light or mostly empty in the case of pulsed inputs. So while the diffusion length is very long during diffusion measurements in which pump-probe pulses are used [94], the diffusion length can be shortened considerably when light is always present inside the cavity. We find that in the case of a free running Fabry-Perot laser operating under a quasi-CW state, the carrier lifetime is significantly shortened due to the continuous presence of stimulated emission [95]. Such a difference not only reduces the diffusion length and leads to SHB effects, but the shortening of the lifetime also aids in the FWM process. The shorter carrier lifetime modifies our interband laser to be more similar to the QC case.

7.2 Derivation of Simplified Model

We illustrate these ideas by taking our full model and reducing it to gain some insight into the physics. The goal is to find a reduced set of equations in which analytic solutions can be found and physical effects clearly discerned.

We first simplify the carrier equations. The SCH population equation is removed, thus ignoring carrier capture and escape dynamics. Carrier injection is now directly incorporated into the quantum well population equations. However, instead of multiple carrier equations to model inhomogeneous broadening, we simplify the carrier groups into just one group centered at the band edge. In doing this, the quantum well carriers no longer have a dependence upon the transverse energy E_t. This, in essence, ignores the effects of inhomogeneous broadening and assumes only a homogenous group of carriers with a Lorentzian gain distribution. In addition, we revert back to a pure two-level system in which $\rho_{qw} = \rho^e_{qw} = \rho^h_{qw}$, thus having to model only one of the carrier types. However, we retain the effects of SHB by keeping the grating term. Under these simplifications, Equations 6.6 become

$$\frac{\partial \rho_{qw}}{\partial t} = \frac{\eta I_{in}}{q N_{qw}}(1-\rho_{qw}) - \frac{\rho_{qw}}{\tau_{sp}} - R(2\rho_{qw}-1)\mathrm{Re}(E^*_+ F_+ + E^*_- F_-) \tag{7.1a}$$

$$\frac{d\rho_g}{dt} = -\frac{\rho_g}{\tau_{sp}} - 4k_0^2 D\rho_g - R\left[\frac{1}{2}(E^*_+ F_- + F^*_+ E_-)(2\rho_{qw}-1) + 2\mathrm{Re}(E^*_+ F_+ + E^*_- F_-)\rho_g\right], \tag{7.1b}$$

where

$$N_{qw} = D_r^{2D} \times (\hbar\Gamma) \times W L h_{qw} \tag{7.2}$$

is the number density of states, D_r^{2D} is the traditional, reduced 2-D density of states, and

$$R = \frac{8gL}{\hbar\omega_0 N_{qw}} \tag{7.3}$$

is the simplified recombination coefficient. The new gain coefficient is related to g_0 via

$$g = \frac{\hbar\Gamma}{\hbar\omega_0} g_0 \,. \tag{7.4}$$

We note that instead of the single carrier group put in an energy bin of width ΔE_t, we expand this width to be $\hbar\Gamma$ in order to capture gain from the entire homogeneous bandwidth. The filtered field $F_{\pm}$ still retains its original form, albeit no longer with an E_t dependence

$$F_{\pm} = \Gamma \int_{-\infty}^{t} dt' e^{-\Gamma(t-t')} E_{\pm}(z, t') \,. \tag{7.5}$$

The traveling wave equations are now simplified as well, as we remove the terms related to third-order nonlinearity and second order dispersion. We retain the linear loss and noise terms and write the traveling waves as

$$\frac{\partial E_+}{\partial z} + \frac{1}{v_g}\frac{\partial E_+}{\partial t} = -\frac{\alpha}{2}E_+ + g\left[(2\rho_{qw} - 1)F_+ + 2\rho_g F_-\right] + \tilde{S}_{sp} \tag{7.6a}$$

$$-\frac{\partial E_-}{\partial z} + \frac{1}{v_g}\frac{\partial E_-}{\partial t} = -\frac{\alpha}{2}E_- + g\left[(2\rho_{qw} - 1)F_- + 2\rho_g^* F_+\right] + \tilde{S}_{sp} \,. \tag{7.6b}$$

Equations 7.1 and 7.6 contain the physical effects of FWM via population pulsations in ρ_{qw} and the physical effects of SHB via the presence of ρ_g. We do note that, while the other physical effects we discarded including chromatic and waveguide dispersion, Kerr nonlinearities, and inhomogeneous gain broadening are certainly very important and can greatly affect comb performance, we ignore them here to demonstrate that they are not essential for FM comb formation. This clarifies not only clarifies the essentials, but also allows us to focus in-depth on the important physical effects of FWM and SHB. Equations 7.1, 7.6 may look much simpler than those in the full model, but finding analytic solutions is still far from easy.

7.3 Effects of four-wave mixing

To start analyzing the physics, we first take a look at the effects of FWM. For this, we assume that the grating term is zero and ignore it for now. We ask the question, "what effect does FWM have on a single mode laser?" We use perturbation theory to analyze the growth of adjacent cavity modes in a laser operating in single mode in the presence of FWM. The simplified equations without the grating term become

$$\frac{\partial \rho_{qw}}{\partial t} = \frac{\eta I_{in}}{q N_{qw}}(1-\rho_{qw}) - \frac{\rho_{qw}}{\tau_{sp}} - R(2\rho_{qw}-1)\mathrm{Re}(E_+^* F_+ + E_-^* F_-) \tag{7.7}$$

$$\begin{aligned} \frac{\partial E_+}{\partial z} + \frac{1}{v_g}\frac{\partial E_+}{\partial t} &= -\frac{\alpha}{2}E_+ + g(2\rho_{qw}-1)F_+ + \tilde{S}_{sp} && \text{(7.8a)} \\ -\frac{\partial E_-}{\partial z} + \frac{1}{v_g}\frac{\partial E_-}{\partial t} &= -\frac{\alpha}{2}E_- + g(2\rho_{qw}-1)F_- + \tilde{S}_{sp}\,. && \text{(7.8b)} \end{aligned}$$

We assume that the electric field is operating in a single mode at optical frequency ω_0 and only strongly interacts with the nearest adjacent cavity modes. Thus the forward and backward electric fields can be written as

$$E_+ = A_0 + A_1 e^{i\omega_s t} + A_{-1} e^{-i\omega_s t} \tag{7.9a}$$

$$E_- = B_0 + B_1 e^{i\omega_s t} + B_{-1} e^{-i\omega_s t}\,, \tag{7.9b}$$

where A_n is the nth forward mode envelope, and B_n is the nth backward mode envelope. The cavity spacing or FSR is given by $\nu_{fsr} = \omega_s/2\pi$.

Our perturbation approach is as follows: we first assume the laser is only in single mode, with envelopes $A_{\pm 1}$ and $B_{\pm 1}$ being zero and only A_0 and B_0 being nonzero; then we solve for a steady state solution for the field and the carriers in the single mode state; lastly we take a look at the growth and behavior of the side modes $A_{\pm 1}$, $B_{\pm 1}$ as a perturbation to the aforementioned steady state, single mode solution. Using this approach, we extract the effects of FWM on our system. This approach has some resemblance to the gain competition modeling in Siegman's *Lasers* [68].

Solving for a steady state, the filtered field (Equation 7.5) becomes simply $F_+ = A_0$, $F_- = B_0$, and the rate equations simplify to

$$\rho_0 = \tau_{cw} \frac{\eta I_{in}}{q N_{qw}} + \tau_{cw} R(|A_0|^2 + |B_0|^2) \tag{7.10}$$

$$\tau_{cw} = \left[\frac{\eta I_{in}}{q N_{qw}} + \frac{1}{\tau_{sp}} + 2R(|A_0|^2 + |B_0|^2) \right]^{-1} , \tag{7.11}$$

where we have defined the dc carrier lifetime as τ_{cw}. We note right away that if there is a significant amount of light, or if the terms $|A_0|^2$ or $|B_0|^2$ become large, τ_{cw} can be significantly reduced from its dark cavity value of τ_{sp}. Inserting Equation 7.10 into the traveling wave equation (Equation 7.8), we obtain

$$\frac{dA_0}{dz} = -\frac{\alpha}{2} A_0 + \frac{g_{eff}}{2} A_0 \tag{7.12a}$$

$$-\frac{dB_0}{dz} = -\frac{\alpha}{2} B_0 + \frac{g_{eff}}{2} B_0 \, , \tag{7.12b}$$

where the effective gain is written

$$g_{eff} = g\left[2\tau_{cw}\frac{\eta I_{in}}{qN_{qw}} + 2\tau_{cw}R(|A_0|^2 + |B_0|^2) - 1\right] . \tag{7.13}$$

Equations 7.12 can be solved by introducing an auxiliary variable θ [96] such that

$$\frac{d\theta}{dz} = -\frac{\alpha}{2} + \frac{g_{eff}}{2} . \tag{7.14}$$

Substituting this into Equations 7.12, we obtain a much simpler set of equations

$$\frac{dA_0}{d\theta} = A_0 \tag{7.15}$$

$$-\frac{dB_0}{d\theta} = B_0 . \tag{7.16}$$

The solution is a straightforward integration with respect to θ and yields

$$A_0 = C_1 e^{\int dz' \frac{d\theta}{dz'}}$$

$$B_0 = C_2 e^{-\int dz' \frac{d\theta}{dz'}} ,$$

and converting back to our original variables,

$$A_0 = C_1 \exp\left(-\frac{\alpha z}{2} + \frac{1}{2}\int_0^z dz' g_{eff}\right) \tag{7.17a}$$

$$B_0 = C_2 \exp\left(\frac{\alpha z}{2} - \frac{1}{2}\int_0^z dz' g_{eff}\right) . \tag{7.17b}$$

Here, C_1 and C_2 are arbitrary integration constants. To complete the solution, we apply the two reflective boundary conditions, $A_0(0) = \sqrt{r}B_0(0)$ and $B_0(L) = \sqrt{r}A_0(L)$, where r is the power reflection coefficient. This results in an expression for the effective gain in steady state.

$$\frac{1}{L}\int_0^L dz g_{eff} = \alpha + \frac{1}{2L}\ln(1/r^2) = g_{th} \tag{7.18}$$

Here is our first major result - we see that the total, round trip integrated gain of the cavity is equal to the threshold gain in steady state. The fact that the laser gain is clamped to threshold is a well known feature of CW lasers. This is important in our subsequent stability analysis, as it suggests the side cavity modes will have difficulty achieving lasing threshold due to this gain clamping. Conceivably, one can solve for the total power inside the cavity with a given input pump I_{in} via Equation 7.18 and then subsequently relate that to the constants C_1 and C_2 to obtain a formal solution for the central cavity mode. However, because the effects of FWM are not dependent upon the values of C_1 and C_2, we leave it as an exercise to the reader.

Now consider the behavior of the side modes, $A_{\pm 1}$ and $B_{\pm 1}$, in the presence of A_0 and B_0. Because we assume the effects of the side modes are perturbative, at least initially, we only keep terms that are linear in these side mode amplitudes. However, the central mode, A_0, B_0, is significant so we retain nonlinearities associated with them. The perturbative approach is useful as the initial growth or decay of the side modes will determine the stability of single mode operation. We modify the population term to include a time harmonic exponential to represent population pulsations, as given by

$$\rho_{qw} = \rho_0 + \rho_1 e^{i\omega_s t} + \rho_1^* e^{-i\omega_s t}\,. \tag{7.19}$$

The filtered field is also modified to include the side modes and the convolution integral can be expanded as such

$$\begin{aligned}
F_+ &= \Gamma \int_{-\infty}^{t} dt' e^{-\Gamma(t-t')}(A_0 + A_1 e^{i\omega_s t} + A_{-1}e^{-i\omega_s t}) \\
F_- &= \Gamma \int_{-\infty}^{t} dt' e^{-\Gamma(t-t')}(B_0 + B_1 e^{i\omega_s t} + B_{-1}e^{-i\omega_s t}) \,,
\end{aligned}$$

and assuming, again, that the envelopes are very slowly varying compared to the exponential decay, the integral is evaluated to be

$$F_+ = c_s^* A_{-1} e^{-i\omega_s t} + A_0 + c_s A_1 e^{i\omega_s t} \tag{7.20a}$$

$$F_- = c_s^* B_{-1} e^{-i\omega_s t} + B_0 + c_s B_1 e^{i\omega_s t} \,. \tag{7.20b}$$

The constant c_s comes from the integration and defined as

$$c_s = \frac{1}{1 + i\omega_s/\Gamma} \,. \tag{7.21}$$

Using these definitions, an equation for the time varying population term describing population pulsations is found to be

$$\begin{aligned}
\frac{\partial \rho_1}{\partial t} + i\omega_s \rho_1 = &- \frac{\rho_1}{\tau_{sp}} - 2R(|A_0|^2 + |B_0|^2)\rho_1 \\
&- R(2\rho_0 - 1)\frac{c_s + 1}{2}\left(A_0^* A_1 + A_0 A_{-1}^* + B_0^* B_1 + B_0 B_{-1}^*\right) \,,
\end{aligned} \tag{7.22}$$

whose steady state solution is easily calculated

$$\rho_1 = -R\tau_{ac}(2\rho_0 - 1)\frac{c_s + 1}{2}\left(A_0^* A_1 + A_0 A_{-1}^* + B_0^* B_1 + B_0 B_{-1}^*\right) \,. \tag{7.23}$$

The lifetime for these pulsations is defined as

$$\tau_p = \left[\frac{1}{\tau_{sp}} + i\omega_s + 2R(|A_0|^2 + |B_0|^2)\right]^{-1} \,. \tag{7.24}$$

The steady state electric field equations for the side modes can be found by substituting Equations 7.23, 7.27, and 7.9 into Equations 7.6, assuming still that the grating term ρ_g is zero. The four side mode equations are obtained

$$\begin{aligned}\frac{dA_1}{dz} =& -\frac{\alpha}{2}A_1 + \frac{g_{eff}}{2}c_s A_1 \\ & - g_2\left(|A_0|^2 A_1 + A_0^2 A_{-1}^* + A_0 B_0^* B_1 e^{2i\Delta k} + A_0 B_0 B_{-1}^* e^{2i\Delta k}\right)\end{aligned} \tag{7.25a}$$

$$\begin{aligned}\frac{dA_{-1}}{dz} =& -\frac{\alpha}{2}A_{-1} + \frac{g_{eff}}{2}c_s^* A_{-1} \\ & - g_2^*\left(|A_0|^2 A_{-1} + A_0^2 A_1^* + B_0 A_0 B_1^* e^{-2i\Delta k} + B_0^* A_0 B_{-1} e^{-2i\Delta k}\right)\end{aligned} \tag{7.25b}$$

$$\begin{aligned}-\frac{dB_1}{dz} =& -\frac{\alpha}{2}B_1 + \frac{g_{eff}}{2}c_s B_1 \\ & - g_2\left(|B_0|^2 B_1 + B_0^2 B_{-1}^* + B_0 A_0^* A_1 e^{-2i\Delta k} + B_0 A_0 A_{-1}^* e^{-2i\Delta k}\right)\end{aligned} \tag{7.25c}$$

$$\begin{aligned}-\frac{dB_{-1}}{dz} =& -\frac{\alpha}{2}B_{-1} + \frac{g_{eff}}{2}c_s^* B_{-1} \\ & - g_2^*\left(|B_0|^2 B_{-1} + B_0^2 B_1^* + B_0 A_0 A_1^* e^{2i\Delta k} + B_0 A_0^* A_{-1} e^{2i\Delta k}\right)\end{aligned} \tag{7.25d}$$

where Δk is the difference in the propagation vectors between the central and side modes. We also introduce a gain saturation

$$g_2 = gR(2\rho_0 - 1)\tau_p \frac{c_s + 1}{2} \tag{7.26}$$

We can make a an additional simplification by noting that, because it is typical that $\omega_s << \Gamma$ as we mentioned before in semiconductor lasers, we take $c_s \approx 1$. Thus the filtered field is simply the sum of the three modes

$$F_+ = A_{-1}e^{-i\omega_s t} + A_0 + A_1 e^{i\omega_s t} \tag{7.27a}$$

$$F_- = B_{-1}e^{-i\omega_s t} + B_0 + B_1 e^{i\omega_s t}\,, \tag{7.27b}$$

and the wave equations simplify to

$$\begin{aligned}\frac{dA_1}{dz} =& -\frac{\alpha}{2}A_1 + \frac{g_{eff}}{2}A_1 \\ &- g_2\left(|A_0|^2 A_1 + A_0^2 A_{-1}^* + A_0 B_0^* B_1 e^{2i\Delta k} + A_0 B_0 B_{-1}^* e^{2i\Delta k}\right)\end{aligned} \tag{7.28a}$$

$$\begin{aligned}\frac{dA_{-1}}{dz} =& -\frac{\alpha}{2}A_{-1} + \frac{g_{eff}}{2}A_{-1} \\ &- g_2\left(|A_0|^2 A_{-1} + A_0^2 A_1^* + B_0 A_0 B_1^* e^{-2i\Delta k} + B_0^* A_0 B_{-1} e^{-2i\Delta k}\right)\end{aligned} \tag{7.28b}$$

$$\begin{aligned}-\frac{dB_1}{dz} =& -\frac{\alpha}{2}B_1 + \frac{g_{eff}}{2}B_1 \\ &- g_2\left(|B_0|^2 B_1 + B_0^2 B_{-1}^* + B_0 A_0^* A_1 e^{-2i\Delta k} + B_0 A_0 A_{-1}^* e^{-2i\Delta k}\right)\end{aligned} \tag{7.28c}$$

$$\begin{aligned}-\frac{dB_{-1}}{dz} =& -\frac{\alpha}{2}B_{-1} + \frac{g_{eff}}{2}B_{-1} \\ &- g_2\left(|B_0|^2 B_{-1} + B_0^2 B_1^* + B_0 A_0 A_1^* e^{2i\Delta k} + B_0 A_0^* A_{-1} e^{2i\Delta k}\right)\,.\end{aligned} \tag{7.28d}$$

Equations 7.28 form the basis of investigating FWM. We can transform them into an eigenvalue equation by assuming that, based on our single mode analysis, the effective gain is equal to the threshold gain, meaning there is no net gain or loss inside the cavity. We can therefore ignore the gain and loss terms. Moreover, we can further simplify by ignoring the spatially phase mismatched terms, decoupling the forward and backward waves and writing separate equations for the forward and backward waves. We also explicitly write the center mode in terms of magnitude and phase, $A_0 = |A_0|e^{i\psi_0^+}$, $B_0 = |B_0|e^{i\psi_0^-}$, as the phase relation between the modes will be important. This transforms the forward and backward side mode equations to be

$$\begin{aligned} \frac{dA_1}{dz} =& - g_2|A_0|^2 \left(A_1 + A_{-1}^* e^{2i\psi_0^+}\right) && (7.29a) \\ \frac{dA_{-1}^*}{dz} =& - g_2|A_0|^2 \left(A_{-1}^* + A_1 e^{-2i\psi_0^+}\right) && (7.29b) \\ \frac{dB_1}{dz} =& g_2|B_0|^2 \left(B_1 + B_{-1}^* e^{2i\psi_0^-}\right) && (7.29c) \\ \frac{dB_{-1}^*}{dz} =& g_2|B_0|^2 \left(B_{-1}^* + B_1 e^{-2i\psi_0^-}\right) \ . && (7.29d) \end{aligned}$$

At last, we have a highly simplified set of equations that describe the major effects of population pulsations caused by the interference of two adjacent electric field cavity modes. The first effect, as seen in the first term in Equations 7.29, is a type of self-saturation that reduces the overall gain of the field. This self-saturation is sometimes called spectral hole burning in the literature [88]. This is somewhat of a misnomer, as it is quite different from spectral hole burning in the physics community which typically refers to saturation of a group of carriers or atoms that is inhomogeneously broadened, reducing the gain and burning a hole in the gain spectrum [14]. The second effect is the FWM term that we expect. The second term in the bracket of Equations 7.29 couples three different waves and is highly phase dependent. The phases of the center mode, $\psi_0^\pm$ can be shown to be constant in z by expanding Equations 7.12 and seeing that $d\psi_0^\pm/dz = 0$.

We can solve Equations 7.29 by solving for the system's eigenfunctions. Again, we substitute the auxiliary variables $\theta^\pm$, but now with the expressions

$$\frac{d\theta^+}{dz} = g_2|A_0|^2 \tag{7.30}$$

$$\frac{d\theta^-}{dz} = g_2|B_0|^2 \, . \tag{7.31}$$

The forward and backward waves each reduce to a separate 2×2 matrix and can be written

$$\frac{d}{d\theta^+}\begin{bmatrix} A_1 \\ A_{-1}^* \end{bmatrix} = \begin{bmatrix} -1 & -e^{2i\psi_0^+} \\ -e^{-2i\psi_0^+} & -1 \end{bmatrix}\begin{bmatrix} A_1 \\ A_{-1}^* \end{bmatrix} \tag{7.32a}$$

$$\frac{d}{d\theta^-}\begin{bmatrix} B_1 \\ B_{-1}^* \end{bmatrix} = \begin{bmatrix} 1 & e^{2i\psi_0^-} \\ e^{-2i\psi_0^-} & 1 \end{bmatrix}\begin{bmatrix} B_1 \\ B_{-1}^* \end{bmatrix} \tag{7.32b}$$

The solutions to Equations 7.32 consist of the eigenvalues $\lambda_1 = 0$, $\lambda_2 = \pm 2$, depending on the direction of the wave. The general solution for the side modes are

$$\begin{bmatrix} A_1 \\ A_{-1}^* \end{bmatrix} = C_1 \begin{bmatrix} -e^{2i\psi_0^+} \\ 1 \end{bmatrix} + C_2 \exp\left(-2\int_0^z dz' g_2 |A_0|^2\right)\begin{bmatrix} e^{2i\psi_0^+} \\ 1 \end{bmatrix} \tag{7.33a}$$

$$\begin{bmatrix} B_1 \\ B_{-1}^* \end{bmatrix} = D_1 \begin{bmatrix} -e^{2i\psi_0^-} \\ 1 \end{bmatrix} + D_2 \exp\left(2\int_0^z dz' g_2 |A_0|^2\right)\begin{bmatrix} e^{2i\psi_0^-} \\ 1 \end{bmatrix}, \tag{7.33b}$$

where C_1, C_2, D_1, and D_2 are arbitrary constants. We see from Equations 7.33 that it is not possible for either side mode A_1 , B_1 or A_{-1}, B_{-1} to grow through FWM. The eigenmodes of propagation are either net loss or zero gain. This is supported the fact that the integral in the exponential is always positive. Moreover, simply increasing the strength of FWM by increasing g_2 does not lead to multimode lasing, as it simultaneously increases the self saturation due to the population pulsations.

Thus the major result of FWM in QW diode lasers is clear. FWM can certainly exist in laser diodes but is not strong enough to sustain additional modes, as it simultaneously increases gain saturation of these side modes. As found in the single mode analysis, there is no net gain or loss inside the cavity when the laser is well above threshold current, due to the clamping of the gain to threshold gain. We note that this is quite different from Kerr combs generated from microresonators, which typically require a very strong external pump laser [97] able to provide the power necessary to sustain the modes. The same effect is also present in FWM experiments in SOAs in which external lasers (CW or pulsed) are used. In addition, some FWM experiments can have lower power inputs that only weakly saturate the gain as opposed to strong saturation in a free running laser. The weak saturation allows the side band modes to achieve gain [90].

7.4 Spatial Hole Burning Analysis

We have found that the requirement of multimode lasing remains unfulfilled with only FWM, as we expected based on our previous numerical calculations. We now take a look at how the grating equation changes the dynamics and reduces gain competition.

Reverting back to our single mode analysis, we assume the population grating term is only significantly generated by the strong central mode, as the side bands are negligible in their contributions to the carrier grating in the perturbation approximation. Thus we write $\rho_g \rightarrow \rho_{g0}$. Substituting this into the grating equation (Equation 7.1b), we obtain

$$\frac{d\rho_{g0}}{dt} = -\frac{\rho_{g0}}{\tau_{sp}} - 4k_0^2 D\rho_{g0} - R(2\rho_0 - 1)B_0 A_0^* - 2R(|A_0|^2 + |B_0|^2)\rho_{g0} \,. \tag{7.34}$$

The steady state solution is given by

$$\rho_{g0} = -R(2\rho_0 - 1)\tau_g B_0 A_0^* \,, \tag{7.35}$$

and we define the grating lifetime as

$$\tau_g = \left[\frac{1}{\tau_{sp}} + 4k_0^2 D + 2R(|A_0|^2 + |B_0|^2)\right]^{-1} \,. \tag{7.36}$$

The key component to this lifetime is the value of $4k_0^2D$, which varies significantly depending upon material and operating wavelength. Physically, this lifetime can be interpreted as the time it takes to diffuse one half wavelength inside the cavity. Using the solution in Equation 7.35 in the single mode wave equations, we obtain a modified set of equations for the steady state single mode

$$\begin{aligned} \frac{dA_0}{dz} &= -\frac{\alpha}{2}A_0 + \frac{g'_{eff}}{2}A_0 - gR(2\rho_0 - 1)\tau_g|B_0|^2A_0 && (7.37a) \\ -\frac{dB_0}{dz} &= -\frac{\alpha}{2}B_0 + \frac{g'_{eff}}{2}B_0 - gR(2\rho_0 - 1)\tau_g|A_0|^2B_0\,. && (7.37b) \end{aligned}$$

The presence of the additional losses from the carrier grating affects the steady state value of the gain and the intracavity fields. We can follow the same approach as before and derive a new expression for the effective gain (labeled g'_{eff}) with the effects of SHB

$$\frac{1}{L}\int_0^L dz g'_{eff} = g_{th} + \frac{2}{L}\int_0^L dz g_3|B_0|^2\,, \tag{7.38}$$

for the forward wave, and

$$\frac{1}{L}\int_0^L dz g'_{eff} = g_{th} + \frac{2}{L}\int_0^L dz g_3|A_0|^2\,, \tag{7.39}$$

for the backward wave. These should be identical, however, because of the symmetric nature of the Fabry-Perot cavity, the integrals of $|A_0|^2$ and $|B_0|^2$ evaluate to be the same. We introduce another gain saturation term

$$g_3 = gR(2\rho_0 - 1)\tau_g\,, \tag{7.40}$$

which is a measure of the strength of the carrier grating. The modified effective gain equations show that the overall steady state effective gain is no longer clamped to threshold, but is actually increased by the saturation intensity of the carrier grating. This physically means that the single mode can no longer take advantage of all the gain inside the cavity because of the standing waves. We therefore write the new effective gain as

$$g'_{eff} \approx g_{eff} + 2g_3|B_0|^2 \,, \tag{7.41}$$

where g_{eff} is the effective gain without spatial hole burning calculated in Equation 7.18, and $|B_0|^2$ can be replaced with $|A_0|^2$ depending on the direction of the wave.

This modified effective gain changes the dynamic of how the side modes behave. Going back to Equations 7.28 and inserting the new effective gain, we obtain

$$\begin{aligned}
\frac{dA_1}{dz} &= -\frac{\alpha}{2}A_1 + \frac{1}{2}\left(g_{eff} + 2g_3|B_0|^2\right)A_1 - g_2\left(|A_0|^2 A_1 + A_0^2 A_{-1}^*\right) && \text{(7.42a)}\\
\frac{dA_{-1}}{dz} &= -\frac{\alpha}{2}A_{-1} + \frac{1}{2}\left(g_{eff} + 2g_3|B_0|^2\right)A_{-1} - g_2\left(|A_0|^2 A_{-1} + A_0^2 A_1^*\right) && \text{(7.42b)}\\
-\frac{dB_1}{dz} &= -\frac{\alpha}{2}B_1 + \frac{1}{2}\left(g_{eff} + 2g_3|A_0|^2\right)B_1 - g_2\left(|B_0|^2 B_1 + B_0^2 B_{-1}^*\right) && \text{(7.42c)}\\
-\frac{dB_{-1}}{dz} &= -\frac{\alpha}{2}B_{-1} + \frac{1}{2}\left(g_{eff} + 2g_3|A_0|^2\right)B_{-1} - g_2\left(|B_0|^2 B_{-1} + B_0^2 B_1^*\right) \,. && \text{(7.42d)}
\end{aligned}$$

Once more, the gain and loss terms given by g_{eff}, the linear loss, and the cavity mirror losses will cancel in a round trip by definition of the threshold gain. We are then left with a modified set of FWM equations

$$\begin{aligned}
\frac{dA_1}{dz} &= (g_3|B_0|^2 - g_2|A_0|^2)A_1 - g_2|A_0|^2 A_{-1}^* e^{2i\psi_0^+} && \text{(7.43a)}\\
\frac{dA_{-1}^*}{dz} &= (g_3|B_0|^2 - g_2|A_0|^2)A_{-1}^* - g_2|A_0|^2 A_1 e^{-2i\psi_0^+} && \text{(7.43b)}\\
-\frac{dB_1}{dz} &= (g_3|A_0|^2 - g_2|B_0|^2)B_1 - g_2|B_0|^2 B_{-1}^* e^{2i\psi_0^-} && \text{(7.43c)}\\
-\frac{dB_{-1}^*}{dz} &= (g_3|A_0|^2 - g_2|B_0|^2)B_{-1}^* - g_2|B_0|^2 B_1 e^{-2i\psi_0^-} \,. && \text{(7.43d)}
\end{aligned}$$

Unfortunately, these equations are not as straightforward as the last two cases to solve. There is no clear integrating factor that can transform the 2 × 2 matrix into all constants for the eigenvalue solution. Fortunately, we can guess a solution based upon the idea that the gain saturation has been reduced by the value of g_3. We then write down the solutions

$$\begin{aligned}\begin{bmatrix} A_1 \\ A^*_{-1} \end{bmatrix} =& C_1 \exp\left(\int_0^z dz' g_3 |B_0|^2\right) \begin{bmatrix} -e^{2i\psi_0^+} \\ 1 \end{bmatrix} \\ &+ C_2 \exp\left(\int_0^z dz' \left(g_3|B_0|^2 - 2g_2|A_0|^2\right)\right) \begin{bmatrix} e^{2i\psi_0^+} \\ 1 \end{bmatrix}\end{aligned} \tag{7.44a}$$

$$\begin{aligned}\begin{bmatrix} B_1 \\ B^*_{-1} \end{bmatrix} =& D_1 \exp\left(-\int_0^z dz' g_3 |A_0|^2\right) \begin{bmatrix} -e^{2i\psi_0^-} \\ 1 \end{bmatrix} \\ &+ D_2 \exp\left(-\int_0^z dz' \left(g_3|B_0|^2 - 2g_2|A_0|^2\right)\right) \begin{bmatrix} e^{2i\psi_0^-} \\ 1 \end{bmatrix} .\end{aligned} \tag{7.44b}$$

These can be verified by taking each solution and taking the derivative, confirming that they obey Equations 7.43.

With the effects of SHB present, we see that both forward waves have the potential to grow exponentially when the integrals in the exponents are positive. In other words, the grating must be sufficiently strong, or equivalently, the grating lifetime must be sufficiently large, such that the gain competition is weakened from unused gain available inside the cavity. In this scenario, we will have sustained multimode lasing from reduced gain competition.

It is clear from our solution in Equations 7.44a that SHB reduces the effects of gain competition and increases the total gain seen by the side modes. It is primarily this SHB effect, not FWM, that induces multimode lasing. In other laser systems, the SHB effect is easily obtained: a long operating wavelength in QC lasers greatly reduces the ability of diffusion to wash out the spatial holes, while negligible diffusion

Parameter	Description	GaAs (InGaAsP) Value
L	Length of device	500 μm
W	Width of waveguide	4 μm
h_{qw}	Height of quantum well	5 nm
n_g	Group refractive index	3.5
α	Intrinsic waveguide loss	5 cm^{-1}
$\hbar\omega_0$	Central transition energy	1.5 eV (0.8 eV)
Γ	Homogenous linewidth	4.0 meV/$\hbar$
g	Modal gain coefficient	50 cm^{-1}
N_{qw}	Effective number of QW states	2.92×10^6
τ_{sp}	Spontaneous emission lifetime	1 ns
D	Ambipolar diffusion coefficient	20.0 cm^2/s (7.2 cm^2/s)

Table 7.1: Simulation parameters for QW traveling wave model for the GaAs and InGaAsP system.

in QD lasers allows for even very narrow gratings to survive. As we expected from our previous numerical calculations, SHB fulfills the multimode lasing requirement for generating a frequency comb.

7.5 Numerical Results

We can see the effects of SHB by solving Equations 7.1 and 7.6 numerically, as we did before. We solve the systems for two different materials - GaAs laser diodes operating at 800 nm wavelength, and InGaAsP operating at 1.550 μm wavelength. The full parameter list for both materials are in Table 7.1. The major differences in parameters are the different central emission wavelengths and a different diffusion coefficient.

We use a first-order Euler method along characteristics as in previous chapters. The results of this calculation for GaAs are shown in Figure 7.1 and for InGaAsP shown in Figure 7.2. The biggest contrast between the two results is the GaAs device exhibits only a single mode, while the InGaAsP has a spectrum with a comb structure. The relative strength of the central comb lines in Figure 7.2b has a remarkably similar

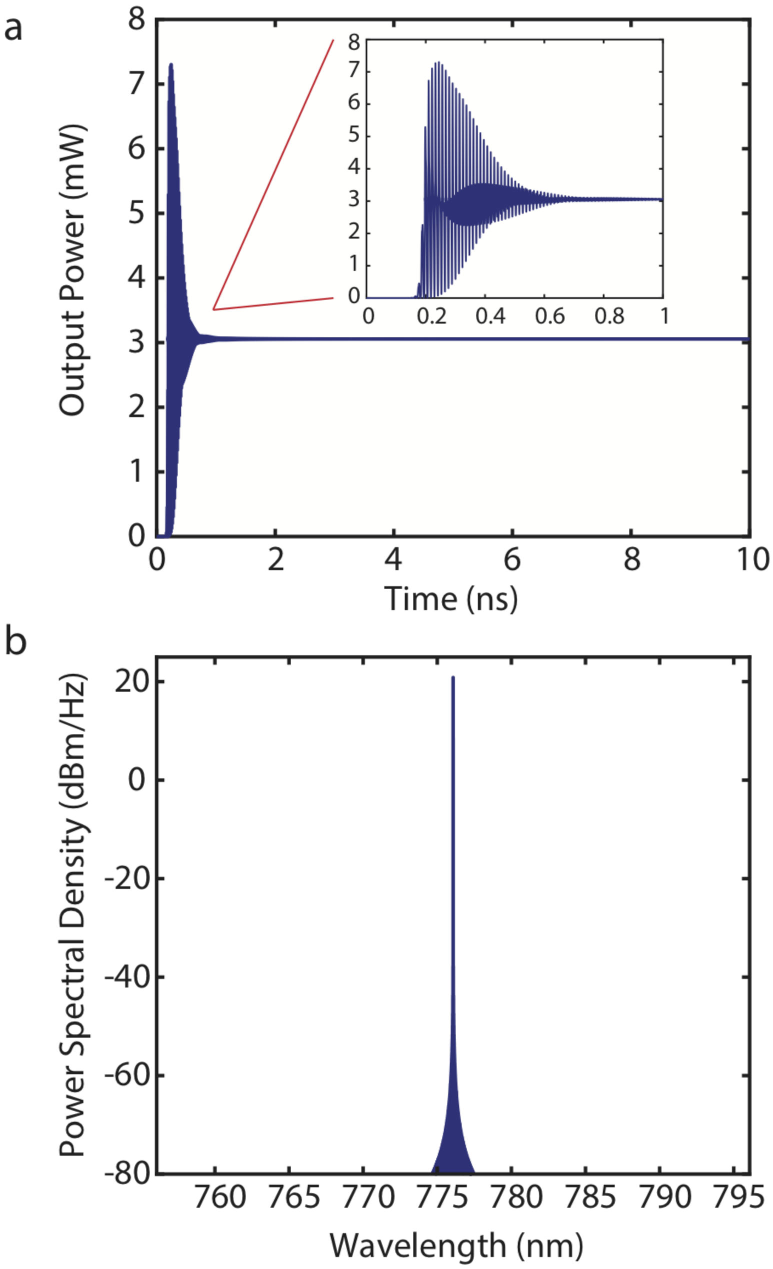

Figure 7.1: The calculated output optical power for a GaAs quantum well. a) the temporal power output, which settles down quickly to a single mode after the initial relaxation oscillations b) the spectrum of the GaAs temporal output showing a single mode.

shape to that of the spectrum obtained from experiment in [53]. Such a spectrum is distinctive of frequency modulation.

The determining criteria for comb generation is whether or not SHB is significant

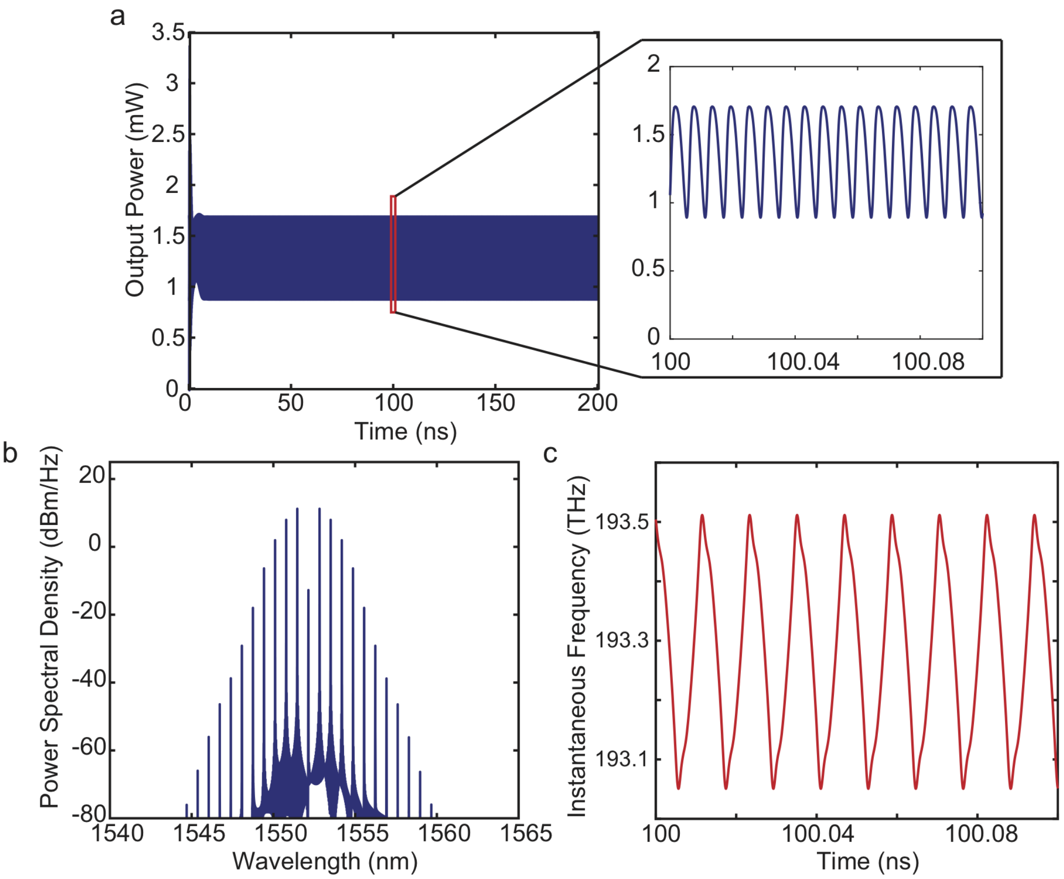

Figure 7.2: The calculated output optical power for an InGaAsP quantum well. a) the temporal power output which, in contrast with the GaAs solutions, does not settle to a single mode but eventually reaches a stable phase-locked state. A zoomed in inset at 100 ns is shown. b) the spectrum of the InGaAsP temporal output showing a frequency comb. c) the instantaneous frequency which shows a triangular, almost saw-tooth like output.

inside the cavity. If the diffusion length is much smaller than the half wavelength, or as modeled in our equations, that τ_g is large enough, then SHB will induce multimode lasing. Assuming a total intracavity power of $|A_0|^2 + |B_0|^2 \approx 5$ mW, the carrier lifetime and diffusion lengths are calculated to be

$$\begin{aligned} \tau_{cw,GaAs} &= 11 \text{ ps} \quad (7.45) \\ \tau_{cw,InGaAsP} &= 5.80 \text{ ps} \quad (7.46) \\ L_{D,GaAs} &= 149 \text{ nm} > \frac{\lambda_{GaAs}}{2n_g} = 118 \text{ nm} \quad (7.47) \\ L_{D,InGaAsP} &= 64.8 \text{ nm} < \frac{\lambda_{InGaAsP}}{2n_g} = 221 \text{ nm}\,. \quad (7.48) \end{aligned}$$

The GaAs has a significantly longer diffusion length, which essentially washes out within a half wavelength any spatial grating that exists. However, in the case of InGaAsP, the diffusion length is much shorter, only about a quarter of the half wavelength. Thus in InGaAsP QW devices operating at 1550 nm, multimode generation should be possible, arising from SHB effects.

The significance of SHB in quantum wells is not a binary effect. The strength of the grating depends on two important parameters - the wavelength and ambipolar diffusion coefficient. As seen in the numerical results, a strong enough SHB effect induces multimode lasing, which then allows FWM to lock the phases with an FM output. Therefore, we should be able to reduce the operating wavelength down to somewhere in between 1.55 μm and 800 nm and generate combs in this range by modifying the InGaAsP quantum wells to suit our needs. An interesting wavelength is 1310 nm, which is around the zero dispersion point of silica. These wavelengths will be revisited in testing our actual devices in the following chapters.

The effects of SHB become more clear as we isolate its effects in our calculation. We solve Equations 7.1 and 7.6 under the InGaAsP parameters but we then turn the grating term off for 50 ns $< t <$ 125 ns, and then turn it on again for $t >$ 125 ns. In Figure 7.3a, the dynamics of the this turn on and off can be seen in real time. The output reaches a stable, phase-locked state after some initial relaxation oscillations. Then, at 50 ns, it abruptly simplifies to a single mode due to the absence of SHB.

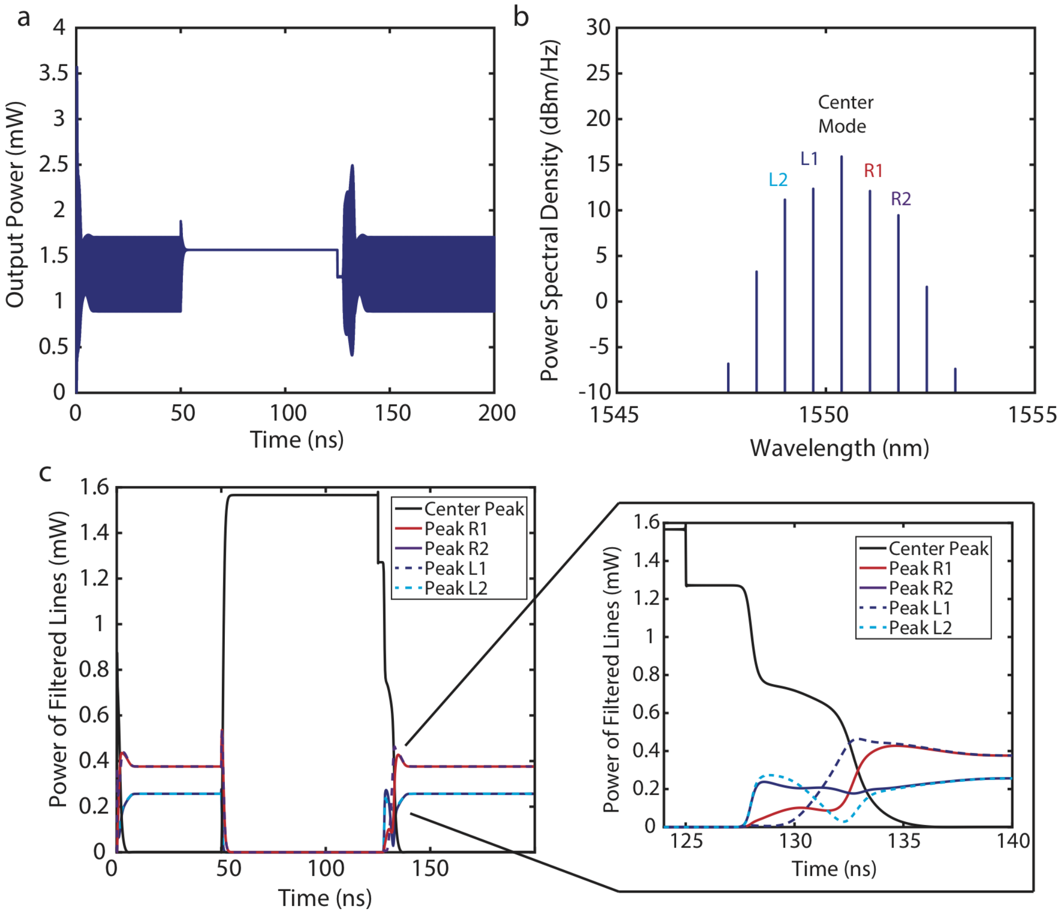

Figure 7.3: The results of turning off and on the population grating equation responsible for SHB. The grating is turned on for $t < 50$ ns, but turned off for $50 \text{ ns} < t < 125$ ns, and turned back on for $t > 125$ ns. a) The temporal output, which at first shows a phase-locked solution but abruptly reduces to a single mode after SHB is turned off. Once it is reenabled, the output goes multimode once more and finds the same phase-locked solution as before. b) The spectrum of the output. It is labeled to identify each mode. c) the modal envelopes after filtering the spectrum in a), with labels corresponding to each mode, with an inset at 125 ns showing the detailed dynamics during the transition from single mode to a multimode, phase-locked state. The center mode emerges as the strongest mode when SHB is turned off, but it is rather weak in the phase-locked solution.

Then after 125 ns, as expected after SHB is turned back on, the laser returns to multimode lasing and reaches the same phase-locked state in the first 50 ns.

The individual mode envelopes can be tracked (as labeled in Figure 7.3b) by applying a simple spectral filter to each comb line in frequency domain and inverse

Fourier transforming the central group of modes back into time domain. Figure 7.3c shows the results of the filtering and inverse transform. We see more clearly that, once SHB is turned off, all other modes decay rapidly until only the center mode remains. When SHB is turned back on, the central mode immediately drops in power due to increased self saturation, while simultaneously the side band amplitudes start increasing from reduced gain competition. Eventually the side bands become strong enough to saturate the central mode's gain and all modes mix together, reaching the same phase-locked state as before. The dynamics of the individual modes are consistent with our previous analytic results which show that the side bands grow primarily due to increased available gain due to increased self saturation of the central mode.

7.6 Phase locking in FM combs

Once the system is in multimode operation, we revisit the effects of FWM to see how it locks the phases together. For this section, we will focus on the forward propagating wave and look at just the amplitudes A_1 and A^*_{-1} (Equations 7.43a, b)

$$\frac{dA_1}{dz} =(g_3|B_0|^2 - g_2|A_0|^2)A_1 - g_2|A_0|^2 A^*_{-1} e^{2i\psi_0^+} \tag{7.49}$$

$$\frac{dA^*_{-1}}{dz} =(g_3|B_0|^2 - g_2|A_0|^2)A^*_{-1} - g_2|A_0|^2 A_1 e^{-2i\psi_0^+} . \tag{7.50}$$

We take a look at two distinct cases: one in which g_2 is purely real, and the second when g_2 is purely imaginary. Which regime we are in is determined by the lifetime τ_p. For $\omega_s << 1/\tau_{sp} + 2R(|A_0|^2 + |B_0|^2)$, then

$$\tau_p \approx \left[\frac{1}{\tau_{sp}} + 2R(|A_0|^2 + |B_0|^2)\right]^{-1} , \tag{7.51}$$

a pure real quantity. This regime can be reached by increasing the intracavity power such that $|A_0|^2$, $|B_0|^2$ are large, reducing the overall lifetime but increasing the real part of τ_p relative to the imaginary part. Physically, we can say the real part determines the carrier fraction that follows in phase with the electric field, or as previously mentioned, equivalent to interband FWM. For the second case, in which $\omega_s >> 1/\tau_{sp} + 2R(|A_0|^2 + |B_0|^2)$, we obtain

$$\tau_p \approx -\frac{i}{\omega_s}\,, \tag{7.52}$$

a pure imaginary quantity. This regime is typical for an mostly empty cavity in which $|A_0|^2$, $|B_0|^2$ are small. Here, the imaginary part determines the carrier fraction that is 90 degrees out of phase with the electric field, or equivalent to intraband FWM. From our previous analytic solutions, a whether τ_p is real or imaginary affects the phases of $A_{\pm 1}$ and $B_{\pm 1}$. Looking at the solution for $A_{\pm 1}$,

$$\begin{aligned}\begin{bmatrix} A_1 \\ A_{-1}^* \end{bmatrix} =& C_1 \exp\left(\int_0^z dz' g_3 |B_0|^2\right) \begin{bmatrix} -e^{2i\psi_0^+} \\ 1 \end{bmatrix} \\ &+ C_2 \exp\left(\int_0^z dz' \left(g_3|B_0|^2 - 2g_2|A_0|^2\right)\right) \begin{bmatrix} e^{2i\psi_0^+} \\ 1 \end{bmatrix}\end{aligned}$$

if $\tau_g < 2\text{Re}(\tau_p)$, the term attached to the C_2 coefficient will exponentially die out, resulting in only a simple and constant phase relation between A_1 and A_{-1}.

Additional insight is gained by writing the phase equation explicitly by substituting $A_1 = |A_1|e^{i\psi_1}$, $A_{-1} = |A_{-1}|e^{i\psi_{-1}}$. First, for the case in which g_2 is real, we obtain

$$\frac{d|A_1|}{dz} = (g_3|B_0|^2 - g_2|A_0|^2)|A_1| - g_2|A_0|^2|A_{-1}|\cos(2\psi_0 - \psi_{-1} - \psi_1) \quad (7.53a)$$

$$\frac{d|A_{-1}|}{dz} = (g_3|B_0|^2 - g_2|A_0|^2)|A_{-1}| - g_2|A_0|^2|A_1|\cos(2\psi_0 - \psi_1 - \psi_{-1}) \quad (7.53b)$$

$$\frac{d}{dz}(\psi_1 + \psi_{-1}) = -2g_2|A_0|^2\sin(2\psi_0 - \psi_1 - \psi_{-1})\left[\frac{|A_1|^2 + |A_{-1}|^2}{|A_1||A_{-1}|}\right]. \quad (7.53c)$$

If we look carefully at the phase in Equation 7.53c, we see that the derivative goes to zero when

$$\Phi = 2\psi_0 - \psi_1 - \psi_{-1} = \pm\pi, 0\,, \quad (7.54)$$

suggesting that these values indicate phase locked states.

A stability analysis around these two points reveals that the phase equation is unstable at $\Phi = 0$, as seen by the fact that $\frac{d}{dz}(\psi_1 + \psi_{-1})$ increases when $\psi_1 + \psi_{-1}$ increases in the sine function. This solution corresponds to the phase differences all being zero between all the modes, which when summed, would result in a series of ultrashort pulses. The instability explains why it is difficult to achieve ultrashort pulses without additional sections, such as a saturable absorber. However, the value of $\Phi = \pm\pi$ is a stable solution. This value corresponds to an FM or FM-like solution in which each mode differs in phase by a finite, but fixed value. A diagram of how the modes interfere given their phase differences are shown in Figure 7.4. From this figure, it is clear that the phase state of $\Phi = \pm\pi$ is much better suited for utilizing all available gain due to gain saturations resulting from population pulsations. Therefore, the phase of the three modes naturally prefers this second state, as it provides the most gain. This is also seen mathematically from Equation 7.53a, b by plugging in $\Phi = \pm\pi$, which turns the RHS FWM term into a net gain due to $\cos(\Phi) = -1$. This phase relation can be generalized to any mode n and summed to produce an

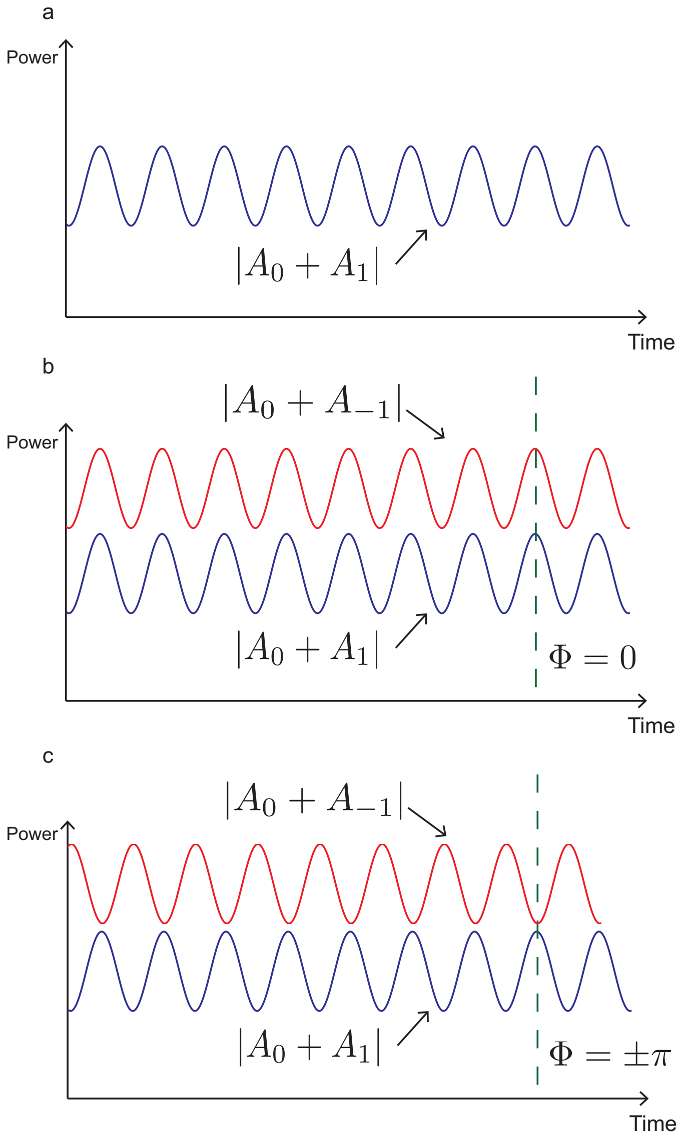

Figure 7.4: An illustration of the intensity patterns of the forward modes. a) the interference between the central mode A_0 and one of the side modes A_1 produces a sinusoidal pattern. b) The third wave's amplitude A_{-1}, interfering with A_0, produces a second sinusoidal pattern that is in phase with the first sinusoid ($\Phi = 0$). c) The second sinusoid is now offset by a phase shift of $\pm\pi$ ($\Phi = \pm\pi$)

expression for the phase ψ_n as a function of n [58]:

$$\sum_{m'=0}^{n} \sum_{m=0}^{m'} \Phi_m = \sum_{m'=0}^{n} \sum_{m=0}^{m'} (2\psi_m - \psi_{m+1} - \psi_{m-1}) \,. \tag{7.55}$$

We can do the summation by changing indices and canceling like terms

$$\sum_{m'=0}^{n}\left[2\sum_{m=0}^{m'}\psi_m-\sum_{m=0}^{m'}\psi_{m+1}-\sum_{m=0}^{m'}\psi_{m-1}\right]=\pm\sum_{m'=0}^{n}\sum_{m=0}^{m'}\pi$$
$$\sum_{m'=0}^{n}\left[2\sum_{m=0}^{m'}\psi_m-\sum_{m=0}^{m'}\psi_m+\psi_0-\psi_{m'+1}-\sum_{m=0}^{m'}\psi_m-\psi_{-1}+\psi_{m'}\right]=\pm\sum_{m'=0}^{n}m'\pi$$

We repeat this process with the second summation, again by adding or removing terms to the summations so that they cancel

$$\sum_{m'=0}^{n}(\psi_{m'}-\psi_{m'+1})=\pm\sum_{m'=0}^{n}(m'\pi+\psi_{-1}-\psi_0)$$
$$\sum_{m'=0}^{n}\psi_{m'}-\sum_{m'=0}^{n}\psi_{m'}-\psi_{n+1}+\psi_0=\pm\frac{n^2\pi}{2}+(\psi_{-1}-\psi_0)n$$

and we are able to obtain an expression for just the phase ψ_{n+1} as a function of n

$$\psi_{n+1}=\mp\frac{\pi n^2}{2}+\alpha_\psi n+\beta_\psi\,, \tag{7.56}$$

where $\alpha_\psi=\psi_0-\psi_{-1}$ and $\beta_\psi=\psi_0$ are arbitrary constants.

The phase as a function of mode number n has a clear quadratic dependence, which can then be compensated via a simple dispersive medium to produce a series of short pulses as shown already in the previous chapters. Our numerical results from the reduced model can also be compensated. The InGaAsP results are numerically phase compensated and the result, shown in Figure 7.5, is similar to that calculated in the full model (Figure 6.3).

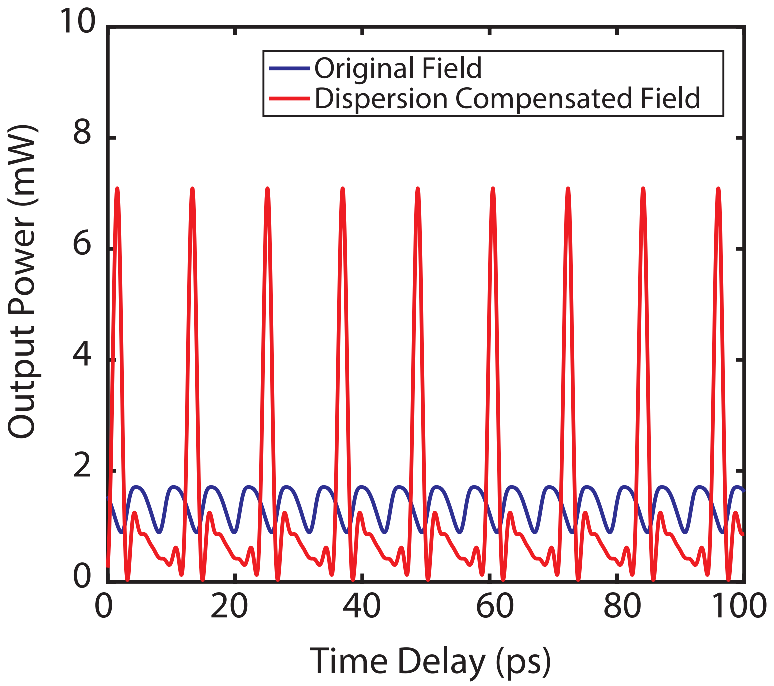

Figure 7.5: The results of InGaAsP temporal output after dispersion compensation. The spectrum from Figure 7.2b is multiplied by quadratic phase to simulate dispersion compensation via an optical fiber. The group delay dispersion (GDD) in this case is 1.15 ps^2.

Now for the second case, in which τ_p is imaginary, we obtain

$$\frac{d|A_1|}{dz} = g_3|B_0|^2|A_1| - g_2|A_0|^2|A_{-1}|\sin(2\psi_0 - \psi_{-1} - \psi_1) \tag{7.57a}$$

$$\frac{d|A_{-1}|}{dz} = g_3|B_0|^2|A_{-1}| + g_2|A_0|^2|A_1|\sin(2\psi_0 - \psi_1 - \psi_{-1}) \tag{7.57b}$$

$$\frac{d}{dz}(\psi_1 + \psi_{-1}) = g_2|A_0|^2\cos(2\psi_0 - \psi_1 - \psi_{-1})\left[\frac{|A_{-1}|^2 - |A_1|^2}{|A_1||A_{-1}|}\right]. \tag{7.57c}$$

In this form, we see that the phase derivative is much more complicated. The stability of the phase relation now depends highly upon the magnitudes, $|A_{\pm 1}|$ instead of only upon phase values. This suggests the phase relation will be much less stable, as we have the additional requirement that $|A_1| = |A_{-1}|$. Even in this state, Φ is not forced to take a specific value, so we cannot say that we have reached a stable, fixed phase relation between the three modes. Therefore, it is important that we operate with a high enough intracavity laser power so that the carriers will be in phase with the electric field for FM comb generation.

Thus, we see that the FM solution emerges as the natural phase-locked solution in the presence of interband FWM and multimode lasing. This physically makes sense in light of gain competition. The various phases of the modes will settle to where the available gain is greatest, producing a natural phase offset between the different modes. In other words, a solution in which all modes constructively add to form a train of pulses is not preferable (absent a saturable absorber) due to the inefficient use of the available gain in between pulses. Instead, the FM solution utilizes all available gain by having the modes interfere at different points in time, producing a stable, quasi-CW phase-locked state.

7.7 Conclusion

We have explored the physics of FM comb generation in QW diode lasers in some detail in this chapter. While there are many physical effects that can alter laser operation and comb generation, we have reduced it down to SHB and FWM as the two dominant and important ones. SHB allows multiple modes to achieve threshold gain due to reduced gain competition between modes, and the FWM induced by population pulsations locks the phases of the modes together. It is important that the cavity modes share the same carriers, or equivalently, are within the homogeneous gain linewidth. This allows for the fields to modulate the phase of the carriers, which in turn modulates the phases of the optical modes. Both SHB and FWM enable this effect to occur - generating a laser with multiple, mutually phase coherent modes.

In comparison to other systems, SHB is easily achieved in QD and QC lasers, proper selection of materials can also allow SHB to exist in QW systems. With the presence of both SHB and FWM, a FM comb emerges passively as a natural state of operation of these diode lasers. With this knowledge, we are now well-equipped to design, fabricate, and test some laser diodes experimentally to verify our theory.

CHAPTER VIII

Design and Fabrication of Quantum Well Laser Diodes

Now that we have a basic understanding of the physics and inner workings of generating FM combs from InGaAsP laser diodes, we move on to design, fabricate, and characterize these devices. The InP / InGaAsP semiconductor materials are processed at the University of Michigan's Lurie Nanofabrication Facility (LNF). We discuss additional laser design parameters not modeled in our theory and also go over the fabrication steps and calibrations used.

8.1 1.55 μm Laser Diode Design

On an elementary level, a semiconductor laser diode converts electric current (electrons and holes) into light by way of radiative recombination. In device design, we have to modify the electrical and optical properties of the material to achieve optimal light generation. The electrical properties are modified by properly growing semiconductor heterojunctions using binary, ternary, and sometimes quaternary materials using metal-organic chemical vapor deposition (MOCVD) or molecular beam epitaxy (MBE) [98]. There are several characteristics that must be carefully considered, such as doping levels, layer thickness, and material types. Incorporating means of trapping

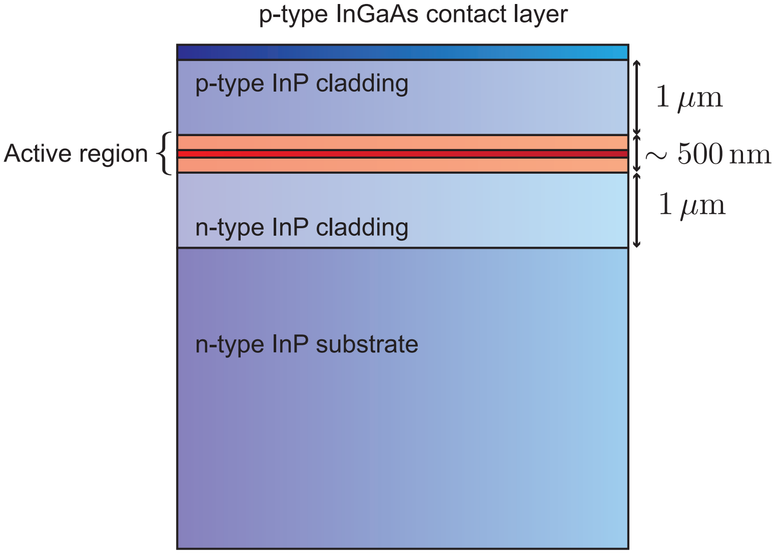

Figure 8.1: Typical layers grown on an InP substrate for a laser diode or LED.

these carriers in QWs or other nanostructures such as QDs and quantum dashes aids in the recombination efficiency. Laser diodes can also be made from bulk materials.

For our laser diode design, we start with a simple Fabry-Perot cavity made up of facet reflections with a 1.5 μm central wavelength. A typical stack of the InP based semiconductor laser is shown in Figure 8.1.

The layers grown on the substrate include a 1 μm waveguide cladding layer, an active region (also the waveguide core) in which the carriers recombine to generate light, a second cladding layer, and a highly doped top contact layer. The lower and upper layers are n-doped and p-doped respectively, forming a p-n diode that facilitates current flow with proper forward bias. As the carriers are injected, they move into the active region, become trapped in the QWs (or other structures), and radiatively recombine to generate light. The energy band diagram for this design is shown in Figure 8.2. Our active region consists of a 200 nm separate confinement heterostructure (SCH), which serves to facilitate carrier capture as well as providing a refractive index contrast between the core and the cladding. Moreover, there are four QWs, separated by 15 nm, to capture carriers and provide optical gain. This design is referred to as a multi-quantum well (MQW) structure. Having multiple QWs aids in

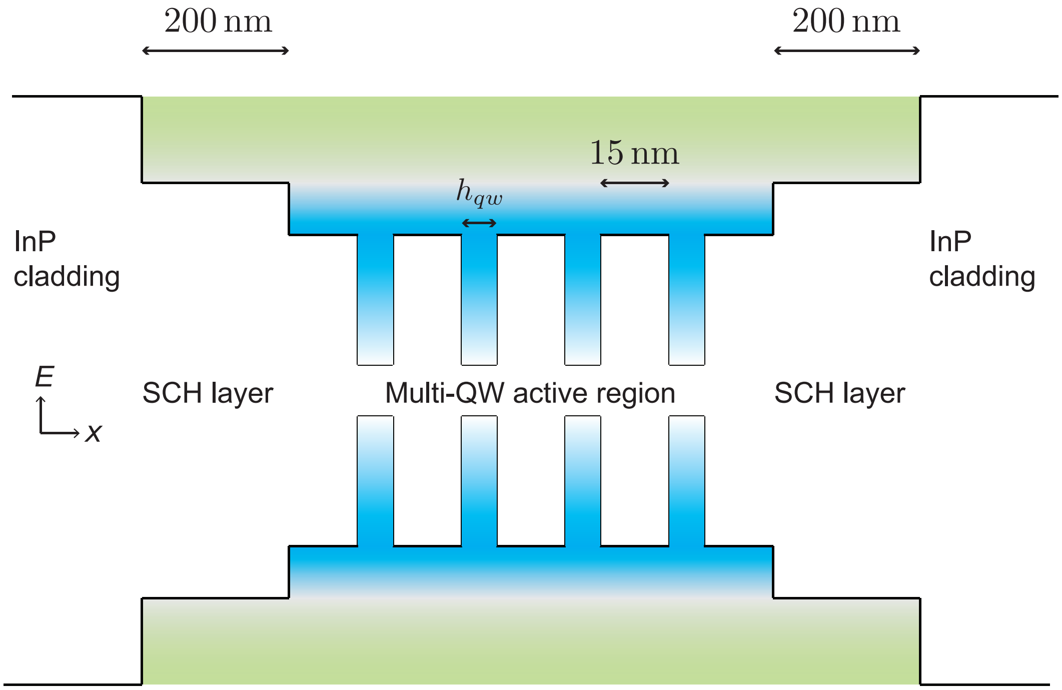

Figure 8.2: The energy band diagram of the semiconductor layers in the active region.

the capture of transported carriers through the active region and overall provides more gain, albeit at the expense of requiring more current to reach population inversion [99, 66].

The details and characteristics of each stack in our laser are shown in Table 8.1. The doping levels of each region can be varied depending on the design. We have chosen a standard doping profile in which the contact layers (substrate and InGaAs cap) are heavily doped to facilitate ohmic contacts with the deposited metal during fabrication [100], while the cladding layers are still doped but not as heavily. The smaller core regions remain undoped. The major trade-off between a lightly or heavily doped cladding and the core region is better electrical characteristics and carrier transport versus additional optical losses from free carrier absorption [101].

The quaternary product, InGaAsP, also written $\mathrm{Ga}_X\mathrm{In}_{1-X}\mathrm{As}_Y\mathrm{P}_{1-Y}$, has additional parameters X, Y that specify its bandgap, lattice constant, and strain. The SCH and barrier layers consist of 1.15Q InGaAsP (designated as such due to its

Stack layer	Thickness	Doping level	$\mathrm{Ga}_X\mathrm{In}_{1-X}\mathrm{As}_Y\mathrm{P}_{1-Y}$ fractions
n-type InP substrate	350 μ m	2×10^{18} cm^{-3}	
n-type InP cladding	1 μ m	5×10^{17} cm^{-3}	
1.15Q InGaAsP SCH layer	200 nm	undoped	$X = 0.1712$, $Y = 0.3737$
1.15Q InGaAsP barrier, 5x	15 nm	undoped	
InGaAsP QW, 4x	8 nm	undoped	$X = 0.2034$, $Y = 0.7475$
p-type InP cladding	1 μ m	5×10^{17} cm^{-3}	
p-type InGaAs top contact	100 nm	2×10^{19} cm^{-3}	

Table 8.1: Semiconductor layer thicknesses and doping levels for a 1.5 μm Fabry-Perot laser diode and quaternary fractions for the InGaAsP layers. The QW fractions are designed for a +1% compressive strain.

bandgap being 1.15 μm) while the QW InGaAsP is designed to emit photons around 1.55 μm and are compressively strained. The compressive strain offers advantages of higher gain and better efficiency due to the separation and decoupling of the heavy-hole (HH) band from the light-hole (LH) band, reducing distortion and lowering effective mass of the heavy holes [102]. The specific values of X and Y are also listed in Table 8.1.

However, the design is not yet complete, as the generated light must also be confined in a laser cavity. While the confinement in the vertical direction is accomplished by index guiding due to the index contrast between the core and the cladding areas, we need to provide confinement in the horizontal direction. This is accomplished by using a ridge waveguide structure etched into the wafer, as seen in Figure 8.3a.

The ridge waveguide provides the needed lateral confinement via the index difference between the semiconductor ridge and its surroundings. We can control the ridge width, tailoring it for single transverse mode or multimode operation. Because our goal is to phase lock longitudinal cavity modes in our laser diode, we design the ridge for the single mode operation. Therefore, we narrow the ridge to a width of 2 μm and etch through the cladding to right before the active (core) region. The transverse electric field profile of this waveguide mode is calculated using finite element methods (COMSOL Multiphysics). Using modal analysis in the optics module, we define

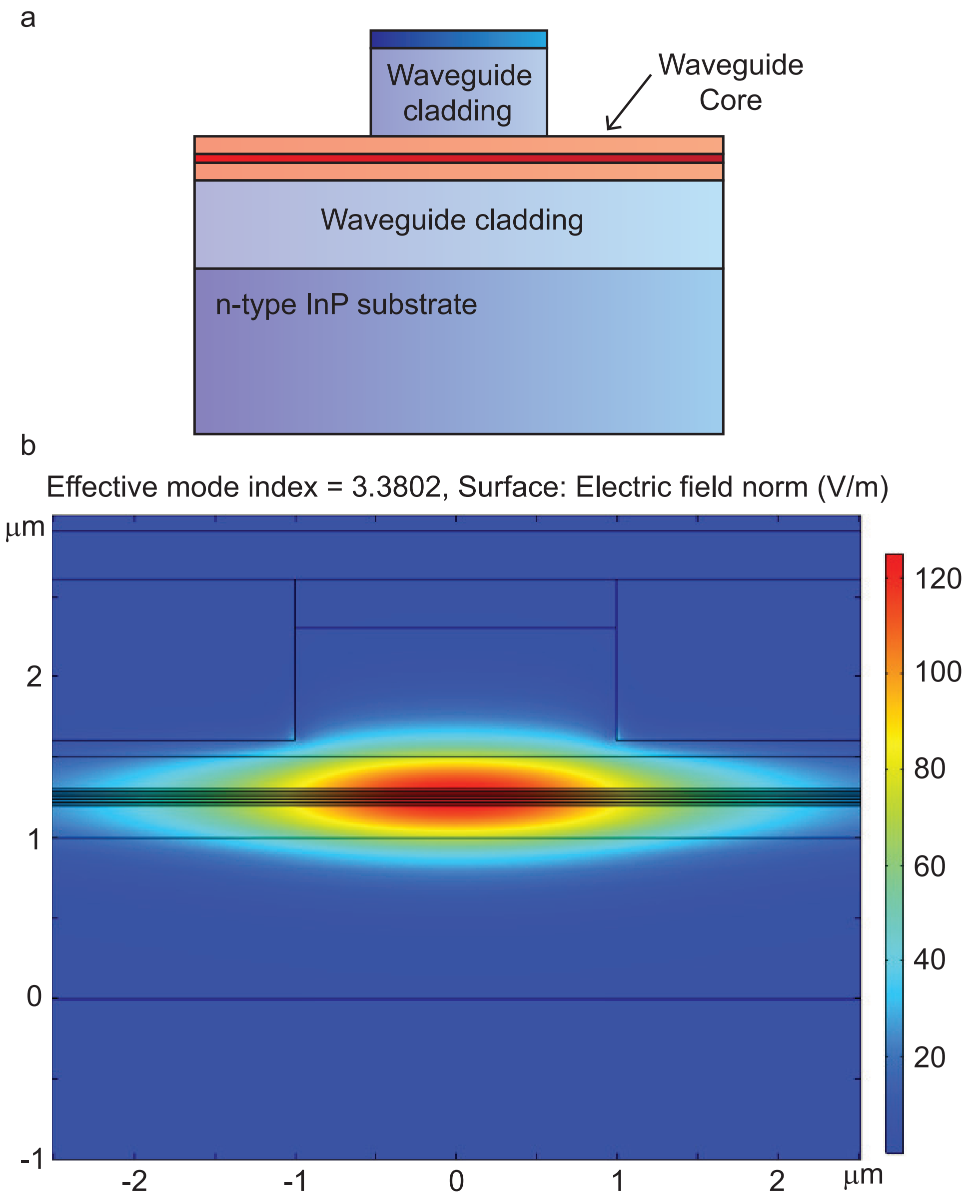

Figure 8.3: a) a diagram of our etched wafer, forming a ridge waveguide with the core and cladding labeled. b) A finite element calculation of the transverse waveguide mode of our laser.

approximate refractive indices for the materials in our structure and find the mode shape, frequency, and effective group index. The result is plotted in Figure 8.3b.

Stack layer	Thickness	Doping level	$Ga_XIn_{1-X}As_YP_{1-Y}$ fractions
1.15Q InGaAsP SCH layer	200 nm	undoped	$X = 0.1712$, $Y = 0.3737$
1.15Q InGaAsP barrier, 5x	15 nm	undoped	
InGaAsP QW, 4x	8 nm	undoped	$X = 0.0808$, $Y = 0.4848$

Table 8.2: Semiconductor layer thicknesses and doping levels for a 1.3 μm Fabry-Perot laser diode and quaternary fractions for the InGaAsP layers. Once more, the QW fractions are designed for a +1% compressive strain.

8.2 1.3 μm and 1.55 μm Asymmetric QW Laser Diode Design

Going beyond the standard 1.55 μm design, we have two additional designs to test. From our theoretical studies, the SHB and FWM effects should still be prevalent at some lower wavelengths such as 1.3 μm, a wavelength of interest due to its close to zero dispersion in optical fibers. The design parameters of the 1.3 μm laser are identical to the aforementioned 1.55 μm laser, albeit with changes to the gain region so the QW energy is adjusted to the shorter wavelength. The parameters for this active region of this design are shown in Table 8.2.

The third design, however, is a bit more complex. The idea is to expand the bandwidth of our comb by expanding the gain bandwidth by incorporating asymmetric QWs with different emission wavelengths, essentially expanding the inhomogeneous broadening of the system. This can be easily done by adjusting the widths of the QWs. However, it is not a simple matter of just growing any asymmetric QWs - we still must ensure that the optical modes can share some carriers in either QW. As mentioned in chapter VII, the frequency separation between the QWs should not be more than the homogeneous linewidth of the gain, thus satisfying the above criteria. A calculation of the asymmetric QW system based off of our reduced equations is shown in Figure 8.4. It is clear from the figure that, if the confined energy separation between the two QWs is much larger than the homogeneous linewidth, the temporal output is not periodic, indicating a lack of phase locking. As the separation is reduced to where there is good overlap via the homogeneous linewidth, the temporal

Stack layer	Thickness	Doping level	$\text{Ga}_X\text{In}_{1-X}\text{As}_Y\text{P}_{1-Y}$ fractions
1.15Q InGaAsP SCH layer	200 nm	undoped	$X = 0.1712$, $Y = 0.3737$
1.15Q InGaAsP barrier, 5x	15 nm	undoped	
InGaAsP QW, 2x	8 nm	undoped	$X = 0.2034$, $Y = 0.7475$
InGaAsP QW, 2x	7 nm	undoped	$X = 0.2034$, $Y = 0.7475$

Table 8.3: Semiconductor layer thicknesses and doping levels for the asymmetric 1.55 μm Fabry-Perot laser diode and quaternary fractions for the InGaAsP layers. Like the previous two designs, the QW fractions are designed for a +1% compressive strain.

output becomes more regular until it reaches a phase locked state similar to what we calculated in the previous chapters. Thus the principle in our third design is to have slightly different QW confined energies - enough to expand the bandwidth but not separated larger than the homogeneous linewidth. The result is a comb that should be broader than just a single QW while still maintaining phase coherence between the modes. The active region parameters for this design are shown in Table 8.3. Here, we have two QWs of 8 nm and two QWs of 7 nm for the asymmetric design for a total of four QWs.

8.3 Laser Fabrication

With the design ready, we move on to manufacturing and fabrication of our lasers. During the work of this dissertation, the University of Michigan's LNF did not have semiconductor growth capabilities, so we ordered InP / InGaAsP material from an external foundry (Xiamen Powerway Advanced Material Co. LTD). The semiconductor layer stack was grown to our specifications as shown in Table 8.1.

We outline the fabrication steps and details as follows. First, we need to etch through the InGaAs top layer and InP cladding layers. The following steps follow the illustration shown in Figure 8.5 for the ridge fabrication.

1. We cleave the 2 inch wafers into smaller pieces, about 1.0 cm × 1.0 cm.

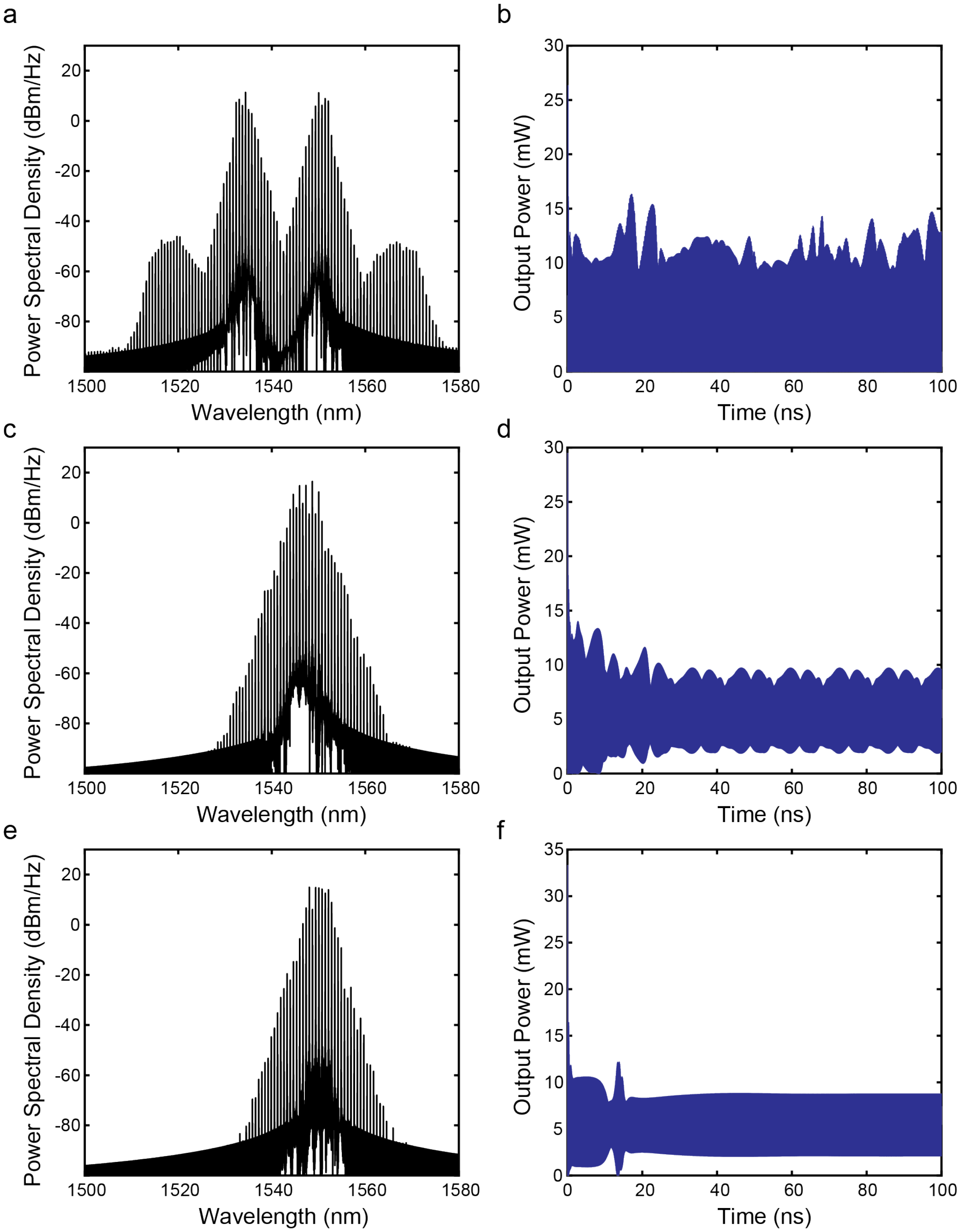

Figure 8.4: A simulation of 2 asymmetric QWs using our reduced model described in chapter VII. The homogeneous half linewidth Γ for all simulations is 6 meV. a) Spectrum and b) temporal output of two QWs with a confined energy separation of 10 meV. c) Spectrum and d) temporal output of two QWs with a confined energy separation of 5 meV. e) Spectrum and f) temporal output of two QWs with a confined energy separation of 2 meV.

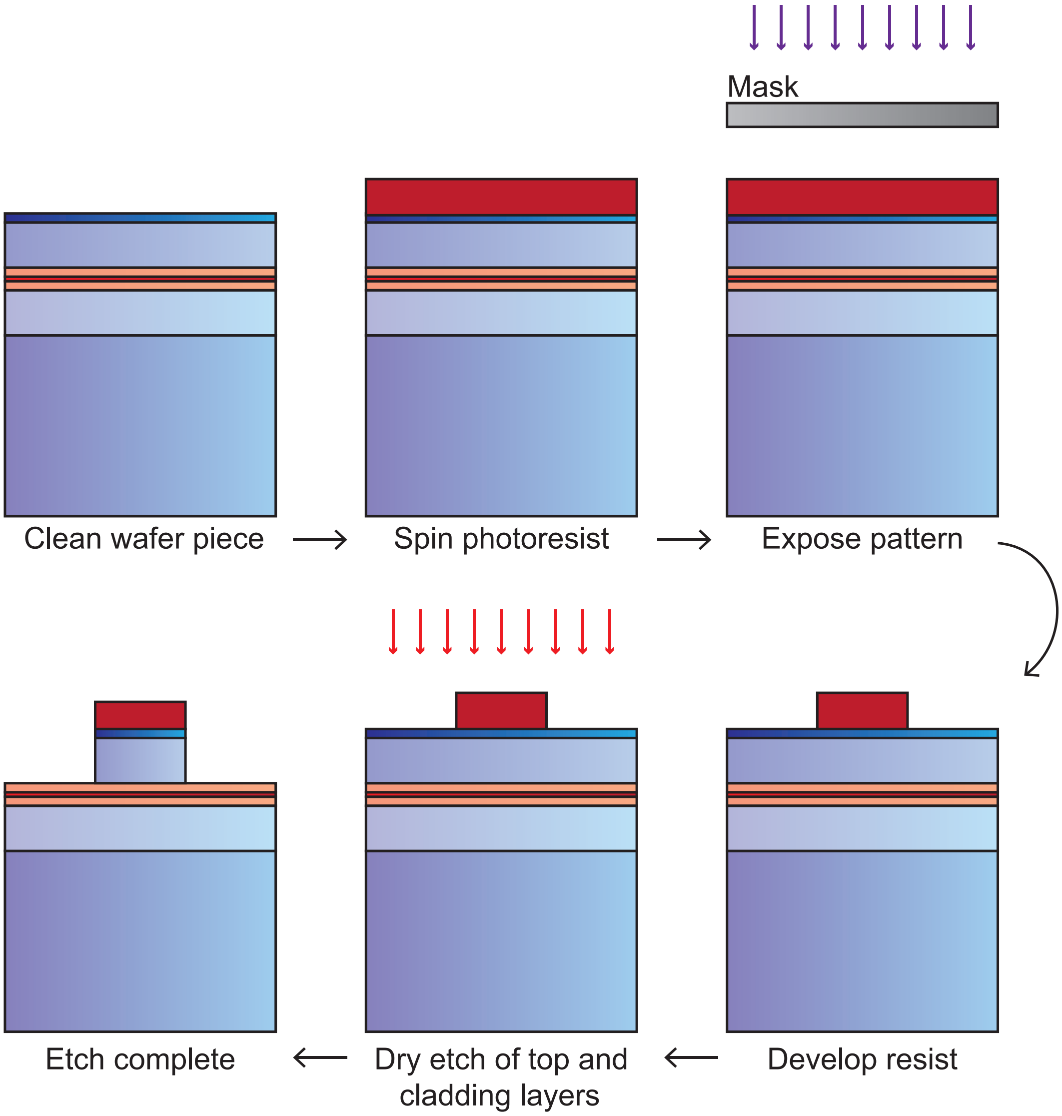

Figure 8.5: An illustration of the InP etching fabrication process as described in this section. Note that the layer thicknesses are not to scale.

2. Pieces are cleaned and primed with HMDS using recipe 1 in the YES Oven (YES-310TA E).
3. Photoresist (SPR 220 3.0) is spun at 3000 RPM and baked for 90 seconds at 115 C. This gives about a 3 μm layer of photoresist.
4. Pieces are exposed using the GCA AS200 AutoStep for 0.3 seconds and baked again for 90 seconds at 115 C (see appendix for details of this exposure).

5. Samples are developed using the CEE Developer tool with AZ 726 and recipe DP 60-60.
6. We perform a dry etch of the cladding layers using the Oxford ICP RIE for 10 minutes. Details of the recipe are in the appendix.

However, we need to fabricate some insulation and passivation layers to protect the edges of the ridge from any unwanted current or applied potentials. Thus we use silicon dioxide for passivation and to aid in planarization of our surface. These additional steps are outlined below and follow the illustration shown in Figure 8.6.

1. We deposit about 800 nm of silicon oxide via physical vapor deposition (PVD) using the AE Evaporator.
2. Samples are soaked for 24-48 hours in Remover PG to dissolve the photoresist, prepping for lift-off.
3. In a heated ultrasonic bath, samples are agitated for 1 hour to complete the oxide lift-off process.
4. Once more, samples are primed with HMDS, spun with SPR 220 3.0 at 2000 RPM, and baked for 90 seconds at 115 C.
5. Pieces are exposed using the GCA AS200 AutoStep for 0.32 seconds and baked again for 90 seconds at 115 C (see appendix for details of this second exposure).
6. Samples are developed using the CEE Developer tool with AZ 726 and recipe DP 60-60.
7. A 100 Å / 3000 Å Titanium / Gold layer is deposited via the AE Evaporator as the top metal contact.
8. Samples are soaked in Remover PG again and sonicated to lift-off the gold.

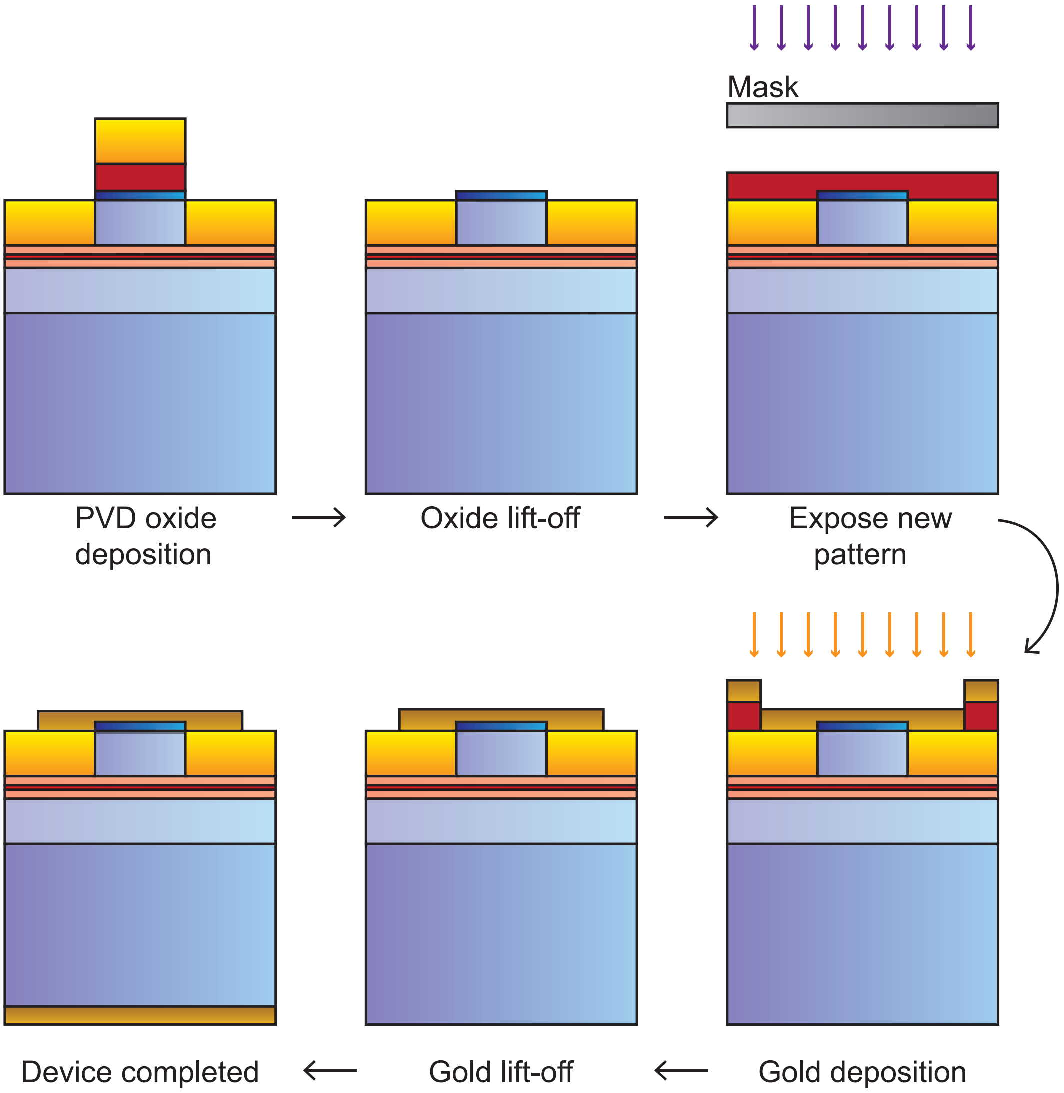

Figure 8.6: An illustration of the silicon oxide passivation and planarization fabrication process is shown. Note that the layer thicknesses are not to scale.

9. A 100 Å / 2000 Å Titanium / Gold layer is deposited on the underside of the substrate to complete the bottom metal contacts.
10. Lastly, the pieces are hand-cleaved into laser bars ranging from 1 mm - 2 mm long.

Alternatively, we could simply strip the photoresist after the InP etching, then deposit silicon oxide using PECVD on the Plasmatherm 790 via the recipe L_OX350 (41 nm / min) for 20 minutes. The difficulty with this approach is that we now have

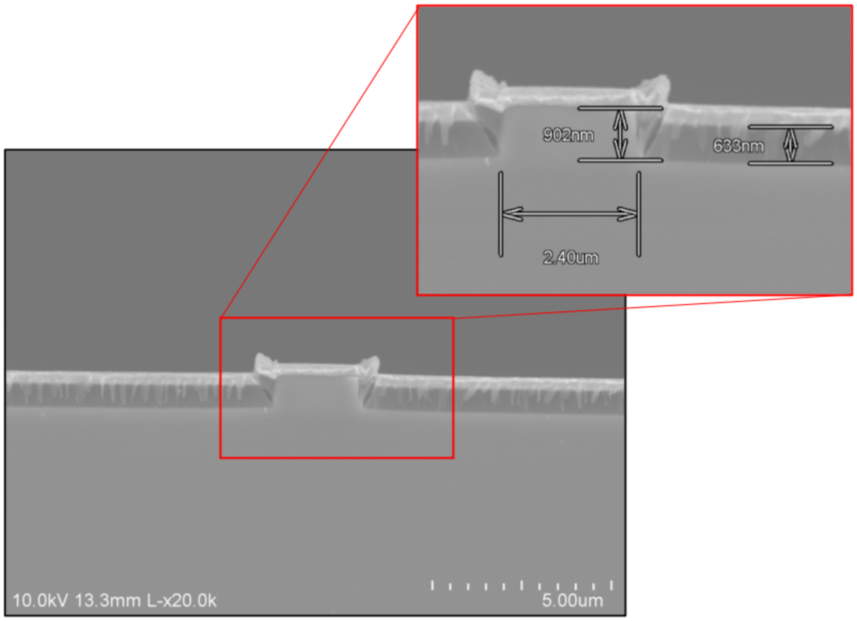

Figure 8.7: An SEM of a cleaved facet of the ridge laser. The oxide and gold layers can be identified by the darker and lighter films respectively around and on top of the ridge.

to etch away the top oxide in order to expose the InGaAs contact. Moreover, the HF wet etchants we have on hand are too imprecise for such a task, so we opted for the lift-off process as described above.

Once the lasers are cleaved, care is taken not to damage or dirty the edge facets to maintain good facet reflectivity. An SEM of the completed ridge device is shown in Figure 8.7.

8.4 Conclusion

To summarize this chapter, we have designed three distinct lasers by changing the semiconductor compositions of the QW layers. The laser designs consist of four identical QWs emitting at 1550 nm, an asymmetric design at 1550 nm to expand the bandwidth of the laser, and a 1310 nm laser. We fabricated ridge waveguides using standard lithography techniques, reactive ion etching, and metallization. We finish the devices with cleaved facets that form the Fabry-Perot cavities. Their performance, spectrum, and coherence will be discussed in detail in the following chapter.

CHAPTER IX

Characterization of Frequency Combs Generated from Quantum Well Laser Diodes

With the design and fabrication process complete, we proceed to make measurements of the optical spectrum and coherence of our laser diodes. Because of the large frequency spacing of our laser cavities, we expect to be able to resolve our frequency combs using a high resolution optical spectrum analyzer. However, the downside with a high repetition rate is that we also require the use of fast electronics in order to perform electrical measurements. Fortunately, we have such equipment on hand which greatly simplifies the experimental setups.

The organization of this chapter is two-fold. The first major section consists of optical spectra and LI curves of our three laser designs, while the second section details the RF and coherence measurements. For convenience, we designate our three laser designs as follows:

1. The 1.55 μm laser with four identical QWs is designated as structure 1 (S1);
2. The 1.55 μm laser with the asymmetric QWs is designated as structure 2 (S2);
3. The 1.3 μm QW laser is designated as structure 3 (S3).

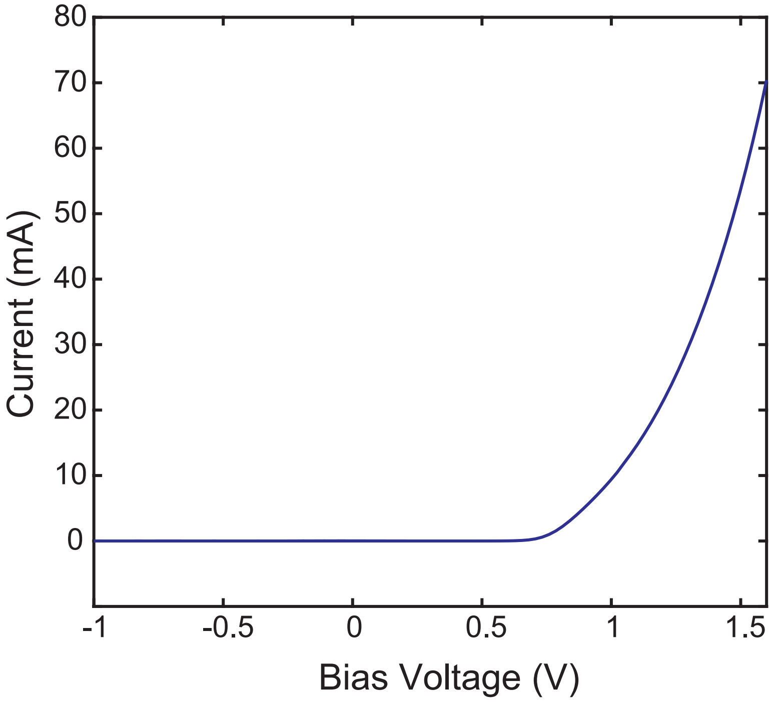

Figure 9.1: A typical IV curve of our laser diodes.

9.1 Characterization of the 1.55 μm Laser

Our experimental setup to perform the characterization measurements is fairly simple. Our hand-cleaved lasers are mounted on a conductive brass sheet on top of a thermoelectric cooler (TEC), which rests on a micrometer stage. Aluminum clamps (held down to the brass sheet with plastic screws) help secure the small laser piece so it has good contact with the brass on the underside of the chip. A second clamp also secures a thermistor that has contact to the chip in order to monitor the temperature. An electric probe on an adjustable stage is brought down on top of the laser to complete the electrical contacts. The mounting and alignment of the electrical probe is done under a monocular microscope (AM Scope) attached to a digital camera which is fed to the computer. The diode can now be forward or reverse biased, with a typical IV curve shown in Figure 9.1. Laser injection current and the TEC are both controlled by a commercial laser diode and temperature controller (Thorlabs ITC4001).

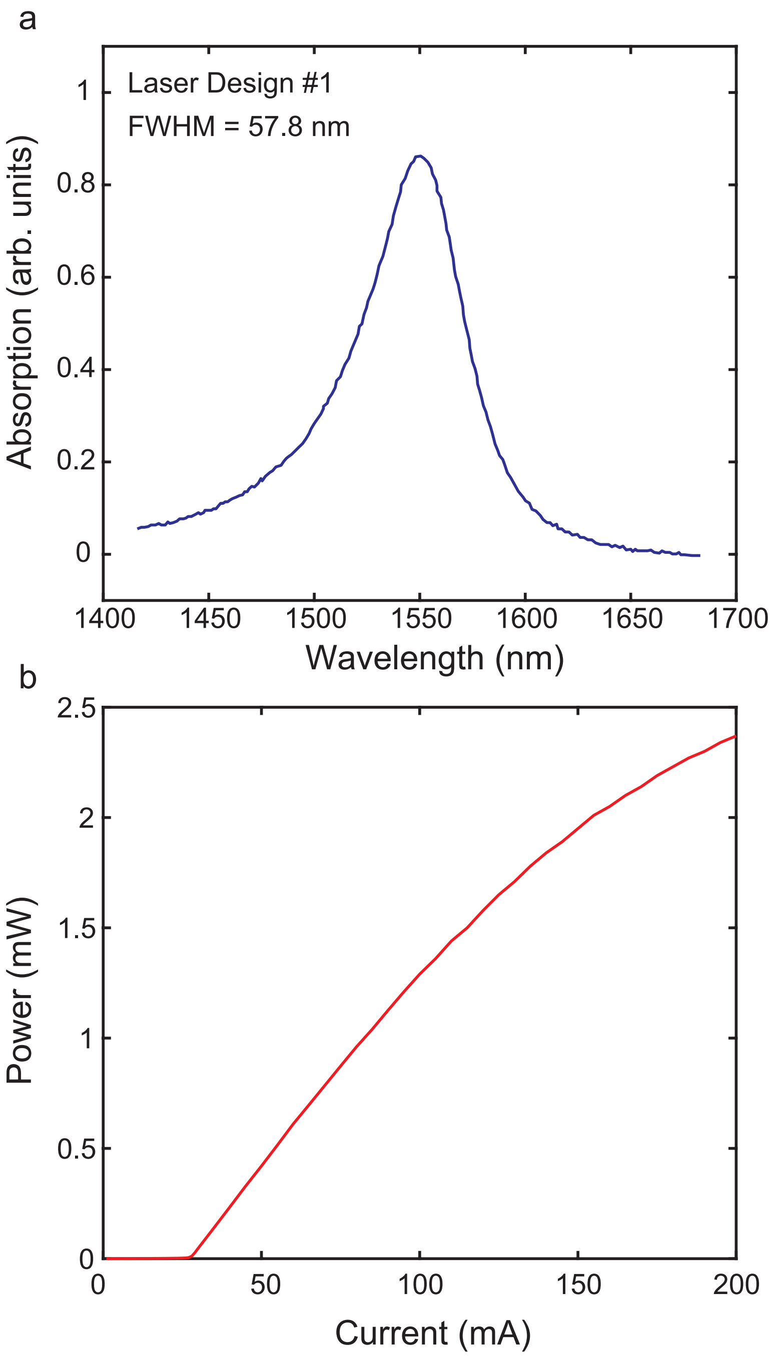

Figure 9.2: a) absorption spectrum of the QWs for the 1.55 μm laser, or S1 (absorption data courtesy of Xiamen Powerway) b) a typical LI curve of our S1 fabricated laser diodes.

The absorption spectrum of the first laser design, S1, is shown in Figure 9.2a, showing a peak around 1550 nm. We measure the LI curve with a broad area IR power head that does not require a precise alignment and plot the LI curve in Figure

9.2b. The shape is of a conventional laser, reaching threshold around 30 mA with a power output of several mW. While this amount of power is certainly usable, it is lower than what has been previously reported. This is due to several factors: first, our power head for measurement is likely not capturing all the power from the laser, as we could not get it right next to the edge of the laser due to spatial and stage constraints. Second, our manufacturing process could be improved to reduce the intracavity losses by having more robust passivation layers, such as the polymer Benzocyclobutene (BCB). Lastly, the epitaxial semiconductor structures could be modified, either slightly reducing the doping level in the cladding to reduce free carrier absorption or increasing the size of the upper InP cladding to further separate the gold contacts from the optical mode. All these changes could help increase the available laser power.

In order to further characterize the laser, we need to couple the light out from the chip. For this purpose, we use a Corning SMF-28 tapered fiber with an AR coating on the tip. The tapered fiber is mounted on a fiber holder on top of another micron stage. The fiber can be easily aligned under the microscope in the plane of the laser waveguide, then adjusted vertically until the coupled power is maximized. We observe a fairly good coupling efficiency of 50% - 60%. The fiber is then fed into an optical spectrum analyzer or a photodiode for additional measurements.

9.1.1 Cavity Length vs Optical Spectrum

We direct the light from the laser diode coupled through the fiber into our optical spectrum analyzer (Ando AQ6315E) and observe the spectrum at practical laser powers (>2 mW). We measured the spectra of two lasers at significantly different cavity lengths, with the results shown in Figure 9.3. It is clear that the comb spacing or FSR can be widely adjusted just by changing the cavity length. Because many of these lasers can be made on a single chip, simply cleaving them at different lengths

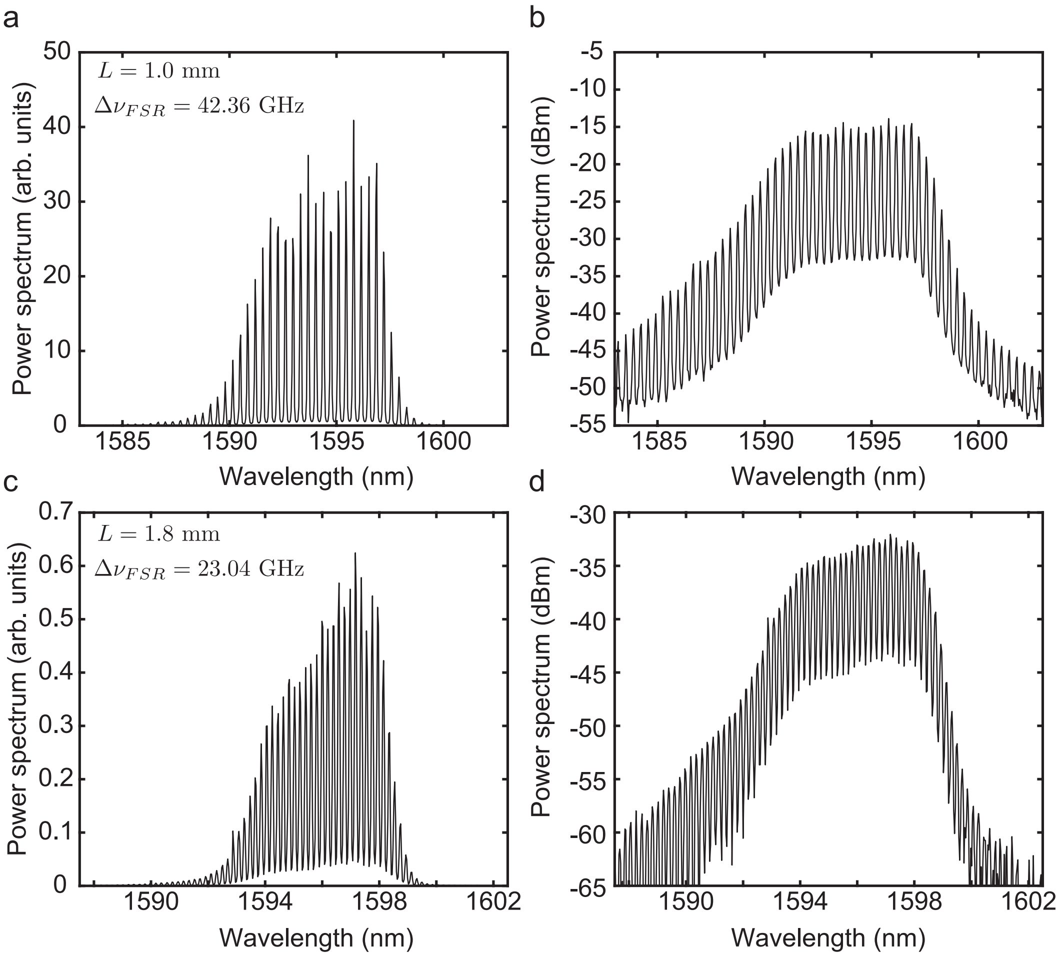

Figure 9.3: Measured optical spectra of an S1 laser diode at two different lengths. a) linear and b) log scale optical spectra of a length 1.0 mm laser diode at a pump current of $I = 190$ mA. A comb structure spanning several nm bandwidth is seen, with an FSR of 42.36 GHz. c) linear and b) log scale optical spectra of a length 1.8 mm laser diode at a pump current of $I = 185$ mA. A similar comb structure is found, although this time with a much lower FSR of 23.04 GHz.

provides quick access to frequency combs of different repetition rates. The bandwidth of the laser diodes is about 6 - 8 nm and consists of fairly flat comb lines.

An interesting pattern is that the shorter lasers, with larger FSR, typically have larger bandwidths than the longer lasers with smaller FSR. While the number of combs lines in the longer lasers is usually larger - 32 lines at -10 dB for the longer laser in Figure 9.3c compared to 24 comb lines at -10 dB for the shorter laser in Figure 9.3a - this does not entirely compensate for the reduced comb spacing and thus the overall bandwidth is smaller. We would expect the gain bandwidth to be similar across both the shorter and longer lasers, but we note that both short and long cavity lasers in Figure 9.3 are at similar pump currents. The longer cavity laser in this case would have reduced current density compared to the short cavity laser, which, according to our previously mentioned theoretical models, would reduce the effective pump rate for higher energy carriers and reducing the overall gain bandwidth.

Overall, our measured spectra is an accurate representation of the spectra from previous work in quantum wells [54, 55] as well as bearing much similarity to our calculations from our theoretical models in Chapter VI.

9.1.2 Pump Current and Temperature vs Optical Spectrum

According to our theoretical model, the frequency comb should broaden as the input pump current is increased due to the increasing gain bandwidth. This increase stems primarily from a larger number of higher energy carriers being injected into the cavity, thus broadening the available gain on the higher frequency side of the comb. Figure 9.4 confirms the effect of this broadening as the pump current is increased from 80 mA to 150 mA, with the shape of the spectra tilting toward the shorter frequency side indicating the gain due to higher energy carriers. However, the measured spectra also exhibit an overall red shift to longer wavelength that is significant (30 - 40 nm from the absorption line center). This shift is likely due to the temperature narrowing of the bandgap [103], an effect not included in our theoretical model.

We can try to reduce the temperature by tuning the TEC current and therefore reduce the red shift of the comb lines. Figure 9.5 shows measured spectra of this temperature tuning at an injection current of $I = 65$ mA. The current for this measurement is kept low as to not heat the chip up too much. As the TEC temperature set point is reduced from room temperature 22 C down to 16 C, the spectrum is blue shifted by about 5 nm. However, this does not work well at higher injection currents

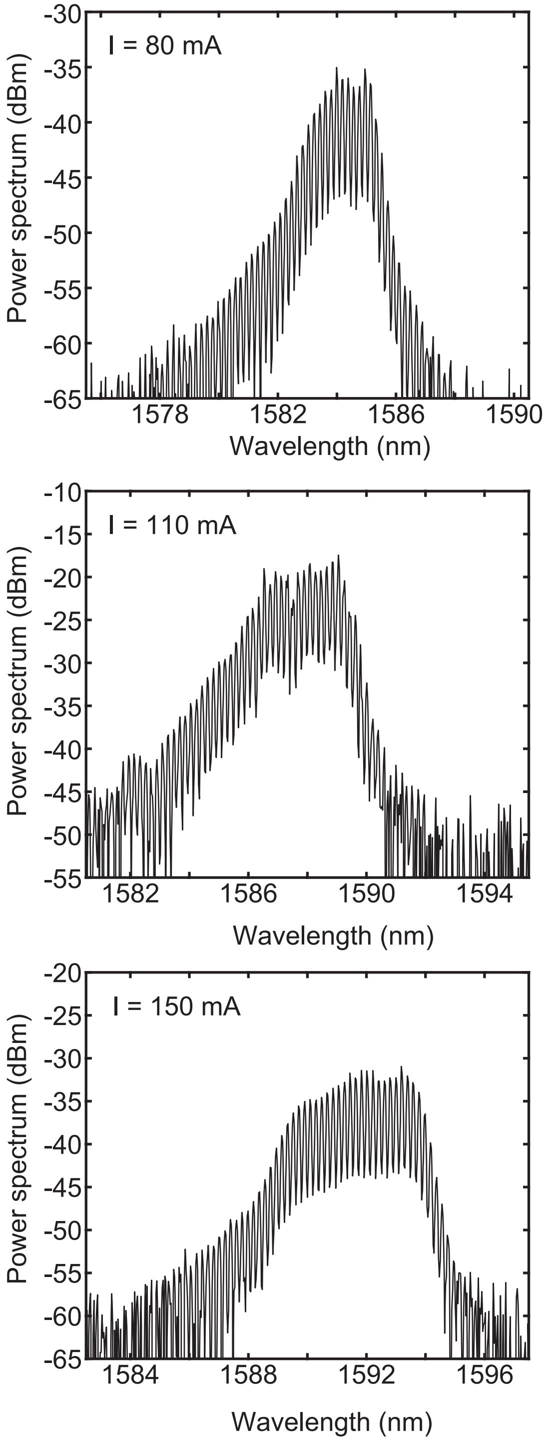

Figure 9.4: Measured optical spectra of an S1 laser diode at various pump currents. As the pump is increased, with I = 80 mA, I = 110 mA, and I = 150 mA shown, the spectra broadens significantly and also red shifts to longer wavelengths.

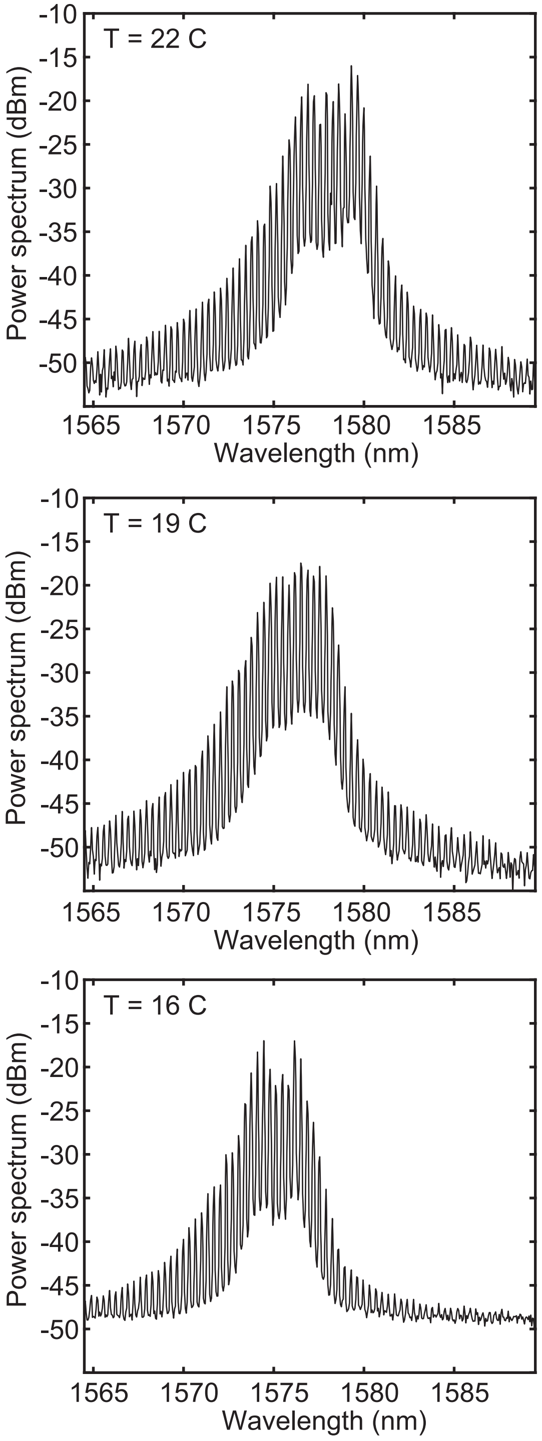

Figure 9.5: Measured optical spectra of an S1 laser diode at a fixed pump of $I = 65$ mA while adjusting the TEC temperature set point. The laser chip can be cooled, as shown in the T = 22 C, T = 19 C, and T = 16 C spectra. The wavelength is blue shifted with the cooling of the laser.

as the heating becomes too significant and our TEC cannot cool past its maximum current rating. Thus some carrier induced heating is inevitable as larger currents are driven through the diode, despite our efforts to control the temperature via the TEC. As a compromise, we occasionally turn off the laser diode and let it cool before resuming measurements. In terms of designing a laser for a specific wavelength, it is a good idea to blue shift the QW transition at the band edge to compensate for the temperature effect.

While we have not tested lasers at currents much larger than 200 mA due to the aforementioned heating effects and the fact that the diodes tend to break at high injection currents, we expect our results can be improved with additional engineering. The TEC setup, stage heat sink, and thermistor placement relative to the active laser diode could all be improved to help manage the temperature. Moreover, all our measurements are done with a DC current without any modulation. Having long, pulsed current injections will still resemble DC current but simultaneously reduce overall heating.

9.2 Characterization of the Asymmetric 1.55 μm Laser

The second design, S2, is an effort to expand the gain bandwidth through asymmetric QWs which should result in more comb lines. By artificially building more inhomogeneous broadening, the overall gain bandwidth has increased a significant 15 nm with only two types of QWs, as seen in Figure 9.6a. The absorption profile is still a single peak, which is important as the optical cavity modes need to overlap in the homogeneous linewidth for proper four-wave mixing. Because we have added a thinner, 7 nm QW, the overall absorption spectra is blue shifted as we would expect due to the higher energy electrons confined in these QWs.

The experimental setup for design S2 is the same as that of the first design. A typical LI curve is shown in Figure 9.6b, which, similar to the output of the first

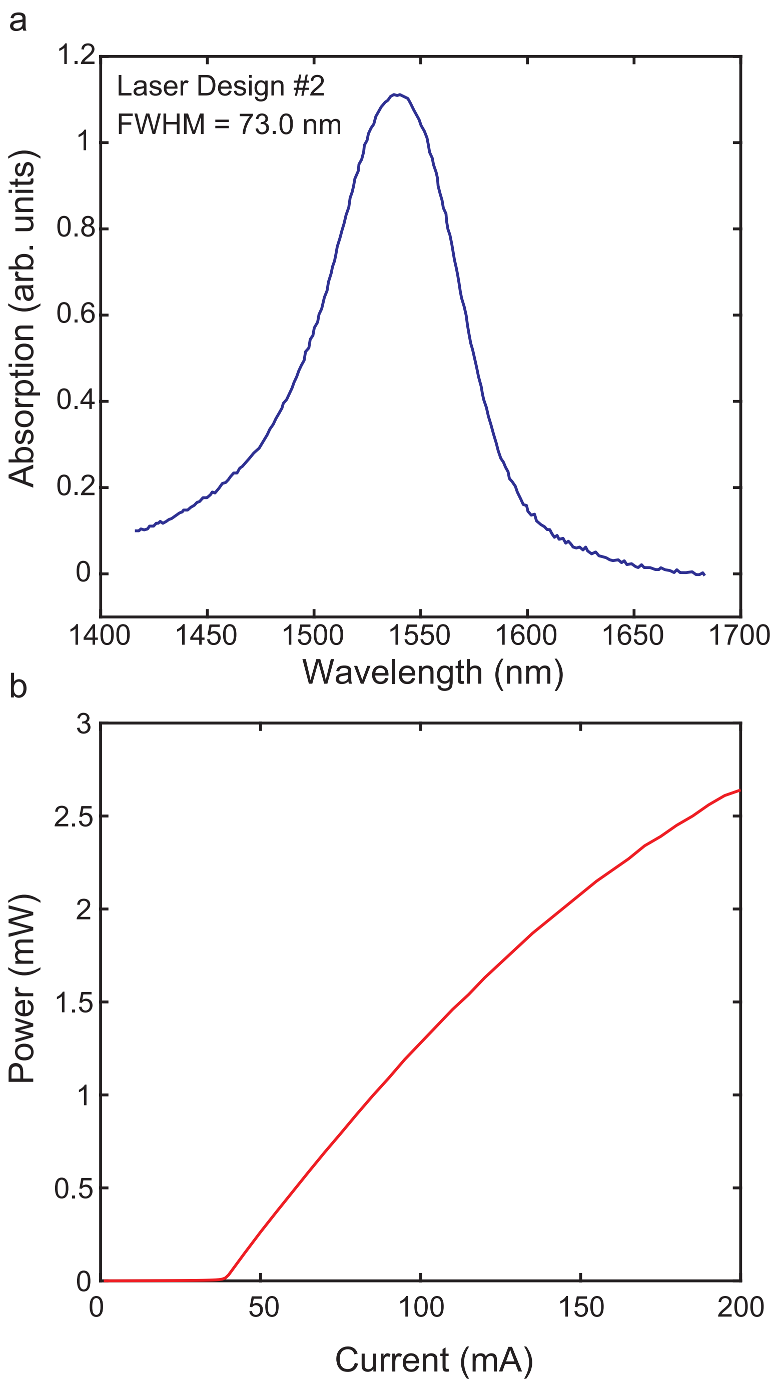

Figure 9.6: a) absorption spectrum of the QWs for the asymmetric QW design at 1.55 μm, or S2 (absorption data courtesy of Xiamen Powerway). The bandwidth is significantly broader than the S1 design (Figure 9.2a) due to the asymmetric QW design. b) a typical LI curve of our S2 fabricated laser diodes.

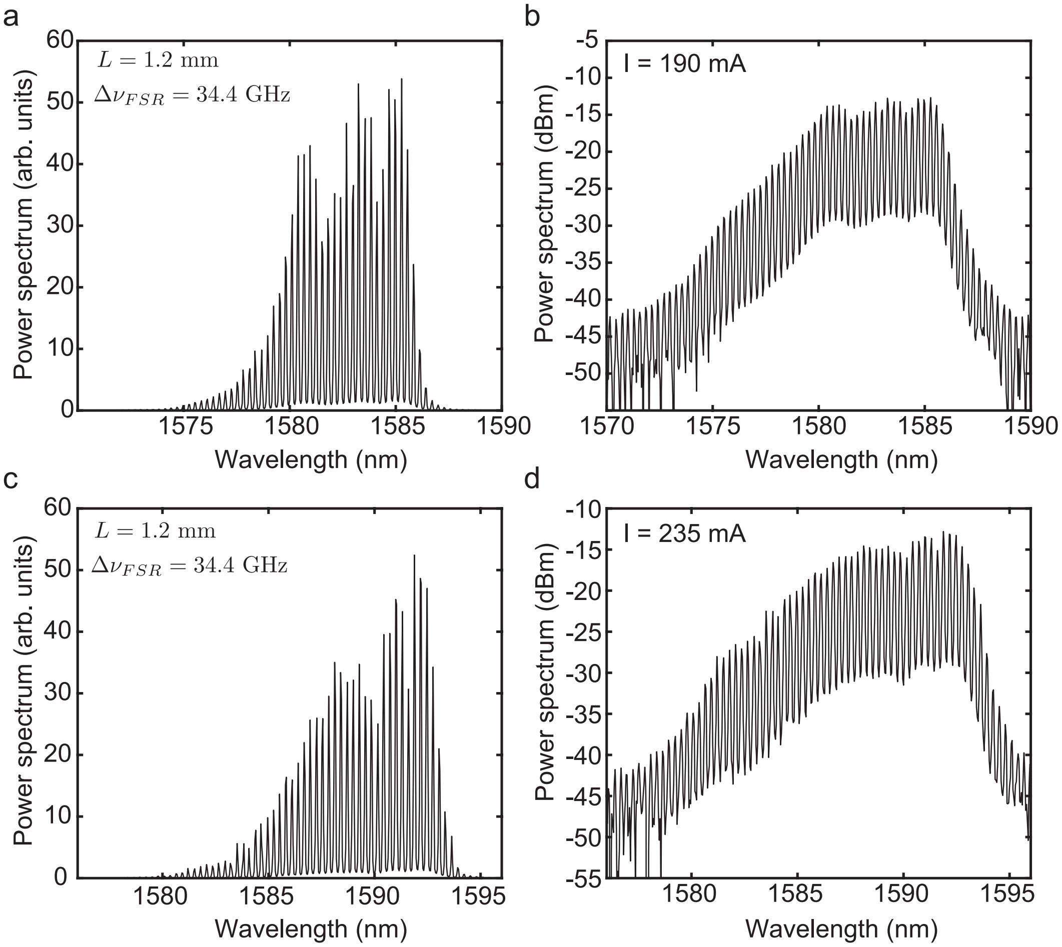

Figure 9.7: Measured optical spectrum of an S2 laser diode. a) linear and b) log scale plot of the optical spectrum at pump current $I = 190$ mA of a length 1.2 mm laser diode, corresponding to an FSR of 34.4 GHz. c) linear and d) log scale plot of the optical spectrum of the same laser at pump current $I = 235$ mA. The modes on the shorter wavelength side are lasing relatively stronger.

design, shows a power of a few mW.

All of the length, temperature, and injection current behaviors studied in the previous section also apply to our asymmetric QW laser. A typical spectrum is shown in Figure 9.7. The laser diode in this case has a cavity length of 1.2 mm, corresponding to a mode spacing of 34.4 GHz. The bandwidth of the comb has increased relative to Figure 9.3ab, a design S1 laser of similar length. In particular, the log spectra (Figure 9.7b, d) show a bump on the shorter wavelength side that is

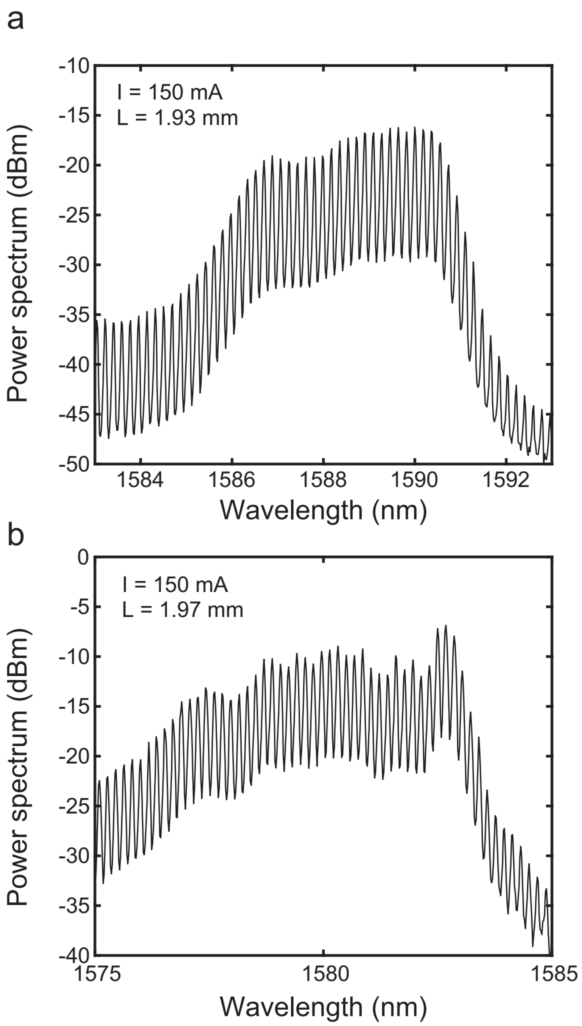

Figure 9.8: The spectrum of an approximately 2 mm length laser diode at similar pump currents for a) design S1 with the four identical QWs and b) design S2 with the asymmetric QWs. The asymmetric design has a broader spectrum.

not present in the S1 lasers, indicating that the higher energy carriers are filling up the narrow, 7 nm QW. This allows more modes to expand into the higher frequencies, expanding our bandwidth. At an input current of 235 mA, the -10 dB bandwidth is about 1.2 THz.

A more direct comparison of lasers of similar length and similar injection current is shown in Figures 9.8 and 9.9. We can see more clearly that the S2 laser design is superior in terms of bandwidth, particularly on the shorter wavelength side. In both

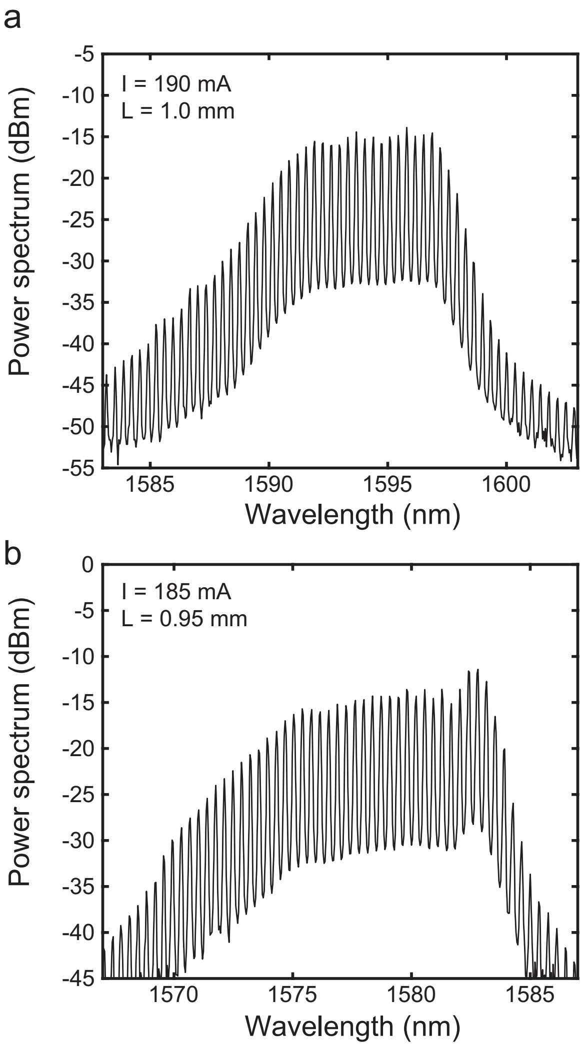

Figure 9.9: The spectrum of an approximately 1 mm length laser diode at similar pump currents for a) design S1 with the four identical QWs and b) design S2 with the asymmetric QWs. Again, the asymmetric design's spectrum is broader.

the long laser (about 2 mm) and short laser (about 1 mm) the spectrum of the asymmetric QW laser is broader. We expect that with better temperature management, we should be able to push the bandwidth even further into the higher frequency side with higher injection current. For future experiments, it is likely we can cascade more than just two widths of QWs, but three or four to expand the number of frequency comb lines.

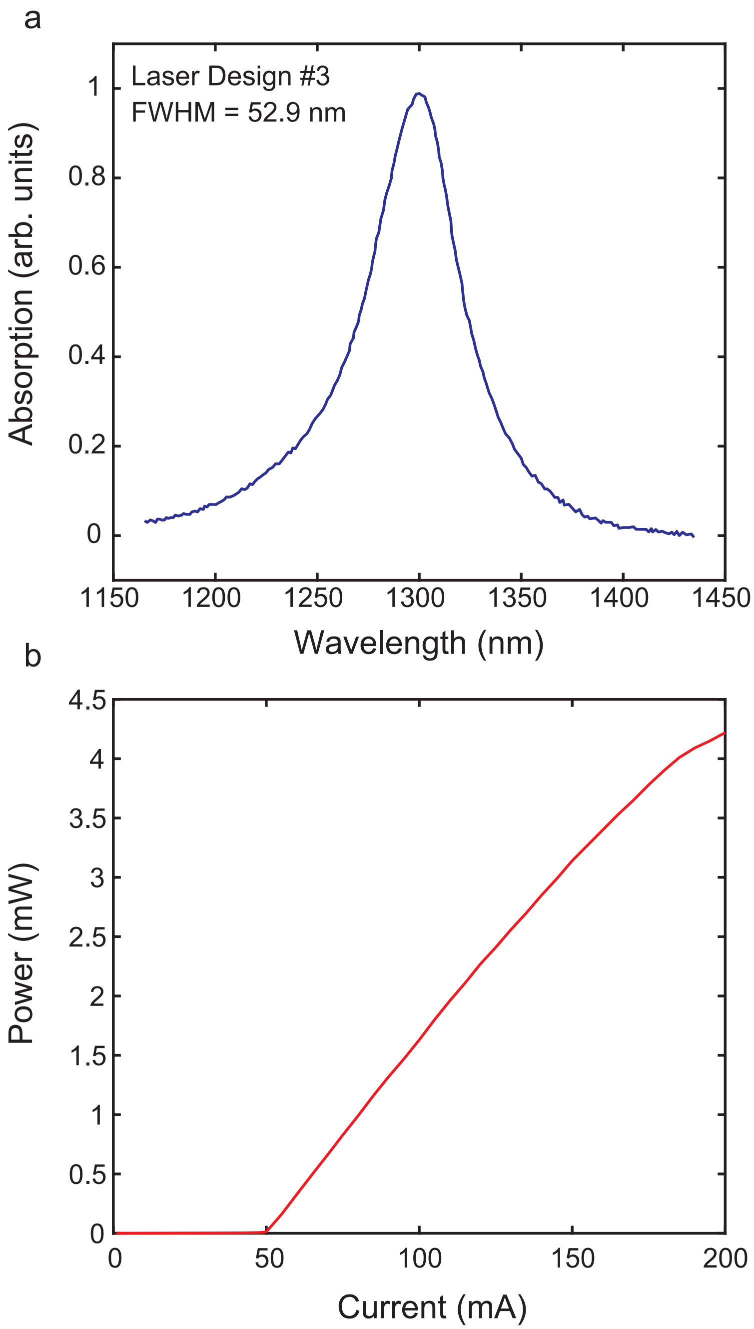

Figure 9.10: a) absorption spectrum of the QWs for the 1.3 μm laser, or S3 (absorption data courtesy of Xiamen Powerway). The band edge of the QW is shifted down to 1.3 μm. b) a typical LI curve of our S3 fabricated laser diodes.

9.3 Characterization of the 1.3 μm Laser

Lastly, we move to our third (S3) and final design, the 1.3 μm laser diode. Our theoretical model has calculated that the diffusion should still be low enough at this

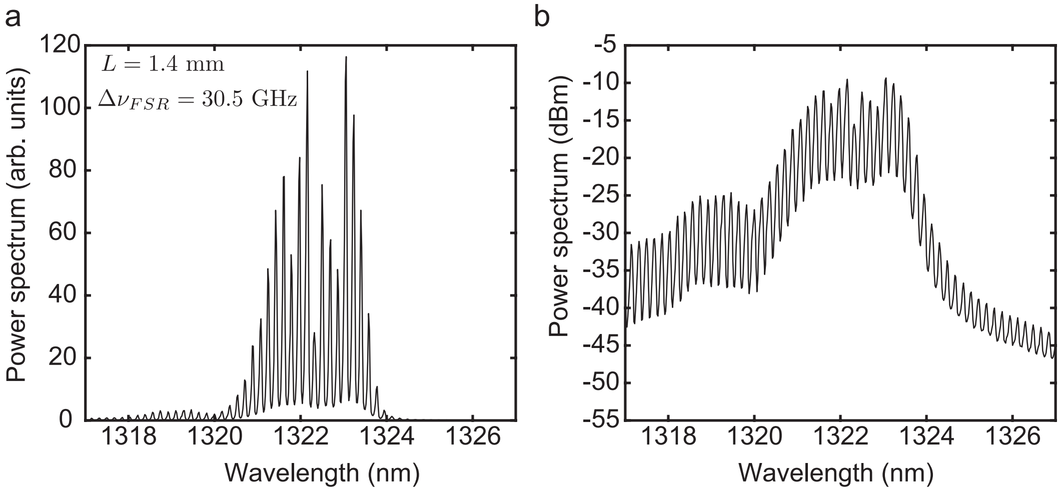

Figure 9.11: Measured optical spectrum of an S3 laser diode at pump current $I = 135$ mA. a) linear and b) log scale plot of the optical spectrum of a length 1.4 mm laser diode, corresponding to an FSR of 30.5 GHz. The QW laser diode still exhibits comb behavior at the shorter, 1.3 μm operating wavelength.

wavelength to generate combs, albeit with slightly degraded performance due to the weaker SHB effect. The absorption spectrum for this laser design is shown in Figure 9.10a, while a typical LI curve is shown in Figure 9.10b. Again, the power output is several mW, similar to that of the first two designs. Also, we once more use the same experimental setup as described for laser design S1 - the major difference is simply adjusting the equipment settings for 1.3 μm.

The absorption spectrum for this laser design is shown in Figure 9.10a, with another typical LI curve in Figure 9.10b. The absorption profile now has a center around 1300 nm and has a similar bandwidth to the S1 design, while the LI curve outputs several mW of power.

A typical optical spectrum is shown in Figure 9.11 for the S3 design. A frequency comb with a bandwidth of about 4 nm (≈ 0.7 THz at 1.3 μm) is seen. The spectrum is not as sharp as the ones shown for 1.5 μm due to our spectrum analyzer having more limited resolution being fixed at 0.05 nm, which corresponds to a larger sampling steps in frequency due to the lower wavelength. Despite this, we are still able to

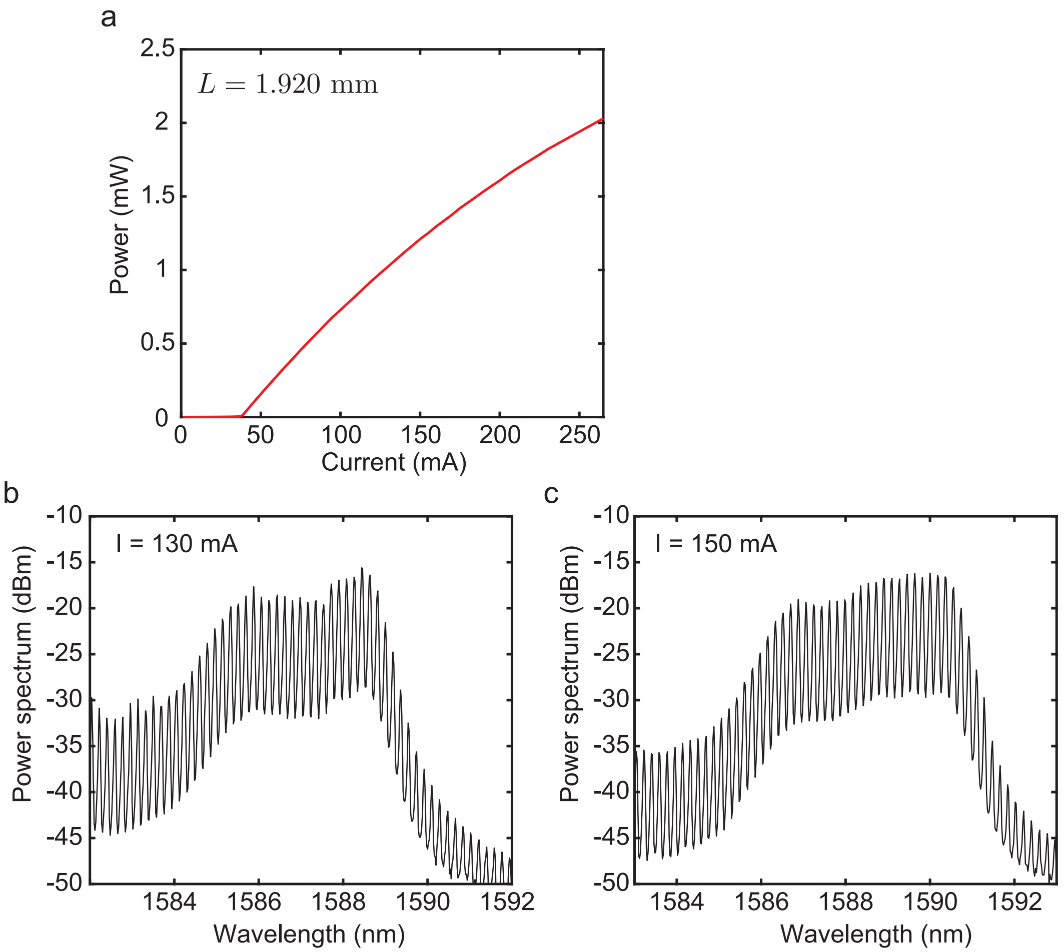

Figure 9.12: Measurements of a length 1.92 mm laser operating at 1.5 μm (S1) a) the LI curve b) optical spectrum at an input current of $I = 130$ mA c) optical spectrum at an input current of $I = 150$ mA.

resolve many comb lines. Overall, the number of comb lines is not as large as the 1.5 μm lasers with a similar decrease in bandwidth.

The comb behavior of the 1.3 μm is an important experimental confirmation of our theoretical predictions, that an optical comb can be generated at this wavelength with QW gain media. While combs at this frequency have been generated with QD lasers [57], we have shown that it is also possible with QW lasers.

9.4 RF Measurements

While we have characterized the optical spectrum of our laser designs, we still need to characterize the coherence of the modes. To perform this measurement, we utilize a self-heterodyning technique which measures the interference of all the comb lines with each other. To do this, we simply feed our fiber which couples the light from the laser into an ultrafast photodiode (Newport 1014). The detector translates our optical spectrum into an RF signal which is then analyzed in a high frequency electrical spectrum analyzer (HP E4408B). Typically, a very narrow RF linewidth suggests extremely stable comb spacing and low amplitude noise, both indicators of phase-coherence between the optical modes.

First, we measure the RF signal of our 1.5 μm laser (design S1). Because of the of limited equipment on hand at the time, such as our electrical spectrum analyzer only reads up to 26 GHz, we are only able to obtain data on our longer lasers with smaller FSR. The LI curve and some optical spectra are shown in Figure 9.12 as a reference for the RF measurements. The actual RF spectra are shown in Figure 9.13. There is a clear trend in the RF linewidths and signal to noise ratio (SNR): as the input current increases, the SNR greatly increases while the linewidth greatly decreases. This is good for our laser operation, as the coherence of the laser improves with increasing laser power (as well as frequency comb bandwidth). The lowest measured RF linewidth is around 240 kHz, a very small fraction of the FSR. This should be sufficiently narrow for dual-comb experiments in which the two combs have different repetition rates separated by a few 100s of kHz to a few MHz.

There are some additional stability considerations not captured by Figure 9.15. Over a period of a few seconds (quite long relative to the laser frequency), the RF peak around 21.85 GHz does tend to drift over a value of 500 kHz - 1 MHz. During this drift, the linewidth does not seem to change significantly and the fact that the time scales for this effect are on the order of seconds suggests a temperature stabilization

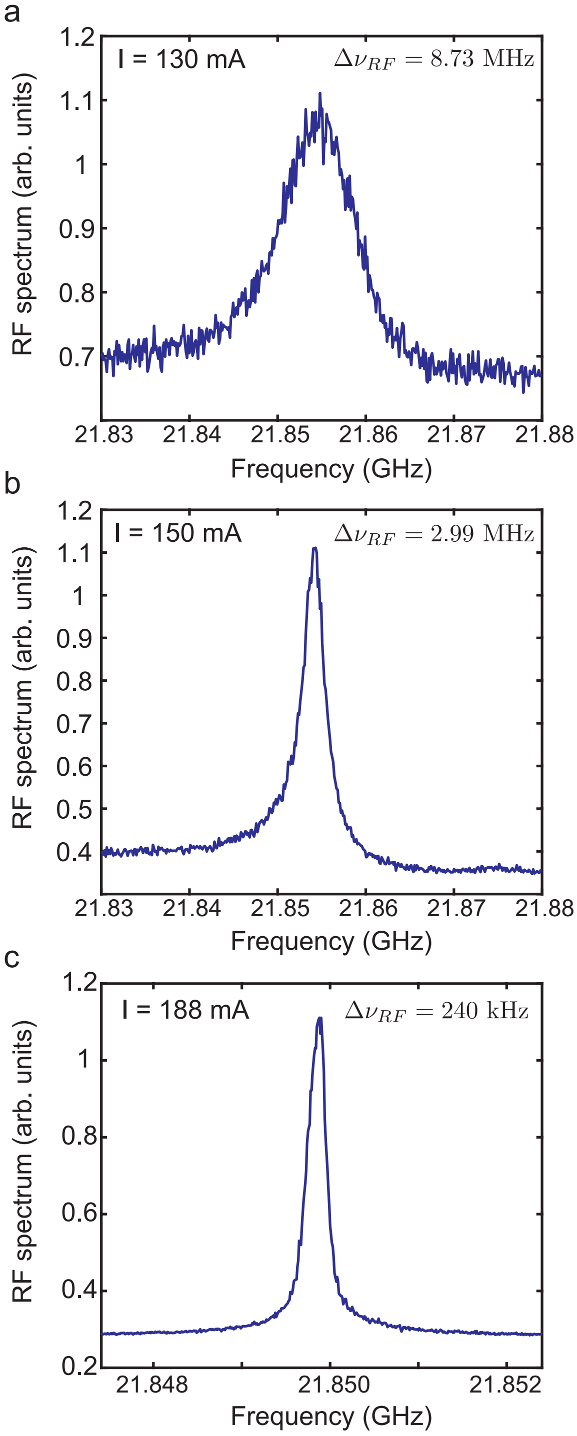

Figure 9.13: RF spectrum of the 1.92 mm laser at different pump currents. Each spectrum is normalized and averaged over 40 acquisitions. a) RF spectrum at $I = 130$ mA b) RF spectrum at $I = 150$ mA c) RF spectrum at $I = 188$ mA.

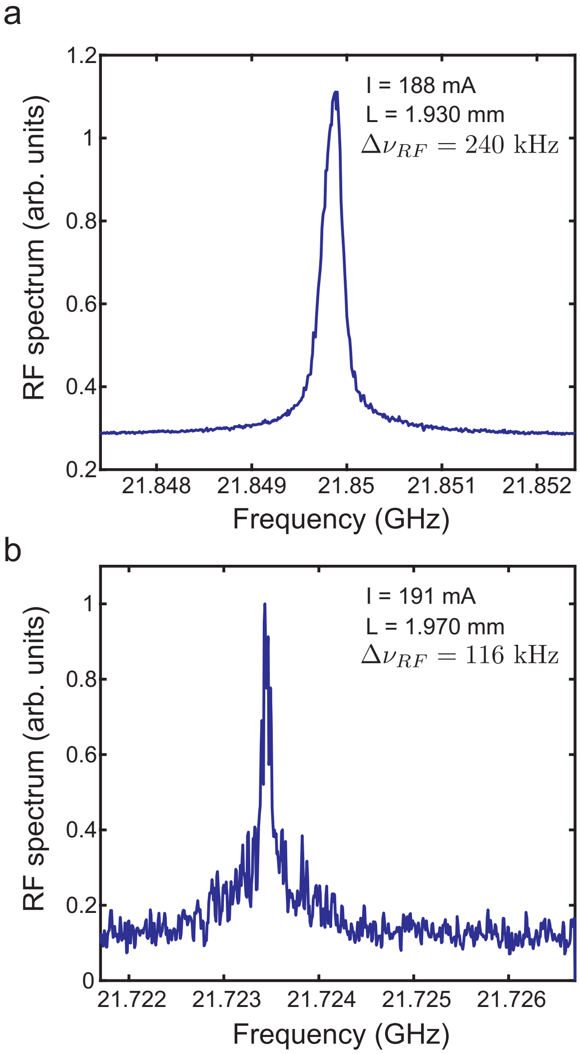

Figure 9.14: RF spectrum of an approximately 2 mm laser comparing the S1 and S2 coherences. a) S1 design RF spectrum at $I = 188$ mA b) S2 (asymmetric QWs) design RF spectrum at $I = 191$ mA

problem. The TEC controller does record small oscillations in temperature over longer periods of time. The drift can likely be improved by adjusting the temperature PID settings and, as already mentioned, improving our temperature control setup.

While the 1550 nm laser has shown to be coherent, we do a direct comparison between the four identical QW design and the asymmetric QW design to ensure that the asymmetric QW design still retains the necessary FWM for phase coherence between the separate QWs. We again compare two lasers of similar length and with

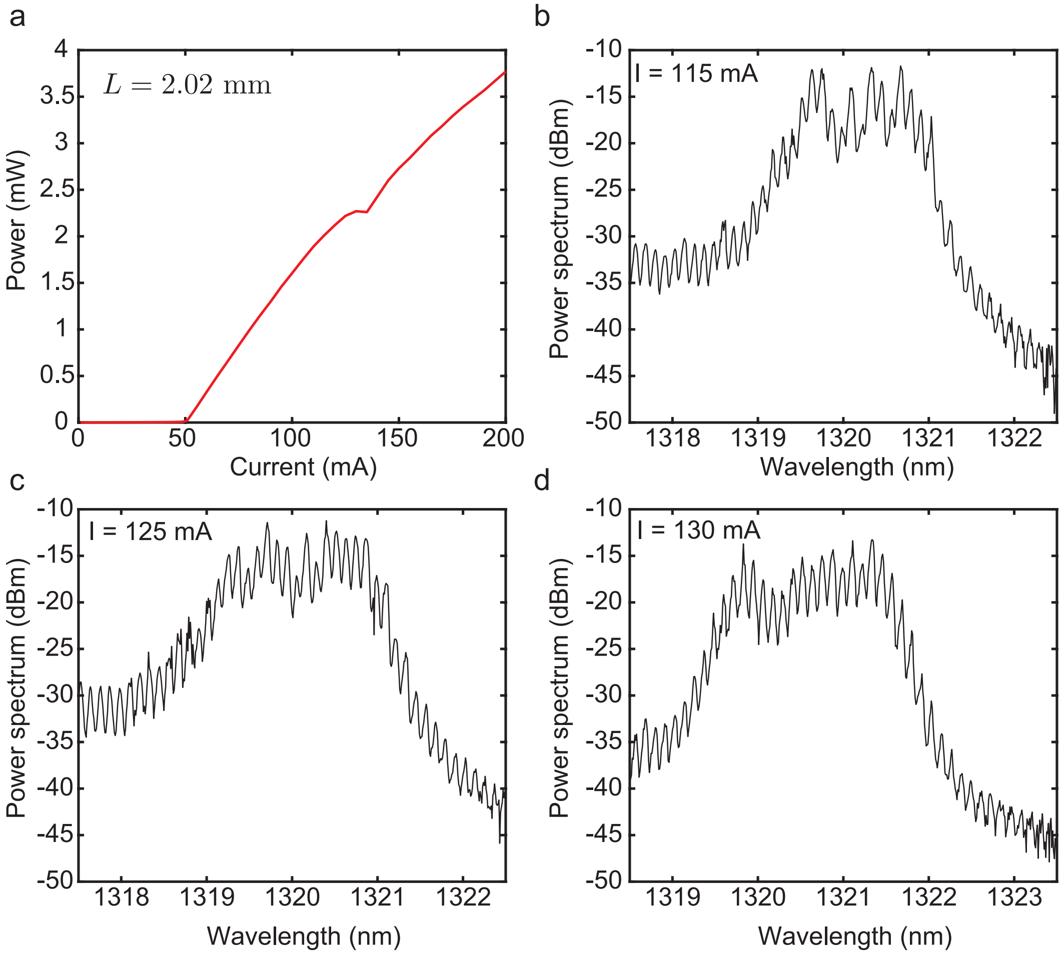

Figure 9.15: Measurements of a length 2.02 mm laser operating at 1.3 μm (S3) a) the LI curve b) optical spectrum at an input current of $I = 115$ mA c) optical spectrum at an input current of $I = 125$ mA and d) optical spectrum at an input current of $I = 130$ mA.

similar injection current. The RF spectra are shown in Figure 9.14. The S1 RF spectrum (Figure 9.14a) has been averaged 40 times, while the S2 RF spectrum (Figure 9.14b)has been averaged only twice, due to the nature of the equipment used for the measurement. The coherence has not been lost in the transition to the asymmetric QW, as seen in that the RF linewidth is even narrower in the asymmetric case (116 kHz). The narrower line could be attributed to the fact that the RF signal tends to drift and the fewer averages in measurement actually shows a narrower line.

Moving onto the 1.3 μm laser (design S3), we perform similar RF measurements

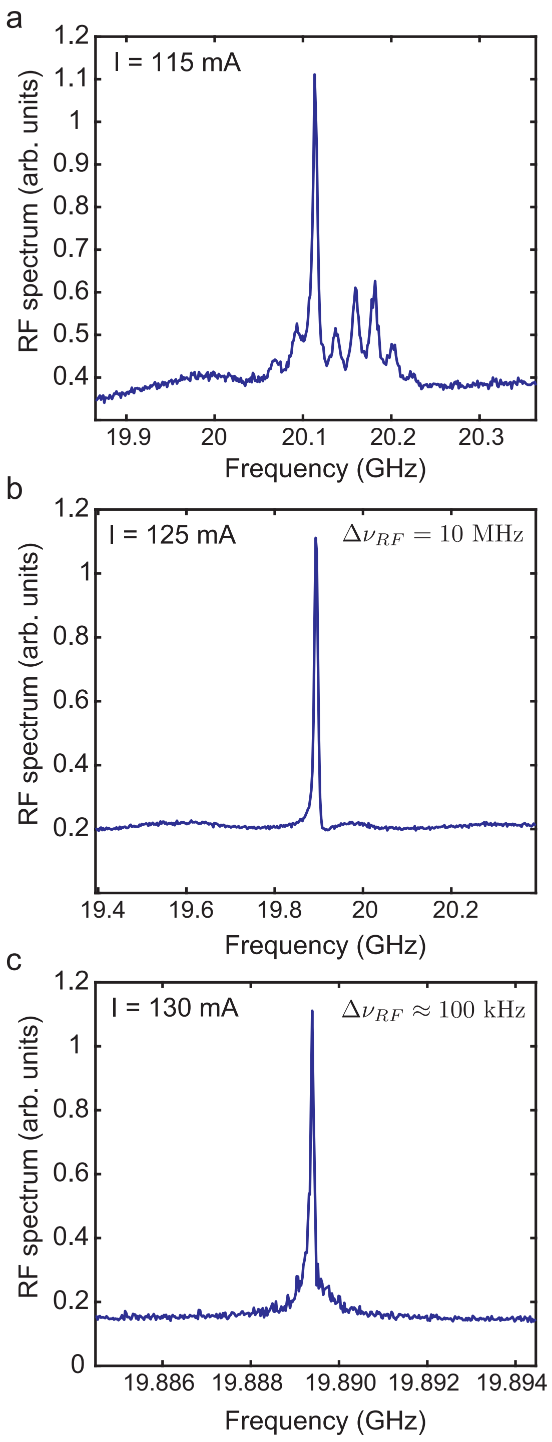

Figure 9.16: RF spectrum of the 2.02 mm laser at different pump currents. a) RF spectrum at $I = 115$ mA, averaged over 40 acquisitions b) RF spectrum at $I = 125$ mA, averaged over 40 acquisitions c) RF spectrum at $I = 130$ mA without averaging, only a single acquisition is shown.

for the characterization of the coherence. The LI curve and some optical spectra for reference are shown in Figure 9.15. The RF spectra are shown in Figure 9.16. The optical spectra for these pump currents resemble frequency combs similar to the 1.5 μm laser, but are not as flat or stable. The RF lines show interesting behavior: at low injection currents, (Figure 9.16a), there is not a single RF line but multiple, suggesting that the comb spacing is not constant and varies between the optical modes. However, as the current injection is increased, the weaker RF lines disappear while the center line narrows and increases in signal. This increase in coherence as power is increased is consistent with the previous RF measurement for the 1.5 μm laser.

The lowest RF linewidth we captured is shown in Figure 9.16c, about 100 kHz. While this value indicates good coherence, the long term comb stability is not as good as the 1.5 μm laser. This is the reason the measurement in Figure 9.16c is not averaged but is only a single acquisition. Over time, the RF peak tends to drift a significant amount (>5 MHz) and sometimes disappears entirely, only to reappear in a few seconds. These effects are possibly due to temperature effects and weaker SHB because of the lower operating wavelength. These effects combine to make the 1.3 μm QW lasers less practical than the 1.5 μm QW lasers, unless more engineering is done to ensure more stable laser operation.

There is an unusual feature in the LI curve for this laser, in which there is a bump in the laser power around $I = 130$ mA before resuming its increase. Past this point, the RF line no longer appears and the optical spectra do not resemble combs anymore, as shown in Figure 9.17. It is possible that the QW has been saturated at this point and the bulk SCH layer started to lase. In this scenario, we would no longer have the necessary elements for comb generation (strong SHB) due to the lack of confined carriers. This effect only occurs in the 1.3 μm lasers, as the QW depth is much smaller (70 meV for electrons, 104 meV for holes) compared to that in the 1.5 μm QWs (133 meV for electrons, 200 meV for holes).

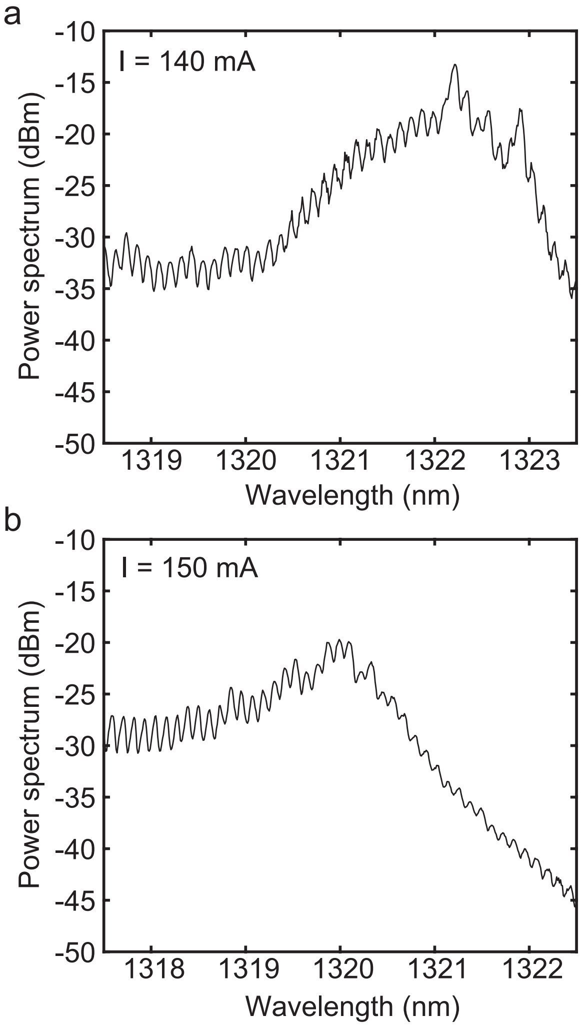

Figure 9.17: Optical spectra of the 2.02 mm laser at high pump currents. a) optical spectrum at $I = 140$ mA b) optical spectrum at $I = 150$ mA. The comb structure is greatly weakened and no longer significant.

Another observation we would to note is that an RF line is observable for most input currents in our laser diodes. This suggests that the output is not purely FM, as such phase modulations would not be picked up by the photodetector. The output likely is a mix of amplitude and frequency modulation such that periodic intensity patterns are generated and picked up by our detector and transformed into an electrical signal. Our theoretical models indeed show an amplitude modulation on top of a CW base. However, future experiments such as an autocorrelation measurement would better confirm the time domain output of our laser diodes.

In summary, the 1.3 μm laser still exhibits a coherent comb at certain pump currents, even though its performance is slightly worse than the 1.5 μm lasers. This experimentally validates our theoretical models of working frequency combs based on of QW gain at lower wavelengths, opening up the possibility for tailoring QW laser diodes to operate in any wavelength in the 1.3 μm - 1.6 μm range.

9.5 Additional Discussion

The behavior of the RF measurements is consistent with our theoretical prediction that the frequency comb coherence should increase as laser power is increased. From the equations in Chapter VII, the pulsating carrier population lifetime is

$$\tau_p = \left[\frac{1}{\tau_{sp}} + i\omega_s + 2R(|A_0|^2 + |B_0|^2)\right]^{-1} . \tag{9.1}$$

As the laser power out and the intracavity power, $|A_0|^2 + |B_0|^2$, increase, the overall pulsating lifetime is shortened while its real part starts to dominate the imaginary part. This allows for the pulsating carriers to follow in phase with the electric field.

For our 2 mm cavity length lasers emitting a power of $P = 2.5$ mW, we can estimate the intracavity power to be approximately

$$|A_0|^2 + |B_0|^2 \approx \frac{P}{1-r} + rP = 4.9 \text{ mW} ,$$

where $r = 0.32$ is the power reflection coefficient. At this amount of intracavity power, the pulsating lifetime is found to be

$$\begin{aligned} |\tau_p| &= 2.8 \text{ ps} \\ \frac{Re(\tau_p)^2}{|\tau_p|^2} &= 0.86 . \end{aligned}$$

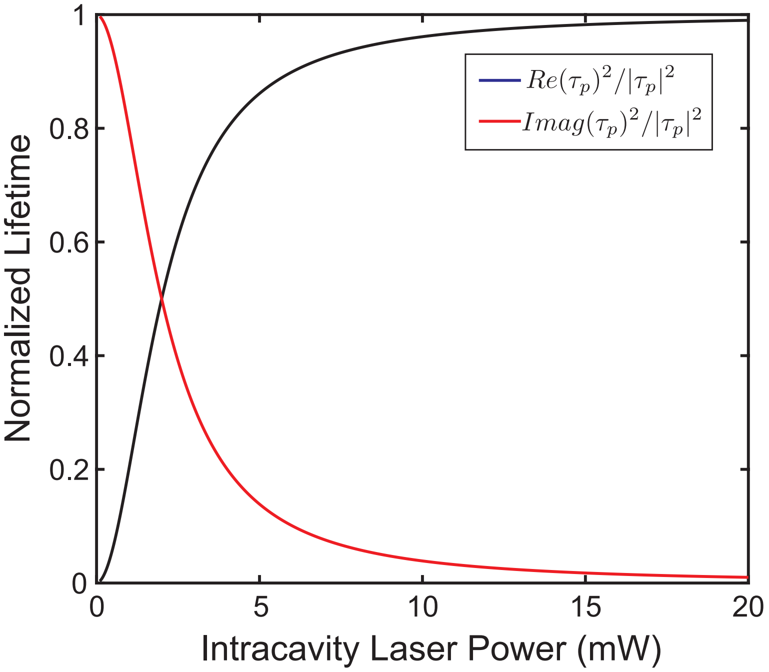

Figure 9.18: A plot of the real and imaginary parts of the pulsating lifetime τ_p (Equation 9.1) as a fraction of the total lifetime for a 2 mm long cavity. The real part of τ_p affects the coherence between the optical modes.

The real portion of τ_p is already much larger (86%) than the imaginary portion (14%), even though the output power is still relatively low. A plot of the fraction of real and imaginary parts of τ_p is shown in Figure 9.18. The overall trend is clear: when there is very little or no intracavity power inside the laser, the pulsating lifetime is almost purely imaginary because the spontaneous lifetime (1 ns) is very long relative to the round trip time (46 ps for a 2 mm cavity length). As the laser power increases, the lifetime is greatly reduced while the real part greatly increases until it dominates. This increases the strength of the FWM and thus reducing the RF linewidth as seen in our experimental results.

All things considered, longer lasers seem to be preferable to shorter lasers. Longer lasers have a smaller FSR, which will be beneficial as they do not require as much power for efficient FWM due to the carrier population not needing to oscillate as quickly. Moreover, a smaller FSR provides more resolution in dual-comb experiments for measuring smaller absorption linewidths (such as vibrational modes in carbon monoxide). Longer lasers also benefit by being less sensitive to cavity losses, as the mirror reflections are not as significant compared to shorter lasers.

Compared to previous QW laser diodes [55, 54], our devices have comparable bandwidth and RF spectral coherence (about 1 THz bandwidth, 100 kHz RF linewidth). Generally, the lengths of our lasers are longer than previous lasers (2 mm vs 1 mm, respectively), giving us a smaller mode spacing, which should be beneficial for spectroscopy. The major difference in our lasers is that our total power is less than that of previously reported (our lasers are 3-4 mW, while previous published literature have stated 15-20 mW). This can be improved upon by improving our laser cavity and semiconductor designs for reduced losses.

9.6 Conclusion

To conclude this chapter, we have characterized our laser diodes, showing that they indeed generate frequency combs as we expected. Their optical spectra show combs up to 1.2 THz bandwidth at -10 dB with a center wavelength of 1.3 μm - 1.6 μm. The narrow RF linewidths, from 100 kHz - 200 kHz, indicate good mutual coherence between the comb lines. The coherence of the frequency combs follows our theoretical predictions in which higher laser power improves the FWM effect, as seen by the narrowing of the RF linewidth with increasing intracavity power. With these characteristics, these laser diodes have much potential to be useful alternatives to current frequency comb sources, possibly acting as a primary source of combs in fiber lasers, or used directly as a frequency comb in free space spectroscopy.

CHAPTER X

Conclusion and Future Directions

As a conclusion to this work, we present a short summary of our work as well some future directions and applications of these laser diode frequency combs. We have studied the nature of traveling wave electric field models and the numerical schemes in which to solve them as a powerful tool for modeling optical phenomenon. We have applied the traveling wave model, while also developing new and predictive theories, to pulsed and cascaded stimulated Brillouin scattering. From there, we have developed a comprehensive model of laser diodes incorporating many elements of semiconductor physics in order to predict the generation of frequency combs directly from single section lasers without a saturable absorber. These calculations demonstrate the feasibility and material requirements for FM comb generation. We further study the physics of FM comb generation in laser diodes by simplifying our comprehensive model and finding some analytical solutions to our wave equations, illuminating the importance of FWM and SHB in the generation of frequency combs. Finally, we have undertaken experimental fabrication and design of InGaAsP/InP based laser diodes, successfully characterizing that their spectra consist of frequency combs with about a 1 THz bandwidth and good coherence with RF linewidths around 200 kHz.

As for possible future experiments and applications, the combs at 1.55 μm can be easily amplified with erbium-doped amplifiers (combs at 1.064 μm can be amplified with ytterbium) and dispersion compensated in single mode fibers to form pulses to be used directly in spectroscopy. Alternatively, after amplification, the pulses can be frequency doubled through nonlinear crystals to 800 nm, expanding their usefulness in spectroscopy. For combs operating less than 1.3 μm, dispersion compensation may be trickier as fibers are not anomalously dispersive at wavelengths less than 1.3 μm, but can still be accomplished with dispersion shifted fibers. Additional measurements include autocorrelation, which can distinguish whether the output is pulsed or FM, and optical heterodyning to establish the optical linewidth and coherence for absolute spectroscopy measurements.

While there are some potential shortcomings of these sources compared to fiber or Ti:Sapphire mode-locked lasers, there are major compensations that help alleviate these shortcomings. The laser diode frequency combs typically have lower output power, but as mentioned already, they can be amplified with erbium or ytterbium doped fibers and passively dispersion compensated in the same fiber system. This eliminates free-space components such as moving gratings and mirrors and, more critically, the saturable absorber altogether, greatly simplifying the design of the system. Finding the mode- locked regime is mostly automatic and much more robust with laser diode combs. Another issue that could be problematic is the lack of tunability of the comb spacing once the lasers are cleaved. However, this can be alleviated by integrating several laser diodes of different cavity lengths (at negligible additional cost) into the same system that can be selectively turned on and off. While this reduces our choices of frequency comb spacing, the elimination of moving mechanical parts greatly improves the stability and viability of using these combs in the field.

For future theoretical work, we can extend our laser model to applications such as dual-comb spectroscopy and calculating the effects of combining the outputs of independent laser diodes. Additionally, we can also include a full many-body calculation of the semiconductor quantum-well gain medium while maintaining the traveling-waves.. This approach would require the use of the semiconductor Bloch equations that takes into account Coulomb interactions and screening, carrier-carrier scattering, and band structure calculations. Such calculations are not trivial, as all carrier equations would now be coupled to every other carrier equation, which would likely require a more sophisticated numerical computation scheme.

The overall major significance is that all of the frequency comb applications at these wavelengths would now be much more accessible to researchers in science and industry. The relatively inexpensive and solid-state nature of laser diode based frequency combs allows them to be mounted on vehicles and robots, greatly enhancing military and national safety applications such as explosive and biochemical weapons detection. In addition, they may be deployed on drones or in hand-held devices for civilian applications such as atmospheric sensing or metrology in chemistry and biology. Many possibilities open up with further engineering and development of these frequency combs.

A list journal and conference publications born from this research is shown below.

Journal publications

M. Dong, S. T. Cundiff, and H. G. Winful, "Physics of Frequency Modulated Comb Generation in Quantum Well Diode Lasers," accepted for publication, *Phys. Rev. A*, (2018)

M. Dong, N. M. Mangan, J. N. Kutz, S. T. Cundiff, and H. G. Winful, "Traveling Wave Model for Frequency Comb Generation in Single-Section Quantum Well Diode Lasers," *IEEE J. Quantum Electron.*, 53, 2500311 (2017).

M. Dong and H. G. Winful, "Unified approach to cascaded stimulated Brillouin scattering and frequency comb generation," *Phys. Rev. A*, 93, 043851 (2016).

M. Dong and H. G. Winful, "Area dependence of chirped-pulse stimulated Brillouin scattering: implications for stored light and dynamic gratings," *JOSA B*, 32, 2514-

2519 (2015)

Conference publications

M. Dong, S. T. Cundiff, and H. G. Winful, ”Physics of Self-Generated Combs in Semiconductor Diode Lasers,” *Self-Generation of Optical Frequency Combs in Semiconductor Lasers*, Turin, Italy (2017)

M. Dong, S. T. Cundiff, and H. G. Winful, ”Physics of Frequency Modulated Comb Generation in Semiconductor Diode Lasers,” *Nonlinear Optics*, NM2A.4 (2017)

M. Dong, N. M. Mangan, J. N. Kutz, S. T. Cundiff, and H. G. Winful, ”Model for Frequency Comb Generation in Single-Section Quantum Well Diode Lasers,” *CLEO*, JTu5A.102 (2017)

M. Dong and H. G. Winful, ”A new theoretical approach to cascaded stimulated Brillouin scattering,” *CLEO*, JW2A.55 (2016)

M. Dong and H. G. Winful, ”Area dependence of chirped-pulse stimulated Brillouin scattering,” *Nonlinear Optics*, NF1A.3 (2015)

APPENDIX

Fabrication Tools Settings

We list the details of some of the laser diode fabrication steps here, as well as some tips and tricks for avoiding several problems we encountered.

GCA AS200 AutoStep Exposure Recipes

The exposure using the AS200 AutoStep, or also called the Stepper, utilizes custom recipes and settings due to size of our pieces. Normally, this tool is using default settings for 100 mm (or 4 inch), 550 μm wafers and we have to make sure these settings are adjusted for our 1.0 cm^2, 350 μm pieces. The SOP for the tool has been updated to accommodate leveling the chuck by focusing directly on the small pieces. The names of the two recipes for exposure are MARK1 (0.3 second exposure) and MARK2 (0.32 second exposure). The first being the first exposure step without any marker alignments, while the second requires an alignment step.

The alignment tolerance on the tool is only ± 0.44 μm, as this is the smallest step the stage can take. Obviously, this causes problems for very precise alignments, especially if we need to overlay a 2 μm waveguide on top of a another one. While our described oxide lift-off process does not require such precise alignment, the PECVD approach does require it. In those cases, it is good to run several alignment steps and

Oxford ICP Parameter	Value
RF Power	110 W
ICP Power	200 W
Process pressure	18 mTorr
CH_4 gas flow	30 sccm
H_2 gas flow	10 sccm
Temperature	50 C

Table A.1: Tool parameters for the Oxford ICP RIE InP etching recipe.

exposures and manually adjust the stage for small errors in alignment, using previous exposure steps as a reference. Errors in the AutoStep stage and lens alignments, as well as errors in the mask maker, can be corrected this way.

InP Dry Etching Recipe

Dry etching of InP is performed in the Oxford ICP RIE with a custom recipe loaded onto the tool (XDev InP) that uses methane and hydrogen plasmas as etchants. Our process follows the results of Lee, *et al.* [104]. We have listed the parameters in Table A.1 for the recipe settings. There is no oxygen flow in this recipe, which is a minor difference from the process in [104]. This gives about a 100 nm/min etch rate for InP, while it is a little slower while etching InGaAs.

Silicon Oxide Deposition

We use the AE Evaporator to deposit thin films in the fabrication process. While depositing gold is relatively straightforward, depositing oxide is a little trickier. There are two problems to be aware of:

1. The deposition of the oxide is not perfectly vertical, as there is significant build up on the sides of the ridges;
2. The oxide does not stick well to the crystal monitoring the deposition rate.

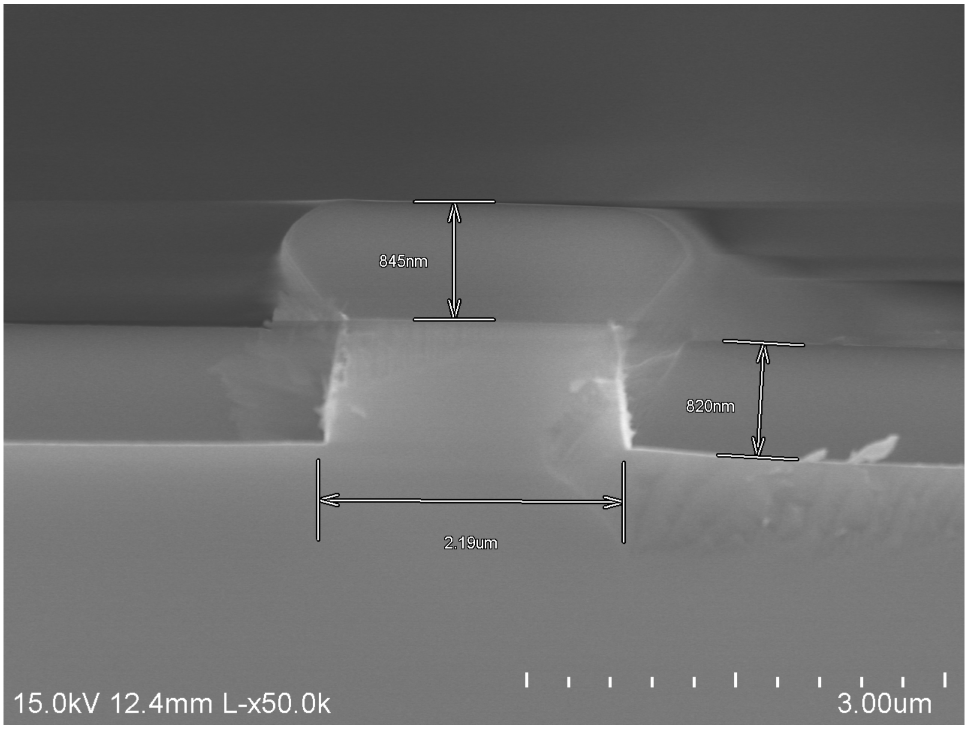

Figure A.1: An SEM of the laser ridge after 850 nm of oxide deposition. The sides and top have unusual shapes due to the slightly non-vertical nature of the deposition tool.

The first problem can be useful as we are hoping for good side wall coverage. However, this means that the oxide layer cannot be too thick - a value around 650-750 nm for a 1 μm ridge is good. If the oxide is too thick, the sides of the photoresist become covered and lift-off is nearly impossible. This means that the second problem is more potent as it exacerbates the first problem. Hitting the range of 650-750 nm may not be easy due to the inaccuracy of deposition. A solution for this is to first deposit 100 Å of titanium in an empty chamber to condition the crystal. That way, the oxide deposition is more accurate.

Buffered HF Etch Rates

While we did not use wet etching in the end process, a characterization of the etch rate is given here. The buffered oxide etch (BHF) available in the LNF is Buffer HF

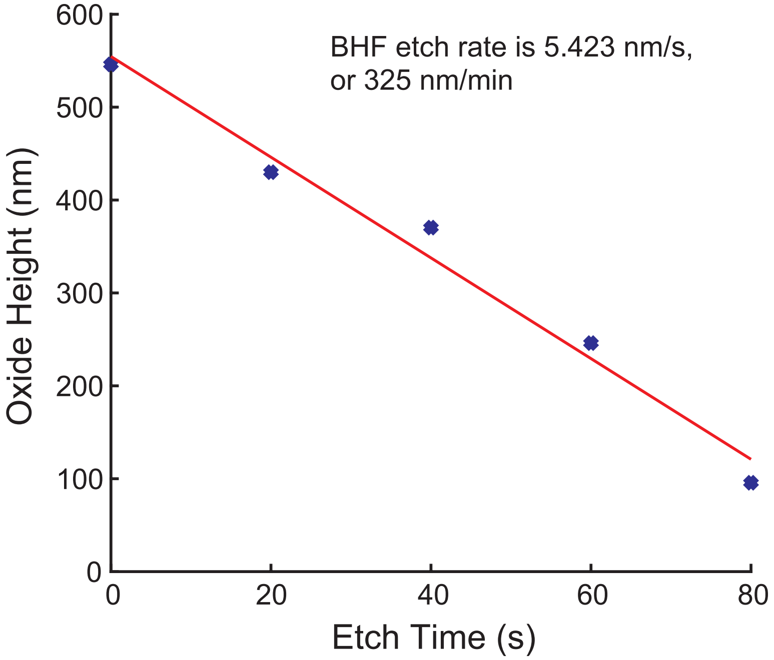

Figure A.2: A plot of the etch rate using Buffer HF improved etchant. The blue crosses are experimental data while the red line is the fit. The fitting gives an etch rate of about 325 nm/min.

improved from Transene Company, Inc.. We tested this etchant on 350 C PECVD oxide, grown in the Plasmatherm 790 tool (recipe L_OX350). The etch rate is about 325 nm/min, with the graph shown in Figure A.2.

BIBLIOGRAPHY

BIBLIOGRAPHY

[1] S. T. Cundiff and J. Ye, "Femtosecond optical frequency combs," *Rev. of Mod. Phys.*, vol. 75, p. 325, March 2003.

[2] T. Udem, J. Reichert, R. Holzwarth, and T. W. Hänsch, "Absolute optical frequency measurement of the Cesium D1 line with a mode-locked laser," *Phys. Rev. Lett.*, vol. 82, no. 18, p. 3568, 1999.

[3] M. J. Thorpe, D. D. Hudson, K. D. Moll, J. Lasri, and J. Ye, "Cavity-ringdown molecular spectroscopy based on an optical frequency comb at 1.45–1.65 μm," *Optics Letters*, vol. 32, no. 3, p. 307, 2007.

[4] S. A. Diddams, T. Udem, J. C. Bergquist, E. A. Curtis, R. E. Drullinger, L. Hollberg, W. M. Itano, W. D. Lee, C. W. Oates, K. R. Vogel, and D. J. Wineland, "An optical clock based on a single trapped 199 Hg1+ ion," *Science*, vol. 293, p. 825, 2001.

[5] S. T. Cundiff and A. M. Weiner, "Optical arbitrary waveform generation," *Nat. Phot.*, vol. 4, p. 760, 2010.

[6] D. J. Jones, S. A. Diddams, J. K. Ranka, A. Stentz, R. S. Windeler, J. L. Hall, and S. T. Cundiff, "Carrier-envelope phase control of femtosecond mode-locked lasers and direct optical frequency synthesis," *Science*, vol. 288, pp. 635–639, 2000.

[7] I. Coddington, W. C. Swann, and N. R. Newbury, "Coherent multiheterodyne spectroscopy using stabilized optical frequency combs," *Phys. Rev. Lett.*, vol. 100, p. 13902, 2008.

[8] G. B. Rieker, F. R. Giorgetta, W. C. Swann, J. Kofler, A. M. Zolot, L. C. Sinclair, E. Baumann, C. Cromer, G. Petron, C. Sweeney, P. P. Tans, I. Coddington, and N. R. Newbury, "Frequency-comb-based remote sensing of greenhouse gases over kilometer air paths," *Optica*, vol. 1, no. 5, p. 290, 2014.

[9] S. T. Cundiff and S. Mukamel, "Optical multidimensional coherent spectroscopy," *Physics Today*, p. 44, July 2013.

[10] B. Lomsadze and S. T. Cundiff, "Frequency combs enable rapid and high-resolution multidimensional coherent spectroscopy," *Science*, vol. 357, pp. 1389–1391, 2017.

[11] M. E. Fermann and I. Hartl, “Ultrafast fibre lasers,” *Nat. Phot.*, vol. 7, p. 868, 2013.

[12] D. H. Sutter, G. Steinmeyer, L. Gallmann, N. Matuschek, F. Morier-Genoud, U. Keller, V. Scheuer, G. Angelow, and T. Tschudi, “Semiconductor saturable-absorber mirror-assisted Kerr-lens mode-locked Ti:sapphire laser producing pulses in the two-cycle regime,” *Opt. Lett.*, vol. 24, p. 631, 1999.

[13] R. Boyd, *Nonlinear Optics*. Academic, Burlington, 3 ed., 2008.

[14] P. R. Berman and V. S. Malinovsky, *Principles of Laser Spectroscopy and Quantum Optics*. 41 William Street, Princeton, NJ 08540: Princeton University Press, 2011.

[15] G. Agrawal, *Nonlinear Fiber Optics*. Academic, Burlington, 4 ed., 2007.

[16] C. M. de Sterke, K. R. Jackson, and B. D. Robert, “Nonlinear coupled-mode equations on a finite interval: a numerical procedure,” *J. Opt. Soc. Am. B*, vol. 8, no. 2, p. 403, 1991.

[17] J. Deng and L. Ma, “Existence and uniqueness of solutions of initial value problems for nonlinear fractional differential equations,” *Applied Mathematics Letters*, vol. 23, no. 6, pp. 676–680, 2010.

[18] W. H. Press, S. A. Teukolsky, W. T. Vetterling, and B. P. Flannery, *Numerical Recipes The Art of Scientific Computing*. Cambridge University Press, 2007.

[19] R. Y. Chiao, C. H. Townes, and B. P. Stoicheff, “Stimulated Brillouin scattering and coherent generation of intense hypersonic waves,” *Phys. Rev. Lett*, vol. 12, p. 592, 1964.

[20] K. Y. Song, W. Zou, Z. He, and K. Hotate, “All-optical dynamic grating generation based on Brillouin scattering in polarization-maintaining fiber,” *Opt. Lett.*, vol. 33, pp. 926–928, 2008.

[21] R. Pant, E. B. Li, C. G. Poulton, D. Y. Choi, S. Madden, B. Luther-Davies, and B. J. Eggleton, “Observation of Brillouin dynamic gratings in a photonic chip,” *Opt. Lett.*, vol. 38, pp. 305–307, 2013.

[22] C. Florea, “Stimulated Brillouin scattering in single-mode As_2S_3 and As_2Se_3 chalcogenide fibers,” *Opt. Exp.*, vol. 14, pp. 12063–12070, 2006.

[23] M. Santagiustina, S. Chin, N. Primerov, L. Ursini, and L. Thévenaz, “All-optical signal processing using dynamic Brillouin gratings,” *Sci. Rep.*, p. 1594, 2013.

[24] H. G. Winful, “Chirped Brillouin dynamic gratings for storing and compressing light,” *Opt. Express*, vol. 21, pp. 10039–10047, 2013.

[25] Z. Zhu, D. J. Gauthier, and R. W. Boyd, "Stored light in an optical fiber via stimulated Brillouin scattering," *Science*, vol. 318, pp. 1724–1750, 2007.

[26] H. Shin, W. Qiu, R. Jarecki, J. A. Cox, R. H. O. III, A. Starbuck, Z. Wang, and P. T. Rakich, "Tailorable stimulated Brillouin scattering in nanoscale silicon waveguides," *Nat. Commun.*, vol. 4, p. 1944, 2013.

[27] B. J. Eggleton, C. G. Poulton, and R. Pant, "Inducing and harnessing stimulated Brillouin scattering in photonic integrated circuits," *Adv. in Opt. and Phot.*, vol. 5, no. 4, p. 536, 2013.

[28] M. Dong and H. G. Winful, "Area dependence of chirped-pulse stimulated Brillouin scattering: implications for stored light and dynamic gratings," *J. Opt. Soc. Am. B*, vol. 32, no. 2, p. 2514, 2015.

[29] I. Y. Dodin and N. J. Fisch, "Storing, retrieving, and processing optical information by Raman backscattering in plasmas," *Phys. Rev. Lett.*, vol. 88, p. 165001, 2002.

[30] E. J. R. Kelleher, J. C. Travers, E.P.Ippen, Z. Sun, A. C. Ferrari, S. V. Popov, and J. R. Taylor, "Generation and direct measurement of giant chirp in a passively mode-locked laser," *Opt. Lett.*, vol. 34, no. 22, pp. 3526–3528, 2009.

[31] M. Baldo, G. E. Town, and M. Romagnoli, "Generation of highly chirped pulses in a diode-pumped optical fiber laser," *Opt. Commun.*, vol. 140, pp. 19–22, 1997.

[32] A. Bambini and P. R. Berman, "Analytic solutions to the two-state problem for a class of coupling potentials," *Phys. Rev. A*, vol. 23, pp. 2496–2501, 1981.

[33] F. T. Hioe, "Solution of Bloch equations involving amplitude and frequency modulations," *Phys. Rev. A*, vol. 30, pp. 2100–2103, 1984.

[34] M. Abramowitz and I. A. Stegun, *Handbook of Mathematical Functions with Formulas, Graphs, and Mathematical Tables.* National Bureau of Standards Applied Mathematics Series, 1964.

[35] C. M. Simon, T. Belhadj, B. Chatel, T. Amand, P. Renucci, A. Lemaitre, O. Krebs, P. A. Dalgarno, R. J. Warburton, X. Marie, and B. Urbaszek, "Robust quantum dot exciton generation via adiabatic passage with frequency-swept optical pulses," *Phys. Rev. Lett.*, vol. 106, p. 166801, 2011.

[36] T. F. S. Büttner, I. V. Kabakova, D. D. Hudson, R. Pant, C. G. Poulton, A. C. Judge, and B. J. Eggleton, "Phase-locking and pulse generation in multi-frequency Brillouin oscillator via four wave mixing," *Sci. Rep.*, vol. 4, p. 5032; DOI:10.1038/srep05032, 2014.

[37] T. F. S. Büttner, M. Merklein, I. V. Kabakova, D. D. Hudson, D. Y. Choi, B. Luther-Davies, S. J. Madden, and B. J. Eggleton, "Phase-locked, chip-based, cascaded stimulated Brillouin scattering," *Optica*, vol. 1, p. 311, 2014.

[38] B. Min, P. Kim, and N. Park, "Flat amplitude equal spacing 798-channel Rayleigh-assisted Brillouin/Raman multiwavelength comb generation in dispersion compensating fiber," *IEEE Photonics Technol. Lett.*, vol. 13, p. 1352, 2001.

[39] K. O. Hill, D. C. Johnson, and B. S. Kawasaki, "Transmission of narrow band high power laser radiation through optical fibers," *Appl. Phys. Lett.*, vol. 29, p. 185, 1976.

[40] M. Dong and H. G. Winful, "Unified approach to cascaded stimulated Brillouin scattering and frequency-comb generation," *Phys. Rev. A*, vol. 93, p. 043851, 2016.

[41] A. Yariv and P. Yeh, *Optical Waves in Crystals*. Hoboken, NJ: John Wiley and Sons Inc., 2003.

[42] K. Ogusu, "Analysis of steady-state cascaded stimulated Brillouin scattering in a fiber Fabry-Perot resonator," *IEEE Photonics Technol. Lett.*, vol. 14, no. 947-949, 2002.

[43] R. W. Boyd, K. Rzazewski, and P. Narum, "Noise initiation of stimulated Brillouin scattering," *Phys. Rev. A*, vol. 42, pp. 5514–5521, 1990.

[44] A. K. Kobyakov, M. Sauer, and D. Chowdhury, "Transient and nonlinear analysis of slow-light pulse propagation in an optical fiber via stimulated Brillouin scattering," *Adv. Opt. Photonics*, vol. 2, p. 1, 2010.

[45] S. Coen, H. G. Randle, T. Silvestre, and M. Erkintalo, "Modeling of octave-spanning Kerr frequency combs using a generalized mean-field Lugiato–Lefever model," *Opt. Lett.*, vol. 38, p. 37, 2013.

[46] T. Russel and W. Roh, "Threshold of second-order stimulated Brillouin scattering in optical fiber," *J. Opt. Soc. Am. B*, vol. 19, p. 2341, 2002.

[47] A. Liu, "Suppressing stimulated Brillouin scattering in fiber amplifiers using nonuniform fiber and temperature gradient," *Optics Express*, vol. 15, no. 3, p. 977, 2007.

[48] K. Ogusu, "Interplay between cascaded stimulated Brillouin scattering and four-wave mixing in a fiber Fabry-Perot resonator," *J. Opt. Soc. Am. B*, vol. 20, p. 685, 2003.

[49] J. Tang, J. Sun, T. Chen, and Y. Zhou, "A stable optical comb with double-Brillouin-frequency spacing assisted by multiple four-wave mixing processes," *Opt. Fiber Tech.*, vol. 17, p. 608, 2011.

[50] K. Ogusu and A. Sakai, "Generation and dynamics of cascaded stimulated Brillouin scattering in a high-finesse fiber Fabry–Perot resonator," *Jpn J. Appl. Phys.*, vol. 41, p. 609, 2002.

[51] P. J. Delfyett, L. T. Florez, N. Stoffel, T. Gmitter, N. C. Andreadakis, Y. Silberberg, and J. P. Heritage, "High-power ultrafast laser diodes," *IEEE J. Quantum Electron.*, vol. 28, no. 10, p. 2203, 1992.

[52] U. Keller, "Ultrafast solid-state laser oscillators: a success story for the last 20 years with no end in sight," *Phys. Rev. B*, vol. 100, pp. 15–28, 2010.

[53] L. F. Tiemeijer, P. I. Kuindersma, P. J. A. Thijs, and G. L. J. Rikken, "Passive FM locking in InGaAsP semiconductor lasers," *IEEE J. Quantum Electron.*, vol. 25, no. 6, p. 1385, 1989.

[54] C. Calò, V. Vujicic, R. Watts, C. Browning, K. Merghem, V. Panapakkam, F. Lelarge, A. Martinez, B.-E. Benkelfat, A. Ramdane, and L. P. Barry, "Single-section quantum well mode-locked laser for 400 Gb/s SSB-OFDM transmission," *Opt. Express*, vol. 23, no. 20, p. 26442, 2015.

[55] K. Sato, "Optical pulse generation using Fabry–Pérot lasers under continuous-wave operation," *IEEE J. Sel. Top. Quantum Electron.*, vol. 9, no. 5, p. 1288, 2003.

[56] R. Rosales, K. Merghem, A. Martinez, A. Akrout, J.-P. Tourrenc, A. Accard, F. Lelarge, and A. Ramdane, "InAs/InP quantum-dot passively mode-locked lasers for 1.55-μm applications," *IEEE J. Sel. Top. Quantum Electron.*, vol. 17, no. 5, p. 1292, 2011.

[57] R. Rosales, K. Merghem, C. Calo, G. Bouwmans, I. Krestnikov, A. Martinez, and A. Ramdane, "Optical pulse generation in single section InAs/GaAs quantum dot edge emitting lasers under continuous wave operation," *App. Phys. Lett.*, vol. 101, p. 221113, 2012.

[58] R. Rosales, S. G. Murdoch, R. Watts, K. Merghem, A. Martinez, F. Lelarge, A. Accard, L. P. Barry, and A. Ramdane, "High performance mode locking characteristics of single section quantum dash lasers," *Optics Express*, vol. 20, no. 8, p. 8649, 2012.

[59] A. Hugi, G. Villares, S. Blaser, H. C. Liu, and J. Faist, "Mid-infrared frequency comb based on a quantum cascade laser," *Nature*, vol. 492, p. 229, 2012.

[60] M. Gioannini, P. Bardella, and I. Montrosset, "Time-domain traveling-wave analysis of the multimode dynamics of quantum dot Fabry–Perot lasers," *IEEE Sel. Topics Quantum Electron.*, vol. 21, p. 1900811, December 2015.

[61] M. Rossetti, P. Bardella, and I. Montrosset, "Time-domain travelling-wave model for quantum dot passively mode-locked lasers," *IEEE J. Quantum Electron.*, vol. 47, no. 2, p. 139, 2011.

[62] J. B. Khurgin, Y. Dikmelik, A. Hugi, and J. Faist, "Coherent frequency combs produced by self frequency modulation in quantum cascade lasers," *App. Phys. Lett.*, vol. 104, no. 8, p. 081118, 2014.

[63] J. Faist, G. Villares, G. Scalari, M. Rösch, C. Bonzon, A. Hugi, and M. Beck, "Quantum cascade laser frequency combs," *Nanophotonics*, vol. 5, no. 2, pp. 272–291, 2016.

[64] M. Dong, N. M. Mangan, J. N. Kutz, S. T. Cundiff, and H. G. Winful, "Traveling wave model for frequency comb generation in single-section quantum well diode lasers," *IEEE J. Quantum Electron.*, vol. 53, no. 6, p. 2500311, 2017.

[65] W. W. Chow, S. W. Koch, and M. Sargent III, *Semiconductor-Laser Physics*. Springer-Verlag, 1994.

[66] S. L. Chuang, *Physics of Photonic Devices*. Hoboken, NJ: John Wiley and Sons, Inc., 2nd ed., 2009.

[67] M. Zimmermann, S. Krämer, F. Steinhagen, H. Hillmer, H. Burkhard, A. Ougazzaden, C. Kazmierski, and A. Hangleiter, "Experimental determination of the intraband relaxation time in strained quantum well lasers," *Hot Carriers in Semiconductors*, p. 591, 1996.

[68] A. E. Siegman, *Lasers*. 55D Gate Five Road, Sausalito, CA 94965: University Science Books, 1986.

[69] K. Kim and D.-S. Shin, "Comparison of quantum wells based on InGaAs(P)/InP and InGa(Al)As/InAlAs material systems in view of carrier escape times for high-saturation-optical-power electroabsorption modulators," *J. Optical Society Korea*, vol. 11, no. 3, pp. 133–137, 2007.

[70] G. Ji, D. Huang, U. K. Reddy, H. Unlu, T. S. Henderson, and H. Morkoç, "Determination of band offsets in AlGaAs/GaAs and InGaAs/GaAs multiple quantum wells," *J. Vacuum Sci. and Tech. B: Microelectronics Processing and Phenomena*, vol. 5, p. 1346, 1987.

[71] M. Homar, S. Balle, and M. S. Miguel, "Mode competition in a Fabry-Perot semiconductor laser: travelling wave model with asymmetric dynamical gain," *Optics Communications*, vol. 131, pp. 380–390, 1996.

[72] Y. Arakawa and A. Yariv, "Quantum well lasers - gain, spectra, dynamics," *IEEE J. Quantum Electron.*, vol. QE22, no. 9, p. 1887, 1986.

[73] S. N. Kaunga-Nyirenda, M. P. Dlubek, A. J. Phillips, J. J. Lim, E. C. Larkins, and S. Sujecki, "Theoretical investigation of the role of optically induced carrier pulsations in wave mixing in semiconductor optical amplifiers," *J. Opt. Soc. Am. B*, vol. 27, p. 168, February 2010.

[74] D. McDonald and R. F. O'Dowd, "Comparison of two- and three-level rate equations in the modeling of quantum-well lasers," *IEEE J. Quantum Electron.*, vol. 31, p. 1927, November 1995.

[75] D. J. Jones, L. M. Zhang, J. E. Carroll, and D. D. Marcenac, "Dynamics of monolithic passively mode-locked semiconductor lasers," *IEEE J. Quantum Electron.*, vol. 31, pp. 1051–1058, June 1995.

[76] A. D. Vandermeer and D. T. Cassidy, "A rate equation model of asymmetric multiple quantum-well lasers," *IEEE J. Quantum Electron.*, vol. 41, no. 7, p. 917, 2005.

[77] A. Gordon, C. Y. Wang, L. Diehl, F. X. Kärtner, A. Belyanin, D. Bour, S. Corzine, G. Höfler, H. C. Liu, H. Schneider, T. Maier, M. Troccoli, J. Faist, and F. Capasso, "Multimode regimes in quantum cascade lasers: From coherent instabilities to spatial hole burning," *Phys. Rev. A*, vol. 77, no. 5, p. 053804, 2008.

[78] D. Lenstra and M. Yousefi, "Rate-equation model for multi-mode semiconductor lasers with spatial hole burning," *Opt. Express*, vol. 22, no. 7, p. 8144, 2014.

[79] C. H. Henry, R. A. Logan, and K. A. Bertness, "Spectral dependence of the change in refractive index due to carrier injection in GaAs lasers," *Journal of Applied Physics*, vol. 51, no. 7, p. 4457, 1981.

[80] M. Homar, J. V. Moloney, and M. S. Miguel, "Traveling wave model of a multimode Fabry-Perot laser in free running and external cavity configurations," *IEEE J. Quantum Electron.*, vol. 32, no. 3, p. 553, 1996.

[81] J. Javaloyes and S. Balle, "Emission directionality of semiconductor ring lasers: A traveling-wave description," *IEEE J. Quantum Electron.*, vol. 45, no. 5, p. 431, 2009.

[82] C. B. Su, "Dielectric grating induced by cavity standing wave as a new explanation of origin of nonlinear gain in semiconductor diode lasers," *IEEE Electron. Lett.*, vol. 24, no. 7, pp. 370–371, 1988.

[83] D. Marshall, A. Miller, and C. C. Button, "In-well ambipolar diffusion in room-temperature InGaAsP multiple quantum wells," *IEEE J. Quantum Electron.*, vol. 36, no. 9, p. 1013, 2000.

[84] Y. Nomura, S. Ochi, N. Tomita, K. Akiyama, T. Isu, T. Takiguchi, and H. Higuchi, "Mode locking in Fabry-Perot semiconductor lasers," *Phys. Rev. A*, vol. 65, p. 043807, 2002.

[85] P. Bardella, L. L. Columbo, and M. Gioannini, "Self-generation of optical frequency comb in single section quantum dot Fabry-Perot lasers: a theoretical study," *Optics Express*, vol. 25, no. 21, pp. 26234–26252, 2017.

[86] Z. Lu, J. Liu, P. Poole, Z. Jiao, P. Barrios, D. Poitras, J. Caballero, and X. Zhang, "Ultra-high repetition rate InAs/InP quantum dot mode-locked lasers," *Optics Communications*, vol. 284, pp. 2323–2326, 2011.

[87] Z. Jiao, R. Zhang, X. Zhang, J. Liu, and Z. Lu, "Modeling of single-section quantum dot mode-locked lasers: Impact of group velocity dispersion and self phase modulation," *IEEE J. of Quant. Elec.*, vol. 49, no. 12, p. 1008, 2013.

[88] G. P. Agrawal, "Population pulsations and nondegenerate four-wave mixing in semiconductor lasers and amplifiers," *J. Opt. Soc. Am. B*, vol. 5, no. 1, p. 147, 1988.

[89] R. Nietzke, P. Panknin, W. Elsäßer, and E. O. Göbel, "Four-wave mixing in GaAs/AlGaAs semiconductor lasers," *IEEE J. of Quant. Elec.*, vol. 25, no. 6, p. 1399, 1989.

[90] P. P. Baveja, D. N. Maywar, and G. P. Agrawal, "Interband four-wave mixing in semiconductor optical amplifiers with ASE-enhanced gain recovery," *IEEE J. Sel. Topics Quantum Electron.*, vol. 18, no. 2, p. 899, 2012.

[91] J. Renaudier, G.-H. Duan, P. Landais, and P. Gallion, "Phase correlation and linewidth reduction of 40 GHz self-pulsation in distributed Bragg reflector semiconductor lasers," *IEEE J. Quantum Electron.*, vol. 43, p. 147, 2007.

[92] A. Godard, G. Pauliat, G. Roosen, and E. Ducloux, "Modal competition via four-wave mixing in single-mode extended-cavity semiconductor lasers," *IEEE J. of Quant. Elec.*, vol. 40, no. 8, p. 970, 2004.

[93] A. Mecozzi, "Cavity standing-wave and gain compression coefficient in semiconductor lasers," *Optics Letters*, vol. 19, no. 9, p. 640, 1994.

[94] B. A. Ruzicka, L. K. Werake, H. Samassekou, and H. Zhou, "Ambipolar diffusion of photoexcited carriers in bulk GaAs," *Appl. Phys. Lett.*, vol. 97, p. 262119, 2011.

[95] H. Rieck, "The effective lifetime of stimulated and spontaneous emission in semiconductor laser diodes," *Solid State Electronics*, vol. 8, pp. 83–85, 1964.

[96] J. R. Ackerhalt, "Novel analytic solutions to general four-wave-mixing problems in a Raman medium," *Phys. Rev. Lett.*, vol. 46, no. 14, p. 922, 1981.

[97] T. Herr, K. Hartinger, J. Riemensberger, C. Y. Wang, E. Gavartin, R. Holzwarth, M. L. Gorodetsky, and T. J. Kippenberg, "Universal formation dynamics and noise of Kerr-frequency combs in microresonators," *Nat. Phot.*, vol. 6, p. 480, 2012.

[98] P. H. Holloway and G. E. McGuire, *Handbook of Compound Semiconductors.* Mill Rd., Park Ridge, NJ 07656: Noyes Publications, 1995.

[99] M. Rosenzweig, M. Möhrle, H. Düser, and H. Venghaus, "Threshold-current analysis of InGaAs-InGaAsP multiquantum well separate-confinement lasers," *IEEE J. Quantum Electron.*, vol. 27, no. 6, p. 1804, 1991.

[100] D. G. Ivey and P. Jian, "Metallurgy of ohmic contacts to InP," *Canadian Metallurgical Quarterly*, vol. 34, no. 2, pp. 85–113, 1995.

[101] G. Belenky, L. Shterengas, C. W. Russel, C. L. Reynolds, M. S. Hybertsen, and R. Menna, "Trends in semiconductor laser design: Balance between leakage, gain and loss in InGaAsP/InP MQW structures," *Advanced Research Workshop on Future Trends in Microelectronics*, no. 231–240, 2002.

[102] P. S. Zory, *Quantum Well Lasers.* 1250 Sixth Ave., San Diego, CA 92101-4311: Academic Press, Inc., 1993.

[103] B. V. Zeghbroeck, *Principles of Semiconductor Devices and Heterojunctions.* Prentice Hall PTR, 2007.

[104] C.-W. Lee, D. Nie, T. Mei, and M. K. Chin, "Study and optimization of room temperature inductively coupled plasma etching of InP using Cl2/CH4/H2 and CH4/H2," *J. of Crystal Growth*, vol. 288, pp. 213–216, 2006.